

1

UNIVERSITY OF BRISTOL

2

DOCTORAL THESIS

3

4

Investigating, implementing, and creating methods for analysing large neuronal ensembles

5

6

Author:

Thomas J. DELANEY

Supervisors:

Dr. Cian O'DONNELL

Dr. Michael C. ASHBY

7

A thesis submitted in fulfillment of the requirements

for the degree of Doctor of Philosophy

8

in the

9

Biological Intelligence & Machine Learning Unit

10

Department of Computer Science

11

12

July 8, 2020

¹⁵ Declaration of Authorship

¹⁶ I, Thomas J. DELANEY, declare that this thesis titled, "Investigating, implementing, and
¹⁷ creating methods for analysing large neuronal ensembles" and the work presented in it are
¹⁸ my own. I confirm that:

- ¹⁹ • This work was done wholly or mainly while in candidature for a research degree at this
²⁰ University.
- ²¹ • Where any part of this thesis has previously been submitted for a degree or any other
²² qualification at this University or any other institution, this has been clearly stated.
- ²³ • Where I have consulted the published work of others, this is always clearly attributed.
- ²⁴ • Where I have quoted from the work of others, the source is always given. With the
²⁵ exception of such quotations, this thesis is entirely my own work.
- ²⁶ • I have acknowledged all main sources of help.
- ²⁷ • Where the thesis is based on work done by myself jointly with others, I have made
²⁸ clear exactly what was done by others and what I have contributed myself.

²⁹

³⁰ Signed:

³¹ _____

³² Date:

³³ _____

34

UNIVERSITY OF BRISTOL

35

Abstract

36

Engineering

37

Department of Computer Science

38

Doctor of Philosophy

39

**Investigating, implementing, and creating methods for analysing large neuronal
ensembles**

41

by Thomas J. DELANEY

42

The Thesis Abstract is written here (and usually kept to just this page). The page is kept centered vertically so can expand into the blank space above the title too...

44

Acknowledgements

45 The acknowledgments and the people to thank go here, don't forget to include your project

46 advisor...

⁴⁷ Contents

⁴⁸	Declaration of Authorship	iii
⁴⁹	Abstract	v
⁵⁰	Acknowledgements	vii
⁵¹	1 Introduction	1
⁵²	1.1 Overview	1
⁵³	2 Sensitivity of the spikes-to-fluorescence transform to calcium indicator and neu-	
⁵⁴	ron properties	7
⁵⁵	2.1 Introduction	8
⁵⁶	2.2 Results	10
⁵⁷	2.2.1 A biophysical computational model can generate accurate fluores-	
⁵⁸	cence traces from spike trains	10
⁵⁹	2.2.2 Spike inference algorithms perform similarly on real data compared	
⁶⁰	with time series simulated from the model	11
⁶¹	2.2.3 Relative effects of various buffers to the fluorescence signal	12
⁶²	2.2.4 Spike inference accuracy is sensitive to indicator properties, and likely	
⁶³	varies within and between cells	13
⁶⁴	2.2.5 Single spike inference accuracy drops for high firing rates, but firing	
⁶⁵	rate itself can be estimated from mean fluorescence amplitude	18
⁶⁶	2.3 Discussion	21
⁶⁷	2.4 Methods	23
⁶⁸	2.4.1 Calcium dynamics model	23
⁶⁹	Photon release & capture	25
⁷⁰	2.4.2 Parameter optimisation	26
⁷¹	Fixed parameters	27
⁷²	2.4.3 Julia	27

73	2.4.4	Spike inference	29
74		Comparing spike inference quality	31
75	2.4.5	Perturbation analysis	31
76	2.4.6	Signal-to-noise ratio	31
77	2.4.7	Data sources	32
78	3	Functional networks expand across anatomical boundaries as correlation time-scale increases	33
79	3.1	Introduction	34
80	3.2	Results	35
81	3.2.1	Average correlation size increases with increasing time bin width	35
82	3.2.2	Goodness-of-fit for Poisson and Gaussian distributions across increasing time bin widths	36
83	3.2.3	Differences between and inter- and intra- regional correlations decrease with increasing bin width	38
84	3.2.4	Connected and divided structure in correlation based networks reduces in dimension with increasing bin width	41
85	3.2.5	Detecting communities in correlation based networks	42
86	3.2.6	Functional communities resemble anatomical division at short timescales	42
87	3.2.7	Conditional correlations & signal correlations	46
88	3.2.8	Absolute correlations and negative rectified correlations	50
89	3.3	Discussion	53
90	3.4	Data	56
91	3.4.1	Brain regions	56
92	3.4.2	Video recordings	57
93	3.5	Methods	57
94	3.5.1	Binning data	57
95	3.5.2	Correlation coefficients	57
96		Total correlations, r_{SC}	58
97		Shuffled total correlations	58
98		Separating Correlations & Anti-correlations	58
99	3.5.3	Conditioning on behavioural data	59
100		Linear regression	59
101		Elastic net regularisation	59

106	Conditional covariance	60
107	Measures of conditional correlation	61
108	3.5.4 Information Theory	61
109	Entropy $H(X)$	61
110	Maximum entropy limit	62
111	Mutual Information $I(X; Y)$	63
112	Variation of Information $VI(X, Y)$	64
113	Measuring entropies & mutual information	65
114	3.5.5 Network analysis	65
115	Correlation networks	65
116	Rectified correlations	65
117	Sparsifying data networks	66
118	Communities	66
119	Weighted configuration model	66
120	Sparse weighted configuration model	66
121	Spectral rejection	67
122	Node rejection	68
123	Community detection	68
124	3.5.6 Clustering Comparison	69
125	Adjusted Rand Index	69
126	Clusterings as random variables	70
127	Information based similarity measures	70
128	Information based metrics	71
129	Comparing detected communities and anatomical divisions	71
130	4 A simple two parameter distribution for modelling neuronal activity and capturing neuronal association	73
131	4.1 Introduction	74
132	4.2 Data	75
133	4.2.1 Experimental protocol	75
134	4.3 Methods	76
135	4.3.1 Binning data	76
136	4.3.2 Number of <i>active</i> neurons	76
137	4.3.3 Moving windows for measurements	76

139	4.3.4	Fano factor	78
140	4.3.5	Probability Distributions suitable for modelling ensemble activity . .	78
141		Association	78
142		Binomial distribution	79
143		Beta-binomial distribution	79
144		Conway-Maxwell-binomial distribution	80
145	4.3.6	Fitting	82
146	4.3.7	Goodness-of-fit	84
147	4.4	Results	84
148	4.4.1	Increases in mean number of active neurons and variance in number of active neurons at stimulus onset in some regions	84
149		Primary visual cortex	85
150		Hippocampus	85
151		Thalamus	85
152	4.4.2	Conway-Maxwell-binomial distribution is usually a better fit than bi- nomial or beta-binomial	85
153	4.4.3	Conway-Maxwell-binomial distribution captures changes in associ- ation at stimulus onset	90
154	4.4.4	Replicating stimulus related quenching of neural variability	90
155	4.5	Discussion	92
159	5	Studies with practical limitations & negative results	95
160	5.1	Dynamic state space model of pairwise and higher order neuronal correlations	96
161	5.2	A multiscale model for hierarchical data applied to neuronal data	96
163	6	Discussion	99
164	Bibliography		101

165 List of Figures

166 2.1	A: Example spike train (blue) and the corresponding GCaMP6s fluorescence 167 trace (green), data replotted from (Berens et al., 2018). Inset shows zoomed 168 section of traces to highlight slow decay of GCaMP6s fluorescence relative 169 to spike time intervals. B: Schematic diagram of the neuron calcium and 170 GCaMP computational model. C: Good visual match of data fluorescence 171 trace (green) and model simulated fluorescence (orange) in response to an 172 identical spike train (blue).	9
173 2.2	A: Workflow to compare spike inference for real versus simulated fluores- 174 cence data. B: True positive rates achieved by three different spike inference 175 algorithms when applied to observed spike trains, and simulated spike trains. 176 Data points overlaid as blue circles. The performance is similar from real 177 and simulated data for each of the algorithms.	12
178 2.3	Calcium Buffering Dynamics (a) The proportions of bound and free cal- 179 cium concentrations within a cell, with the associated spike train. (b)-(f) The 180 dynamics of the concentration of (b) excited indicator bound calcium, (c) in- 181 dicator bound calcium, (d) immobile endogenous buffer bound calcium, (e) 182 mobile endogenous buffer bound calcium, and (f) free calcium in response to 183 an action potential at $\sim 23.2\text{s}$	14
184 2.4	(a) An example trace for each of the five pairs of values used for the binding 185 and unbinding rates of the fluorescent calcium indicator. (b) The signal-to- 186 noise ratio of the modelled fluorescence traces using each of the four per- 187 turbed values, and the experimental value. The SNRs for the two pairs with 188 values lower than the experimental value are lower than the experimental pair 189 or the higher value pairs. (c) The true-positive rates of the deconvolution al- 190 gorithm's predictions when inferring from the observed data, and inferring 191 from modelled traces using the perturbed and experimental values.	16

192	2.5 (a) An example trace for each of the five perturbed values for the concentration of fluorescent calcium indicator. The top two traces are produced by the lower perturbed values, the middle trace is produced by the experimental value, and the lowest two traces are produced when using the higher perturbed values. (b) The signal-to-noise ratio of the modelled fluorescence traces using each of the four perturbed values, and the experimental value. Extreme perturbations of the concentration either above or below the experimental level lowered the SNR. (c) The true-positive rates of the deconvolution algorithm's predictions when inferring from the observed data, and inferring from modelled traces using the perturbed and experimental values. We found that the algorithms performs equally badly on the two most extreme values, and performs equally well on the experimental value, and the next higher perturbed value.	17
205	2.6 (a) An example trace for each of the five perturbed values for the concentration of immobile endogenous buffer. (b) The signal-to-noise ratio of the modelled fluorescence traces using each of the four perturbed values, and the experimental value. The lower values for the immobile buffer produce the same SNR as the experimental value. But the higher perturbed values produce fluorescence traces with a lower SNR. (c) The true-positive rates of the deconvolution algorithm's predictions when inferring from the observed data, and inferring from modelled traces using the perturbed and experimental values.	19
214	2.7 Simulating fluorescence traces at different firing rates Example modelled traces created using simulated spike trains with a mean firing rate of 1Hz (left column), 5Hz (middle column), and 10Hz (right column). Note the difference in amplitude with different mean firing rates.	20
218	2.8 Inference quality and $\Delta F/F_0$ vs Firing rate (left) The spike inference accuracy when applied to 30 traces created using simulated spike trains with mean firing rates of 1, 5, and 10 Hz. (right) The mean $\Delta F/F_0$ across those 30 traces for each frequency.	21

222	3.1 (A) An example of the correlation coefficients between two different pairs 223 of cells, one where both cells are in the same brain region (intra-regional 224 pair), and one where both cells are in different brain regions (inter-regional 225 pair). The correlation coefficients have been measured using different time 226 bin widths, ranging from 5ms to 3s. Note the increasing amplitude of the 227 correlations with increasing bin width. (B) A raster plot showing the spike 228 times of each pair of cells.	36
229	3.2 Mean correlation coefficients measured from pairs of 50 randomly chosen 230 neurons. (A) All possible pairs, (B) positively correlated pairs, and (C) neg- 231 atively correlated pairs. (D) Mean and standard error of χ^2 test statistics for 232 Poisson and Gaussian distributions fitted to neuron spike counts.	37
233	3.3 (Left)The mean intra-region and inter-region correlations using all possible 234 pairs of \sim 500 neurons, spread across 9 different brain regions. (Right) 235 Courtesy of Stringer et al. (2019), mean inter-regional (out-of-area) correla- 236 tion coefficients vs mean intra-regional (within-area) correlation coefficients 237 for a bin width of 1.2s. Note that the intra-regional coefficients are higher in 238 each case.	39
239	3.4 The mean intra-regional correlations (coloured dots) and mean inter-regional 240 correlations (black dots) for a given region, indicated on the x-axis, for dif- 241 ferent time bin widths. Each black dot represents the mean inter-regional 242 correlations between the region indicated on the x-axis and one other region. 243 (A) shows these measurements when we used a time bin width of 5ms. (B) 244 shows these measurements when we used a time bin width of 1s. Note that 245 the difference between the mean inter-regional correlations and mean intra- 246 regional correlations is smaller for 1s bins.	40
247	3.5 Mean inter-regional (main diagonal) and intra-regional (off diagonal) corre- 248 lation coefficients. (A) Shows these measurements when spike times were 249 binned using 5ms time bins. (B) Shows the same, using 1s time bins. Note 250 that the matrices are ordered according to the main diagonal values, therefore 251 the ordering is different in each subfigure.	41

252 3.6	The number of dimensions in the k -partite and connected structure in the cor-		
253	relation based networks beyond the structure captured by a sparse weighted		
254	configuration null network model (see section 3.5.5), shown for different time		
255	bin widths. Note that the k -partite structure disappears for time bin width		
256	greater than 200ms for all three subjects. The dimension of the connected		
257	structure reduces with increasing bin width for 2 of the 3 subjects (top row).	43	
258 3.7	(A-B) Correlation matrices with detected communities indicated by white		
259	lines. Each off main diagonal entry in the matrix represents a pair of neu-		
260	rons. Those entries within a white square indicate that both of those neurons		
261	are in the same community as detected by our community detection proce-		
262	dure. Matrices shown are for 5ms and 1s time bin widths respectively. Main		
263	diagonal entries were set to 0. (C-D) Matrices showing the anatomical dis-		
264	tribution of pairs along with their community membership. Entries where		
265	both cells are in the same region are given a colour indicated by the colour		
266	bar. Entries where cells are in different regions are given the grey colour also		
267	indicated by the colour bar.	44	
268 3.8	(A) The variation of information is a measure of distance between cluster-		
269	ings. The distance between the anatomical ‘clustering’ and community de-		
270	detection ‘clustering’ increases with increasing time bin width. (B) The ad-		
271	justed Rand index is a normalised similarity measure between clusterings.		
272	The anatomical and community detection clusterings become less similar as		
273	the time bin width increases.	45	
274 3.9	Comparing the components of the total covariance across different values for		
275	the time bin width. We observed a consistent increase in $E[\text{cov}(X, Y Z)]$ as		
276	the time bin width increased. But we saw different trends for $\text{cov}(E[X Z], E[Y Z])$		
277	for each mouse.	46	
278 3.10	Comparing the components of the total covariance across different values for		
279	the time bin width. We saw a consistent increase in $\rho_{X,Y Z}$ as the time bin		
280	width increased in all three subjects. But we saw different trends in ρ_{signal} for		
281	each of the subjects.	47	

282	3.11 Matrices showing the regional membership of pairs by colour, and the com-	
283	munities in which those pairs lie. (A-B) Detected communities and regional	
284	membership matrix for network based on rectified spike count correlation	
285	$\rho_{X,Y Z}$, using time bin widths of 0.005s and 1s respectively. (C-D) Detected	
286	communities and regional membership matrix for network based on rectified	
287	signal correlation ρ_{signal} , using time bin widths of 0.005s and 1s respectively.	48
288	3.12 Distance and similarity measures between the anatomical division of the neu-	
289	rons, and the communities detected in the network based on the spike count	
290	correlations $\rho_{X,Y Z}$. (A) The variation of information is a ‘distance’ mea-	
291	sure between clusterings. The distance between the anatomical ‘clustering’	
292	and the community clustering increases as the time bin width increases. (B)	
293	The adjusted Rand index is a similarity measure between clusterings. The	
294	detected communities become less similar to the anatomical division of the	
295	cells as the time bin width increases.	49
296	3.13 Distance and similarity measures between the anatomical division of the neu-	
297	rons, and the communities detected in the network based on the signal cor-	
298	relations ρ_{signal} . (A) The variation of information is a ‘distance’ measure be-	
299	tween clusterings. The distance between the anatomical ‘clustering’ and the	
300	community clustering increases as the time bin width increases. (B) The ad-	
301	justed Rand index is a similarity measure between clusterings. The detected	
302	communities become less similar to the anatomical division of the cells as	
303	the time bin width increases.	50
304	3.14 (A-B) Absolute correlation matrices with detected communities indicated by	
305	white lines. These communities are based on the absolute value of the total	
306	correlation between each pair of cells. Those entries within a white square in-	
307	dicate that both of those neurons are in the same community. Matrices shown	
308	are for 5ms and 1s time bin widths respectively. Main diagonal entries were	
309	set to 0. (C-D) Matrices showing the anatomical distribution of pairs along	
310	with their community membership. Regional membership is indicated by the	
311	colour bar. (E) Variation of information between the anatomical division of	
312	the cells, and the detected communities. (F) Adjusted Rand index between	
313	the anatomical division, and the detected communities.	51

314	3.15 (A-B) Sign reversed rectified correlation matrices with detected communities indicated by white lines. Those entries within a white square indicate that both of those neurons are in the same community. Matrices shown are for 5ms and 1s time bin widths respectively. Main diagonal entries were set to 0. (C-D) Matrices showing the anatomical distribution of pairs along with their community membership. Regional membership is indicated by the colour bar. (E) Variation of information between the anatomical division of the cells, and the detected communities. (F) Adjusted Rand index between the anatomical division, and the detected communities.	52
323	3.16 Probe Locations: The locations of the probes in each of the three mouse brains (Stringer et al., 2019).	57
325	3.17 Entropy Limit: The upper limit on entropy of binned spike count data as a function of the maximum observed spike count. The orange line is the analytical maximum. The blue line is the entropy of samples with $N = 1000$ data points taken from the discrete uniform distribution.	63
329	4.1 Figures showing the over-dispersion possible for a beta-binomial distribution relative to a binomial distribution. Parameters are shown in the captions.	80
331	4.2 Figures showing (A) the under-dispersion and (B) over-dispersion permitted by the COMb distribution relative to a binomial distribution. (C) illustrates that the p parameter of the COMb distribution does not correspond to the mean of the distribution, as it does for the binomial and beta-binomial distributions. (D) shows a heatmap for the value of the Kullback-Liebler divergence between the COMb distribution and the standard binomial distribution with same value for n , as a function of p and ν . Parameters are shown in the captions.	83

339	4.3 (A) Raster plot showing the spikes fired by 33 randomly chosen neurons in	
340	the primary visual cortex. (B-C) (B) average and (C) variance of the number	
341	of active neurons, measured using a sliding window 100ms wide, split into	
342	100 bins. The midpoint of the time interval for each window is used as the	
343	timepoint (x-axis point) for the measurements using that window. The grey	
344	shaded area indicates the presence of a visual stimulus. The opaque line is	
345	an average across the 160 trials that included a visual stimulus of any kind.	
346	We can see a transient increase in the average number of active neurons and	
347	the variance of this number, followed by a fluctuation and another increase.	86
348	4.4 (A) Raster plot showing the spikes fired by 33 randomly chosen neurons in	
349	the hippocampus. (B-C) (B) average and (C) variance of the number of active	
350	neurons, measured using a sliding window 100ms wide, split into 100 bins.	
351	The midpoint of the time interval for each window is used as the timepoint (x-	
352	axis point) for the measurements using that window. The grey shaded area	
353	indicates the presence of a visual stimulus. The opaque line is an average	
354	across the 160 trials that included a visual stimulus of any kind. We can see	
355	a transient increase in the average number of active neurons and the variance	
356	of this number at stimulus onset.	87
357	4.5 (A) Raster plot showing the spikes fired by 33 randomly chosen neurons in	
358	the thalamus. (B-C) (B) average and (C) variance of the number of active	
359	neurons, measured using a sliding window 100ms wide, split into 100 bins.	
360	The midpoint of the time interval for each window is used as the timepoint (x-	
361	axis point) for the measurements using that window. The grey shaded area	
362	indicates the presence of a visual stimulus. The opaque line is an average	
363	across the 160 trials that included a visual stimulus of any kind. We can	
364	see an immediate increase at stimulus onset, a subsequent fall, and another	
365	sustained increase until the stimulus presentation ends.	88

366	4.6 (A) An example of the binomial, beta-binomial, and Conway-Maxwell-binomial	
367	distributions fitted to a sample of neural activity. The Conway-Maxwell-	
368	binomial distribution is the best fit in this case. The histogram shows the	
369	empirical distribution of the sample. The probability mass function of each	
370	distribution is indicated by a different coloured line. (B) Across all samples	
371	in all trials, the proportion of samples for which each fitted distribution was	
372	the best fit. The Conway-Maxwell-binomial distribution was the best fit	
373	for 93% of the samples taken from V1 using a bin width of 1ms.	89
374	4.7 (A) We fit a Conway-Maxwell-binomial distribution to the number of active	
375	neurons in 1ms time bins of a 100ms sliding window. We did this for all	
376	trials with a visual stimulus and took the average across those trials. We	
377	see a transient drop in value for the distribution's ν parameter at stimulus	
378	onset. This shows an increase in association between the neurons. (B) We	
379	measured the correlation coefficient between the spike counts of all possible	
380	pairs of neurons in the same sliding window. The took the average of those	
381	coefficients. We also did this for every visually stimulated trial, and took	
382	the average across trials. The increase in association is not reflected with an	
383	increase in average correlation.	91
384	4.8 (A) The mean Fano factor of the spike counts of the cells in the primary visual	
385	cortex. Means were taken across cells first, then across trials. There was a	
386	significant decrease in the Fano factors immediately after stimulus onset. (B)	
387	The mean Fano factor of the spike counts of the cells in the motor cortex. No	
388	significant change in measurements at any point.	92

389 List of Tables

390 2.1	Fixed parameters A table of the parameters fixed before optimising the	
391	model. The values of these parameters could be changed to model differ-	
392	ent fluorescent calcium indicators.	28
393 4.1	Details of the different bin width and analysis window sizes used when bin-	
394	ning spike times, and analysing those data.	77
395 4.2	Relative dispersion of the COMb distribution, and association between Bernoulli	
396	variables as represented by the value of the ν parameter.	82
397 4.3	Proportion of samples for which each distribution was the best fit, grouped	
398	by bin width. The COMb distribution is the best fit most of the time.	90

³⁹⁹ List of Abbreviations

COMb Conway-Maxwell-binomial (distribution)

OASIS Online active set inference system?

For/Dedicated to/To my...

401 **Chapter 1**

402 **Introduction**

403 **1.1 Overview**

404 Since Hodgkin and Huxley's squid experiments featuring a single axon (Hodgkin and Hux-
405 ley, 1939), to more recent research with spike sorted data from ~ 24000 neurons from 34
406 brain regions from 21 mice (Allen et al., 2019), the number of neurons contributing to elec-
407 trophysiological datasets has been growing. Recording methods using two-photon calcium
408 imaging have also been used to extract data from populations containing over 10000 neurons
409 (Peron et al., 2015). This dramatic growth in the number of neurons available for analysis
410 requires a dramatic change in analysis methods. In this project, we have attempted to address
411 some of the difficulties in collecting data from these large ensembles, and analysing these
412 data.

413 To focus on calcium imaging for a start, a neuron that contains a fluorescent calcium
414 indicator in its cytoplasm will fluoresce when bombarded with photons. The amount that the
415 cell will fluoresce is dependent on the concentration of fluorescent indicator within the cell,
416 and the concentration of calcium within the cell. When a neuron fires an action potential, the
417 influx of free calcium ions causes an increase in fluorescence when those ions bond with the
418 fluorescent indicator and those bounded molecules are bombarded with photons. After the
419 action potential, as calcium is extruded from the cell the fluorescence returns to a baseline
420 level. This is the basic mechanism of fluorescent calcium indicator based imaging.

421 This method has some advantages over electrophysiology as measure of neuronal ensem-
422 ble activity. Isolating individual neurons is easier and more reliable than identifying unique
423 spike sources in electrophysiology (Buccino et al., 2019). Also, spike sorting methods can
424 only detect spikes, but imaging methods can also detect cells that are not spiking, because
425 cells will emit a baseline level of fluorescence when not firing action potentials. Calcium
426 imaging sites can be re-used for weeks for longitudinal studies (Chen et al., 2013). The

427 fluorescent indicator is delivered to the cell by adeno-associated viruses, consequently there
428 can be problems with indicator gradients around the infection site, and expression levels
429 will change in individual cells over weeks (Tian et al., 2009; Chen et al., 2013). This de-
430 livery method can also cause cell pathology, and nuclear filling (Zariwala et al., 2012), but
431 these problems can be solved by using lines of transgenic mice (Dana et al., 2014). The
432 fluorescence signal itself can serve a a good indicator of cell activity, but similarly to electro-
433 physiology, the aim of calcium imaging is often spike detection.

434 If the imaging data is collected at a high enough frequency, and the signal-to-noise ratio
435 of the fluorescence trace is high enough, it should be possible to infer the spike times to some
436 level of accuracy. For example, the calmodulin based indicator GCaMP6s has a sufficiently
437 high signal-to-noise ratio that isolated action potentials can be detected and inferred (Chen
438 et al., 2013). Many spike inference algorithms exist (Vogelstein et al., 2010; Pnevmatikakis
439 et al., 2016; Friedrich and Paninski, 2016; Pnevmatikakis et al., 2013; Pnevmatikakis et al.,
440 2014; Deneux et al., 2016; Greenberg et al., 2018), and some of these can perform both cell
441 isolation and spike detection simultaneously (Vogelstein et al., 2010; Pnevmatikakis et al.,
442 2016; Pnevmatikakis et al., 2014; Deneux et al., 2016). But the relationship between spik-
443 ing and fluorescence change is not fully understood. For example, the fluorescent indicator
444 will act like an additional calcium buffer within the cell cytoplasm and will compete with
445 the other endogenous buffers to bind with free calcium cells. Therefore, the concentration of
446 those endogenous buffers, and the binding dynamics of those buffers will have an effect on
447 the change in fluorescence in response to an action potential. Furthermore, the binding dy-
448 namics of the fluorescent indicator itself will have an effect on the change in fluorescence. For
449 example, the GCaMP series of fluorescence indicators are based on the calcium buffer pro-
450 tein *calmodulin*. This protein has four binding sites, whose affinities interact non-linearly.
451 But most of the spike inference algorithms model the fluorescence as a linear function of a
452 calcium trace, and they model this calcium trace as a first or second order autoregression with
453 a pulse input to represent action potentials. Deneux et al. (2016) developed a spike inference
454 algorithm with a bit more biological inspiration, but this amounted to a very similar process.
455 While this autoregression idea appears to be a reasonable approximation, the algorithms that
456 use this approximation are outperformed by the most recently published spike inference al-
457 gorithm to be cited here (Greenberg et al., 2018). This algorithm does take into account the
458 binding dynamics of both the endogenous buffers and fluorescent calcium indicator, and the
459 concentrations of free calcium, indicator, and endogenous buffer within the cell cytoplasm.
460 This shows that there is value in more biologically inspired models of fluorescent calcium

461 indicators.

462 In light of the growing popularity of two-photon calcium imaging, and the lack of biolog-
463 ically inspired spike inference algorithms (Greenberg et al. developed their spike inference
464 algorithm in parallel to our work), we decided to develop a biologically inspired model for
465 fluorescent calcium indicator fluorescence. The idea being that our model would take a spike
466 train, or simply spike times, provided by the user, and return the fluorescence trace that would
467 be induced by this spike train or spike times. The model contains parameters for concentra-
468 tions of indicator and endogenous buffers, as well as affinity and unbinding rates for these
469 buffers. There are also parameters for the baseline concentration of free calcium in the cell
470 cytoplasm, and the cell radius (as a means for calculating the cell volume). With this model,
471 we hoped that experimentalists would be able to test out different calcium indicators on the
472 types of spike trains that they expect to encounter. This way they could decide ahead of time
473 which indicator suited their situation best. Since the output of our model is a fluorescence
474 trace, the spike inference models mentioned above can be applied to the modelled fluores-
475 cence. This means that the model could also be used to benchmark the performance of these
476 spike inference algorithms, and to investigate the impact of variations in the model on spike
477 inference accuracy.

478 We have outlined some of the advantages that calcium imaging has over electrophysiolog-
479 ogy. But electrophysiology is more useful in some situations. One particular drawback for
480 two-photon calcium imaging is that it can only be used for imaging near to the surface of the
481 brain. Although imaging with three (or presumably more) photons may solve this problem
482 in the future (Ouzounov et al., 2017). A better option for reading activity from neurons be-
483 yond the surface of the brain is to use Neuropixels probes (Jun et al., 2017). These probes
484 can be used to read from thousands of neurons simultaneously in many different areas of the
485 brain (Allen et al., 2019; Stringer et al., 2019; Steinmetz, Carandini, and Harris, 2019; Stein-
486 metz et al., 2019). This brings us to another problem for which we require new innovations
487 in our analysis methods. Specifically, analysing correlated behaviour in neural ensembles
488 consisting of neurons from many different brain regions.

489 Until the invention of new technologies such as the Neuropixels probes, most elec-
490 trophysiology datasets read from neurons in only one or two regions. Therefore most of
491 the research on interactions between neurons in different regions is limited to two regions
492 (Wierzynski et al., 2009; Patterson et al., 2014; Girard, Hupé, and Bullier, 2001). In chapters
493 3 and 4 we used datasets with neurons from 9 and 5 different brain regions respectively.

494 In light of recent findings based on correlated behaviour showing that spontaneous be-
495 haviours explain activity in many different parts of the brain that would otherwise be regarded
496 as noise (Stringer et al., 2019), that satiety is represented brain wide Allen et al., 2019, and
497 that exploratory and non-exploratory states are represented in the amygdala Gründemann
498 et al., 2019, it was clear that state representation or motor control had an influence on cor-
499 related behaviour in areas of the brain not usually associated with these tasks. Also, given
500 differences in timescales of fluctuations in different brain regions Murray et al., 2014, and
501 different timescales for event representation in different brain regions Baldassano et al., 2017,
502 we decided to investigate brain wide correlated behaviour at timescales ranging from 5ms up
503 to 3s.

504 We started off measuring the correlations in spike counts between individual neurons in
505 our ensemble. These measurements induced a weighted undirected graph where each node
506 represented a neuron, and the weight of each edge was the strength of the correlation be-
507 tween the neurons represented by the nodes at either end of that edge. In order to put the
508 neurons into groups with correlated behaviour, we applied a novel community detection al-
509 gorithm (Humphries et al., 2019) to this graph. We repeated this analysis for timescales from
510 milliseconds to seconds. Bear in mind that our correlation based graph was completely ag-
511 nistic of the anatomical regions in which our cells resided. We then compared our correlated
512 communities to their anatomy at each timescale. In this way, we used a novel method, never
513 applied neuronal data before, to analyse the makeup of correlated communities across dif-
514 ferent regions at different timescales. We found that for short timescales $< 50\text{ms}$ correlated
515 communities tended to exist within anatomical regions, and for longer timescales $> 100\text{ms}$,
516 the correlated communities tended to exist across anatomical regions. This is broadly in
517 agreement with a similar finding for EEG data from humans performing semantic or memory
518 tasks (Stein and Sarnthein, 2000). Von Stein et al. (2000) found that visual processing taking
519 place locally in the visual system was captured in the gamma frequency range (25 – 70Hz),
520 while semantic processing was captured in the beta range (12 – 18Hz), and tasks involving
521 mental imagery and working memory retention were captured in the theta and alpha ranges
522 (4 – 8Hz, and 8 – 12Hz respectively).

523 Many important findings have been made by measuring the correlations between binned
524 spike counts, but there are some problems with this method of analysis. Firstly, the width of
525 the bins used to bin spike times into spike counts has an effect on the magnitude of the cor-
526 relations measured. Using a short bin width can cause your measurements to be artificially
527 small (Cohen and Kohn, 2011). This may not be an issue if one is considering relative size of

correlations when using the same bin width, but it is still not ideal. Secondly, while pairwise correlations can capture most of the information in a small network (up to 40 cells) of highly correlated cells (Schneidman et al., 2006), a model based on pairwise correlations alone will fail to capture the activity of larger (~ 100 cells) networks, higher order correlated activity is required (Ganmor, Segev, and Schneidman, 2011). One problem with these higher order correlations is that they may be defined in different ways (Staude, Grün, and Rotter, 2010). Furthermore if we want to include them in a model this usually involves greatly increasing the number of parameters to fit, which increases the dimension of the parameter space leading to the ‘curse of dimensionality’. Some models attempt to sidestep these problems while still capturing higher-order correlations. These models attempt to capture the relationship between each individual neuron in the ensemble, and the ensemble as a whole. Okun et al (2015) called the strength of this relationship the ‘population coupling’, and demonstrated that this quantity can predict an individual neuron’s response to optogenetic stimulation of the whole ensemble. They also showed that this quantity was an indicator of the neuron’s synaptic connectivity (**okun**). With the ‘population tracking model’, O’Donnell et al. (2016) linked the probability of firing an action potential for each individual neuron with the distribution of the number of active neurons. This allowed model fitting for a large number of neurons, as well as calculation of full pattern probabilities, and population entropy (O’Donnell et al., 2017).

In this work, we also aimed to capture correlated behaviour between the neurons in a neuronal ensemble without measuring correlations directly. Correlation coefficients capture the linear component of the relationship between two random variables, but will not measure any relationship beyond linearity. Also, measuring correlation coefficients using short timebins can be difficult for neuronal data (Cohen and Kohn, 2011). We decided to abandon correlation, and we aimed to quantify a more general concept of association by modelling the number of active neurons in the ensemble using a Conway-Maxwell-binomial (COMb) distribution (Kadane, 2016).

The COMb distribution is a probability distribution over the number of successes in a sequence of Bernoulli trials, where these trials can be associated in some way. The COMb distribution is an extension of the standard binomial distribution, with an additional parameter to model association between the Bernoulli variables. Using this additional parameter the distribution can capture positive association, where the Bernoulli variables tend to take the same value, negative association, where the Bernoulli variables tend to take opposite values, or no association i.e. the standard binomial distribution.

562 We fit a COMb distribution to spike sorted electrophysiological data taken from five
563 different regions in the brain of an awake mouse exposed to visual stimuli Steinmetz et al.,
564 2019. We examined whether or not a model based on the COMb distribution was able to
565 capture changes in the number of active neurons in these neuronal ensembles in response to
566 the stimuli. We also investigated the relationship between the changes as captured by the
567 COMb model and the change in neural variability as measured by Churchland et al. in their
568 famous paper (Churchland et al., 2010).

569 Our overall aim was to investigate some of the challenges in analysing large ensembles
570 of neurons present today. That included collecting the data to analyse (via calcium imaging),
571 and subsequently analysing these data. We felt that this was a worthwhile project because
572 the size of datasets, in terms of numbers of neurons and data collected, is growing rapidly.
573 Consequently these challenges will only become greater unless they are addressed. This is
574 our attempt at addressing them.

575 **Chapter 2**

576 **Sensitivity of the**
577 **spikes-to-fluorescence transform to**
578 **calcium indicator and neuron**
579 **properties**

580 *Abstract*

581 Fluorescent calcium indicators such as GCaMP are widely used to monitor neuronal activity.
582 However the relationship between the fluorescence signal and the underlying action potential
583 firing is poorly understood. This lack of knowledge makes it difficult for experimenters
584 to decide between different indicator variants for a given application. We addressed this
585 problem by studying a basic biophysical model of calcium dynamics in neuronal soma. We
586 fit the model parameters to publicly available data where GCaMP6s fluorescence and whole-
587 cell electrophysiological recordings were made simultaneously in the same single neurons.
588 We systematically varied the model's parameters to characterise the sensitivity of spike train
589 inference algorithms to the calcium indicator's main biophysical properties: binding rate,
590 dissociation rate, and molecular concentration. This model should have two potential uses:
591 experimental researchers may use it to help them select the optimal indicator for their desired
592 experiment; and computational researchers may use it to generate simulated data to aid design
593 of spike inference algorithms.

594

2.1 Introduction

595 Although fluorescent calcium indicators such as GCaMP are widely used to monitor neuronal
596 activity, the relationship between the fluorescence signal and the underlying action potential
597 firing is imperfect. The fluorescence signal has a low signal-to-noise ratio, and most indi-
598 cators' kinetics are slow relative to the millisecond-timescale dynamics of the membrane
599 voltage (example in Figure 1). This makes spike inference difficult. Furthermore, the effects
600 of the indicator and cell properties on the fluorescence signal are unknown. For example,
601 genetically encoded indicators can accumulate within neurons over weeks and months (Chen
602 et al., 2013). Studies using calcium-sensitive fluorescent dyes have shown that indicator con-
603 centration has substantial effects on the spike-to-fluorescence relationship (Maravall et al.,
604 2000). Therefore spike rates inferred from GCaMP fluorescence signals may give mislead-
605 ing results if comparing across imaging sessions. More generally, the poor understanding of
606 the spike-to-fluorescence transform means experimenters may not know whether to trust the
607 outputs of spike train inference methods in any given application.

608 Spike trains are usually inferred from the time series of intensity values of one pixel of the
609 fluorescence image, where the pixel is located at the cell's soma. The problems of identifying
610 these pixels, and inferring spikes from their time series can solved separately or together.
611 When attempting to infer spikes, the fluorescence trace is modelled as a linear combination of
612 calcium concentration dynamics, a baseline calcium concentration, and some Gaussian noise.
613 The calcium concentration dynamics are modelled as an autoregressive process of degree 1
614 or 2 with a pulse input corresponding to the spike train, or the number of spikes fired in a
615 time step. The model includes no dynamics for the fluorescent indicator itself. Furthermore,
616 in order to make this model into an easily solvable linear programming problem the number
617 of spikes fired in a timestep is not restricted to non-negative integers but to arbitrary non-
618 negative values (Vogelstein et al., 2010; Pnevmatikakis et al., 2016; Friedrich and Paninski,
619 2016; Pnevmatikakis et al., 2013; Pnevmatikakis et al., 2014). More biologically inspired
620 spike inference models do exist (Deneux et al., 2016), but their fundamentals are very similar.
621 In this work, we investigated the effect of changing dynamics and buffer concentrations on
622 the accuracy of the inference algorithms based on these models.

623 The aim of this project was to model the fluorescence traces produced by a fluorescent
624 calcium indicator in a neuron soma resulting from a specific spike train, given calcium indi-
625 cator parameters such as binding rate, dissociation rate, and molecular concentration. Such

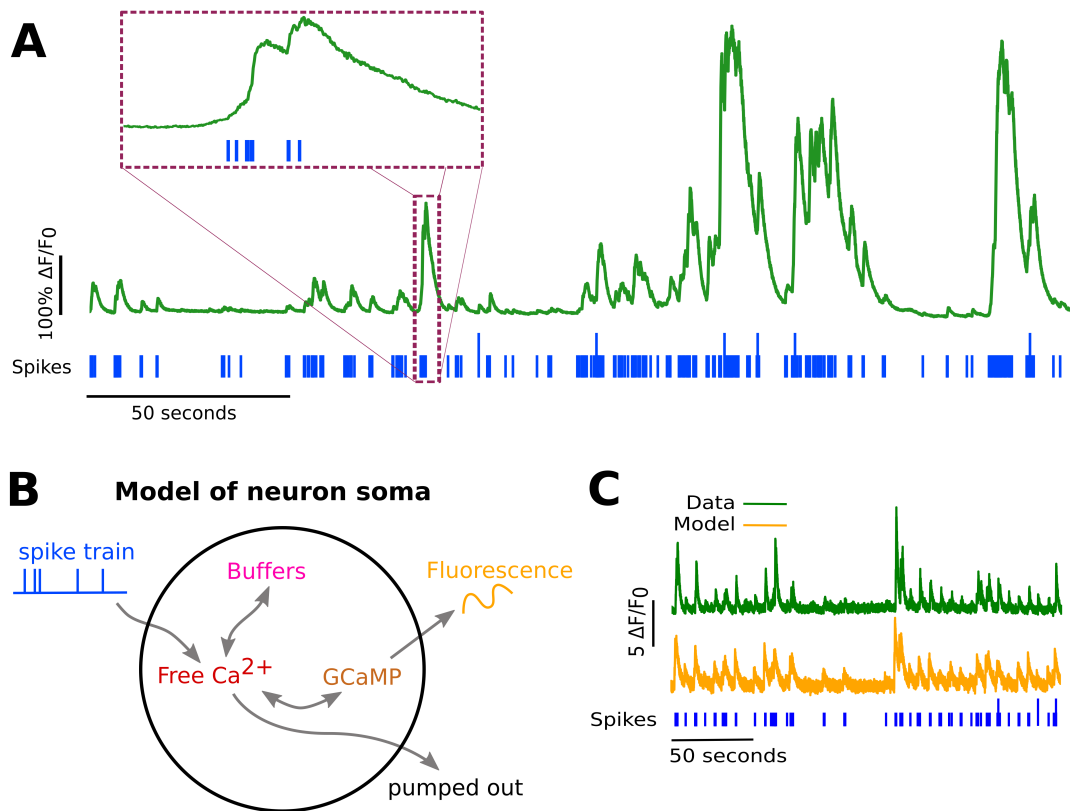


FIGURE 2.1:

A: Example spike train (blue) and the corresponding GCaMP6s fluorescence trace (green), data replotted from (Berens et al., 2018). Inset shows zoomed section of traces to highlight slow decay of GCaMP6s fluorescence relative to spike time intervals.

B: Schematic diagram of the neuron calcium and GCaMP computational model.

C: Good visual match of data fluorescence trace (green) and model simulated fluorescence (orange) in response to an identical spike train (blue).

626 a model would allow benchmarking of various spike inference algorithms, and enable under-
627 standing of how indicator characteristics affect the quality of spike train inference.

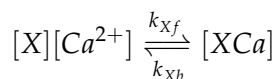
628 The model we developed consisted of free calcium, fluorescent indicator molecules, and
629 mobile and immobile endogenous calcium buffers. The indicator molecules which were
630 bound to a calcium molecule could be either excited, i.e. able to release a photon, or relaxed.
631 In order to reproduce the noise inherent in the data collection, we modelled the release of
632 photons from the excited indicator bound calcium as a stochastic process.

633 The fluorescence traces produced by the simulation were calibrated to reproduce the
634 signal-to-noise ratio observed in experimental data. Previously published spike inference
635 algorithms were then used to infer spike trains from the experimental fluorescence traces and
636 the modelled fluorescence traces. The parameters of the model were then varied in order to
637 determine the effect on the system dynamics and the effects on spike inference.

638 2.2 Results

639 2.2.1 A biophysical computational model can generate accurate fluorescence 640 traces from spike trains

To study the relationship between action potential firing and calcium fluorescence, we built a computational model of calcium dynamics in a neuronal soma. The model consisted of four dynamic variables: the concentration of free calcium, two types of endogenous buffer, and the calcium-sensitive fluorescent indicator. Each of the buffers and the indicator could independently bind and unbind with calcium. These reactions were modelled as



641 where X is the buffer concentration and Ca^{2+} is the calcium concentration. Each species
642 could therefore exist in two states: either bound with calcium or unbound. To model the
643 imaging process, we also added a third, excited state to the indicator. When in the calcium-
644 bound state, the indicator could be converted to an excited state, corresponding to the absorp-
645 tion of a photon. The rate of this excitation process could be interpreted as the intensity of
646 the light illuminating the sample. Once excited, the species decayed back to the unexcited
647 state at a fixed rate, corresponding to the spontaneous emission of photons. The total emitted
648 fluorescence signal was interpreted as proportional to this de-excitation flux. To represent
649 experimental noise in the photon capture process, we drew a random number of captured

650 photons at each time step from a binomial distribution, parameterised by a number p that
651 corresponds to the mean fraction of released photons that are captured.

652 The model had 17 parameters in total describing the molecules' concentrations and re-
653 action rates (Methods). We set 13 of these parameters to values from the literature. The
654 remaining 4 parameter values we fit to publicly-available data (Berens et al., 2018), briefly
655 explained as follows (see Methods for full details). Single neurons from acute rat cortical
656 slices expressing GCaMP6f were imaged with two-photon microscopy while the membrane
657 potentials of the somata of the same neurons were simultaneously recorded via whole-cell
658 patch clamp electrophysiology. In this dataset, the electrical recordings give unambiguous
659 information about neurons' spike times. To do the parameter fitting, we feed these spike
660 trains as inputs to the computational model. After running, the model returns a simulated
661 fluorescence trace. We aimed to find the model parameter values that give the best match
662 between this simulated fluorescence trace and the real fluorescence time series recorded in
663 the corresponding neuron. To do this we used a suite of optimisation procedures to jointly
664 fit both the real neuron's fluorescence time series and power spectrum, which capture com-
665 plementary information about the spikes-to-fluorescence mapping (Methods). We performed
666 the fitting procedure independently for each of the 20 neurons in the spikefinder dataset
667 (<http://spikefinder.org>). After fitting, the model produced realistic-looking fluorescence time
668 series (Figure 2.1).

669 **2.2.2 Spike inference algorithms perform similarly on real data compared with**
670 **time series simulated from the model**

671 Researchers often pass the fluorescence time series through a spike inference tool before per-
672 forming further statistical analyses. These spike inference algorithms take the fluorescence
673 trace as input and attempt to estimate the neuronal spike train that triggered them (Vogelstein
674 et al., 2010; Pnevmatikakis et al., 2016; Friedrich and Paninski, 2016; Pnevmatikakis et al.,
675 2013; Pnevmatikakis et al., 2014; Deneux et al., 2016). Part of our motivation for building
676 this model was to allow us to ask the question: how do the properties of the cell and the
677 calcium indicator affect the quality of spike inference? In order to trust the conclusions from
678 our model, we should first be confident that spike inference from our simulated fluorescence
679 traces is similar to that from the real data. To test this we passed each of the simulated fluores-
680 cence traces through three previously published spike inference algorithms, quantified their
681 performance against the ground-truth electrophysiology data, repeated the procedure for the
682 real calcium fluorescence time series, and compared the accuracy of the inference processes

in all cases. The *true positive rate*, also known as the *recall*, the *sensitivity*, or the *probability of detection* of spike inference varied across the three inference algorithms we tried (p value and statistical test here). The constrained non-negative matrix deconvolution algorithm (Pnevmatikakis et al., 2016) (CNMD algorithm) correctly detected approximately 45% of the true spikes, the OASIS algorithm (Friedrich and Paninski, 2016) correctly detected approximately 35% of the true spikes, and the ML spike algorithm (Deneux et al., 2016) correctly detected approximately 15% of the true spikes (see figure 2.2). Notably, for two of the three inference algorithms, the quality of inference was also fairly consistent for individual spike trains, not just the group means ($p > 0.05$, paired t-test). This demonstrates that the models were generating fluorescence time series that were similarly difficult to decode as the real data, in ways that were not specific to any one inference algorithm. This is evidence that the models captured real aspects of the spikes-to-fluorescence transform.

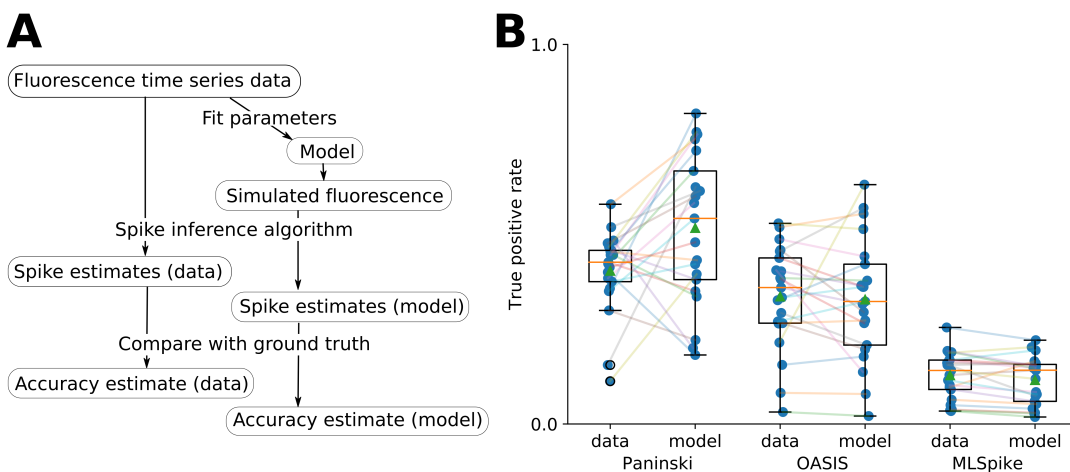


FIGURE 2.2:
A: Workflow to compare spike inference for real versus simulated fluorescence data.
B: True positive rates achieved by three different spike inference algorithms when applied to observed spike trains, and simulated spike trains. Data points overlaid as blue circles. The performance is similar from real and simulated data for each of the algorithms.

694

695 2.2.3 Relative effects of various buffers to the fluorescence signal

696 One of the benefits of computational models over laboratory experiments is that we can
697 observe all the variables in the simulation to gain insight into the system's dynamics, which
698 can be difficult to do in the lab. We plotted the concentrations of the various species over
699 time for a version of the model fit to one data set, in response to the same train of spikes used
700 for fitting (figure 2.3). Figure 2.3a shows the absolute values of the species concentrations,

701 summed. Consistent with experimental estimates (Maravall et al., 2000), only a small fraction
702 ($\sim 0.1\%$) of calcium is free and unbound to any buffer. Of the bound calcium, the vast
703 majority, ($\sim 96\%$) is bound to the GCaMP indicator. The two types of endogenous buffer
704 are bound to the remaining calcium ($\sim 4\%$). An influx of calcium from a single spike adds
705 very little to the total calcium, in relative terms (red line in Figure 3a).

706 When calcium entered the model neuron it was rapidly buffered (Bartol et al., 2015).
707 However the relative fractions of which buffer molecules bound to the influxed calcium was
708 dynamic, and changed over time . Figure 2.3 (b-f) shows the time course of the various
709 species over time in response to a calcium influx event from a single action potential. Cru-
710 cially, the indicator $[BCa]$ competed with the endogenous buffers $[ImCa]$ and $[ECa]$ – all
711 three bind calcium on similar timescales. This implies that the timecourse and amplitude of
712 the $[BCa]$ variable will also depend on the binding rates and availabilities of the endogenous
713 buffers. For example if we decreased the concentration of an endogenous buffer, we might
714 expect both a faster rise time and greater peak amplitude of the $[BCa]$ signal in response to
715 a calcium influx event. The slowest component of the decay had a similar time constant for
716 $[BCa]$, $[ImCa]$ and $[ECa]$, which in turn matched the $[Ca]$ extrusion time constant in our
717 model ($\sim 6.29 \times 10^{-22} \text{Ms}^{-1}$). This implies that the buffers and the indicator had reached
718 a dynamic equilibrium and were jointly tracking the free calcium concentration as calcium
719 was slowly extruded from the cell.

720 Interestingly the excited bound calcium species ($[BCa^*]$) showed a qualitatively different
721 timecourse in response to a calcium influx event. This concentration is subject to the added
722 ‘excitation and release’ dynamic, where a certain proportion of the concentration absorbs the
723 energy from an incoming photon and goes into an ‘excited state’ at each time step. A certain
724 proportion of the concentration releases a photon and reverts to a ‘relaxed state’ at each
725 timestep also. This means that the excited bound calcium lags behind the bound calcium
726 trace. We could think of the excited bound calcium trace as a low pass filtered version of the
727 bound calcium trace.

728 2.2.4 Spike inference accuracy is sensitive to indicator properties, and likely 729 varies within and between cells

730 The above results imply that the fluorescence signal depends on the relative properties of
731 both GCaMP and the endogenous buffers. We next used the model to directly ask how
732 sensitive spike inference was to these components. We focused on three key parameters that

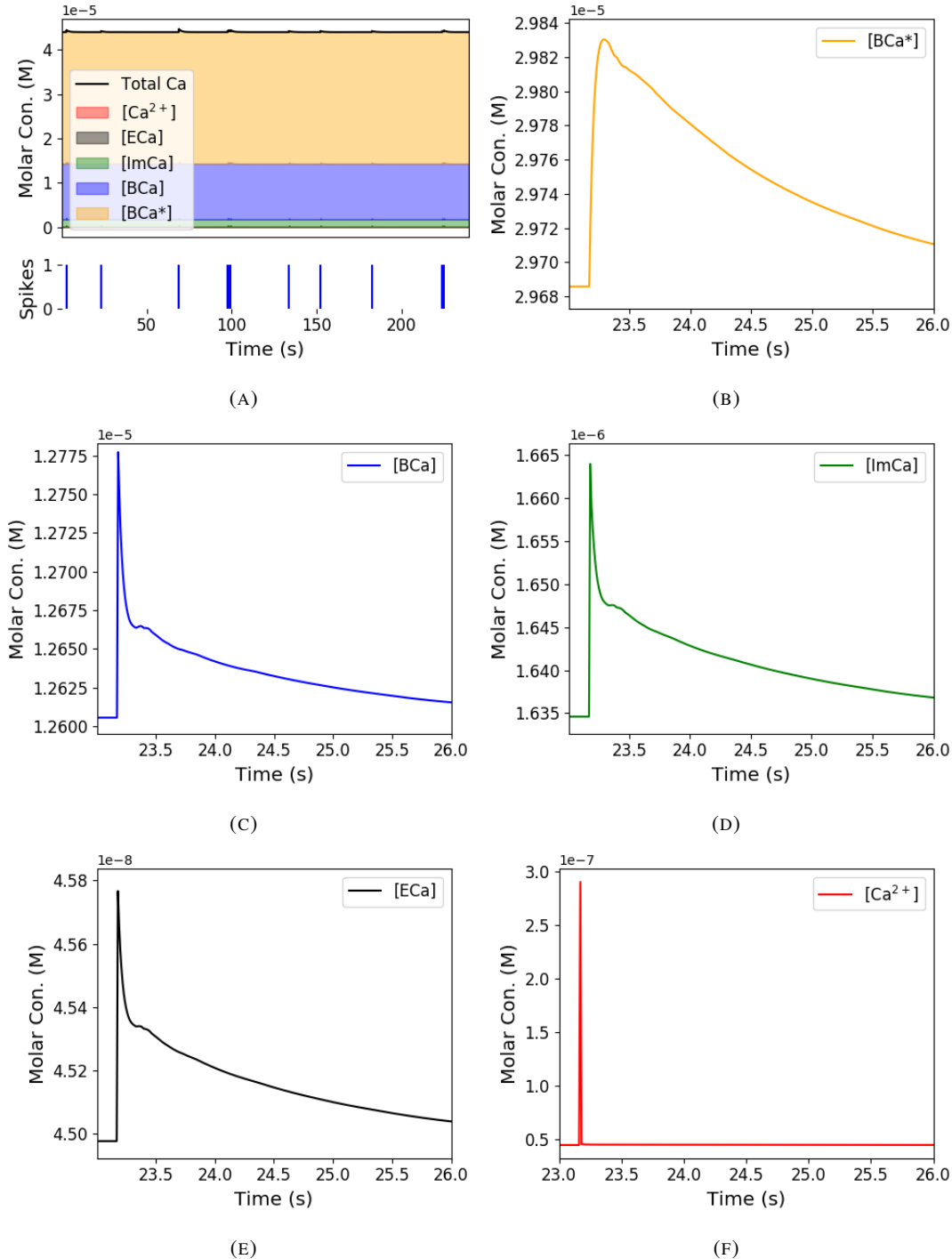


FIGURE 2.3: **Calcium Buffering Dynamics** (a) The proportions of bound and free calcium concentrations within a cell, with the associated spike train. (b)-(f) The dynamics of the concentration of (b) excited indicator bound calcium, (c) indicator bound calcium, (d) immobile endogenous buffer bound calcium, (e) mobile endogenous buffer bound calcium, and (f) free calcium in response to an action potential at ~ 23.2 s.

733 likely vary from cell to cell and experiment to experiment: GCaMP binding kinetics, GCaMP
734 concentration, and endogenous buffer concentration.

735 Several variants of GCaMP itself have been made that differ in calcium binding kinetics,
736 baseline fluorescence, fluorescence efficiency, and other factors. For example, GCaMP6f has
737 a decay time constant of ~ 1 s, while GCaMP6s has a decay time constant of ~ 2 s (Chen
738 et al., 2013). Here we asked how these differences in binding kinetics affect spike inference.
739 We jointly varied the calcium binding and unbinding rates of the indicator by the same factor
740 over a range from 100-fold slower to 100-fold faster from the fitted values, and simulated the
741 fluorescence response for each of the parameter settings in response to the same spike trains
742 as before (figure 2.4). Notably this manipulation does not affect the indicators affinity, and
743 therefore would not affect steady-state responses to prolonged changes in calcium. Instead
744 it is likely to affect its sensitivity to the spike train dynamics. We computed two summary
745 measures from the simulated fluorescence traces: the signal-to-noise ratio for a single spike
746 (Methods, section 2.4.6), and the accuracy of spike inference for each of the spike trains. We
747 observed a reduction in the signal-to-noise ratio and the spike inference quality when we set
748 the binding and unbinding rates were set to one hundredth of their fitted values, and to one
749 tenth of their fitted values. When we increased the value of both binding rates, we observed
750 no change in these measurements. The reduction in both rates lead to smaller increases in
751 fluorescence in response to an action potential and a longer decay time (figure 2.4a), this
752 caused the reduction in signal-to-noise ratio. As both rates were increased, the change in
753 $\Delta F/F_0$ in response to an action potential increased and the decay time decreased slightly,
754 but the fluorescence trace created by these values was very similar to the trace created by the
755 fitted values.

756 Second, the overall concentrations of GCaMP often varies from cell to cell. For exam-
757 ple different cells, even of the same type in the same tissue, can express different levels of
758 GCaMP, due to proximity to the infection site, or the cell becoming ‘nuclear-filled’ (Tian et
759 al., 2009; Chen et al., 2013). Also, GCaMP is often used for longitudinal experiments where
760 the same cells are re-imaged across multiple days or weeks. However since GCaMP expres-
761 sion typically ramps up over time (Chen et al., 2013), the accuracy of spike inference may
762 differ across multiple longitudinal recordings in the same cell. We addressed this by varying
763 the concentration of calcium indicator in the model, simulating spike trains and measuring
764 signal-to-noise ratio and spike inference accuracy on the resulting fluorescence traces. Both
765 increasing and decreasing the concentration of the indicator had effects on the fluorescence

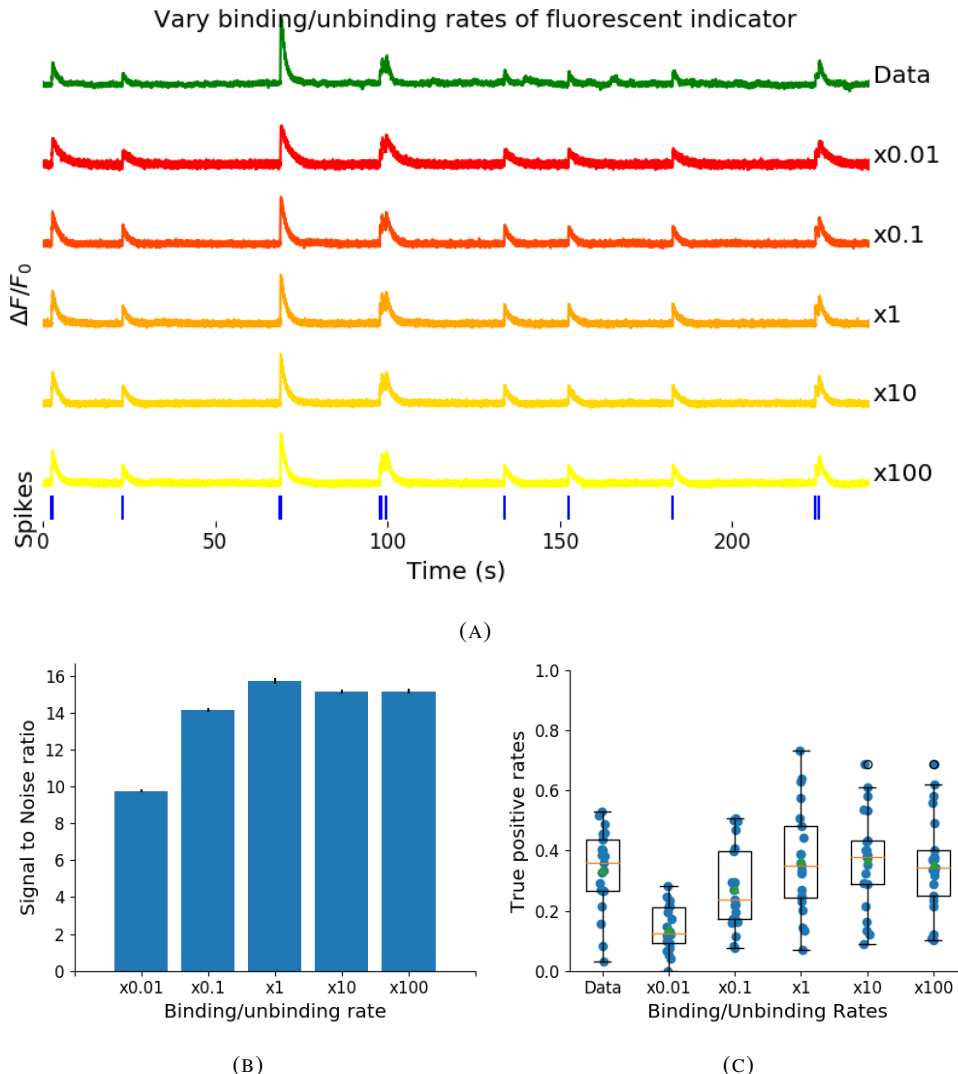


FIGURE 2.4: (a) An example trace for each of the five pairs of values used for the binding and unbinding rates of the fluorescent calcium indicator. (b) The signal-to-noise ratio of the modelled fluorescence traces using each of the four perturbed values, and the experimental value. The SNRs for the two pairs with values lower than the experimental value are lower than the experimental pair or the higher value pairs. (c) The true-positive rates of the deconvolution algorithm's predictions when inferring from the observed data, and inferring from modelled traces using the perturbed and experimental values.

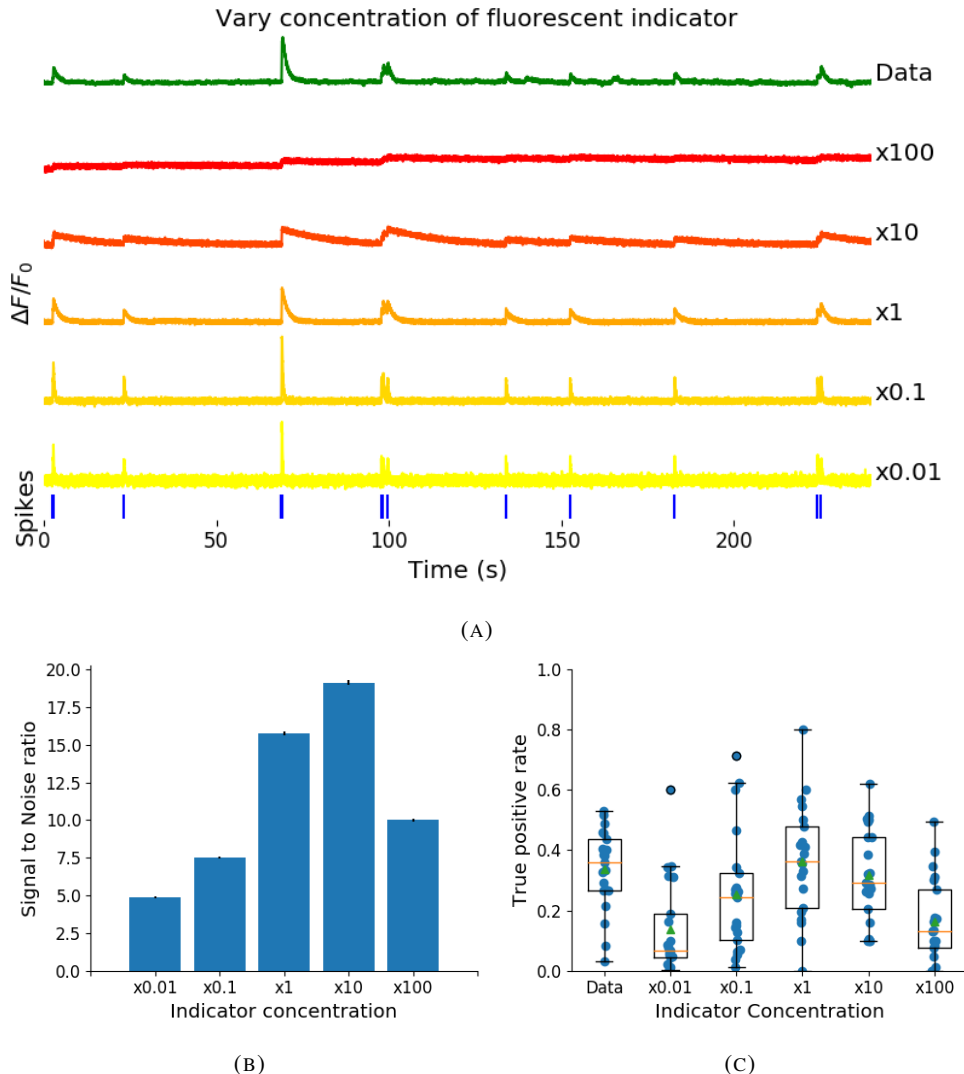


FIGURE 2.5: (a) An example trace for each of the five perturbed values for the concentration of fluorescent calcium indicator. The top two traces are produced by the lower perturbed values, the middle trace is produced by the experimental value, and the lowest two traces are produced when using the higher perturbed values. (b) The signal-to-noise ratio of the modelled fluorescence traces using each of the four perturbed values, and the experimental value. Extreme perturbations of the concentration either above or below the experimental level lowered the SNR. (c) The true-positive rates of the deconvolution algorithm's predictions when inferring from the observed data, and inferring from modelled traces using the perturbed and experimental values. We found that the algorithms performs equally badly on the two most extreme values, and performs equally well on the experimental value, and the next higher perturbed value.

766 trace, signal-to-noise ratio, and spike inference. The signal-to-noise ratio and spike inference
767 quality decreased with decreased indicator concentration, and both showed a decrease
768 when the indicator concentration was increased to 100 times its fitted value (figure 2.5).
769 The signal-to-noise ratio showed an increase when the indicator concentration was increased
770 to 10 times its fitted value, but there was no corresponding change in the spike inference
771 quality. The decrease in indicator concentration caused a reduction in the increase in $\Delta F / F_0$
772 in response to an action potential, and an increase in the decay time of this increase (figure
773 2.5a). The increase in indicator concentration had the opposite effect, it caused an increase
774 in the change in $\Delta F / F_0$ in response to an action potential, and a decrease in the decay time.

775 Third, the concentration and types of endogenous calcium buffers also vary from neuron
776 to neuron, both within and between cell types (Bartol et al., 2015; Maravall et al., 2000;
777 Neher and Augustine, 1992). Since the calcium buffer capacity of neurons is high, around
778 50-70 (Lee et al., 2000) in excitatory hippocampal pyramidal cells, around 100-250 (Lee et
779 al., 2000) in inhibitory hippocampal pyramidal cells, and 900-200 in Purkinje cells (depend-
780 ing on the age of the subject), these endogenous buffers compete with GCaMP for binding
781 to calcium, and variations in endogenous buffer concentration may affect GCaMP signal and
782 therefore spike inference. To address this we varied the concentration of the endogenous
783 buffer in the model neuron over five orders of magnitude from 0.8 to 8000 μM , simulated
784 calcium fluorescence traces in response to the same set of spike trains, and performed spike
785 inference on the resulting fluorescence time series. Increasing the endogenous buffer con-
786 centration had a substantial effect on the GCaMP fluorescence signal, both decreasing its
787 amplitude and slowing its kinetics (figure 2.6(a)). This corresponded with a decrease in both
788 single-spike signal-to-noise ratio (figure 2.6(b)) and spike inference accuracy (figure 2.6(c)).
789 In contrast, decreasing endogenous buffer capacity from the fitted value had little effect on
790 either the GCaMP signal or spike inference (figure 2.6).

791 **2.2.5 Single spike inference accuracy drops for high firing rates, but firing rate
792 itself can be estimated from mean fluorescence amplitude**

793 The fluorescence signal recorded from neurons using calcium indicators is typically much
794 slower than changes in membrane potential for two reasons: first, because the calcium and
795 the indicator have slow binding and unbinding kinetics, the signal is a low-pass filtered ver-
796 sion of the membrane potential. Second, neuronal two-photon imaging experiments are often
797 performed in scanning mode, which limits their frame rate to $\sim 10\text{Hz}$ or slower. This im-
798 plies that multiple spike events that occur close in time might be difficult to resolve from a

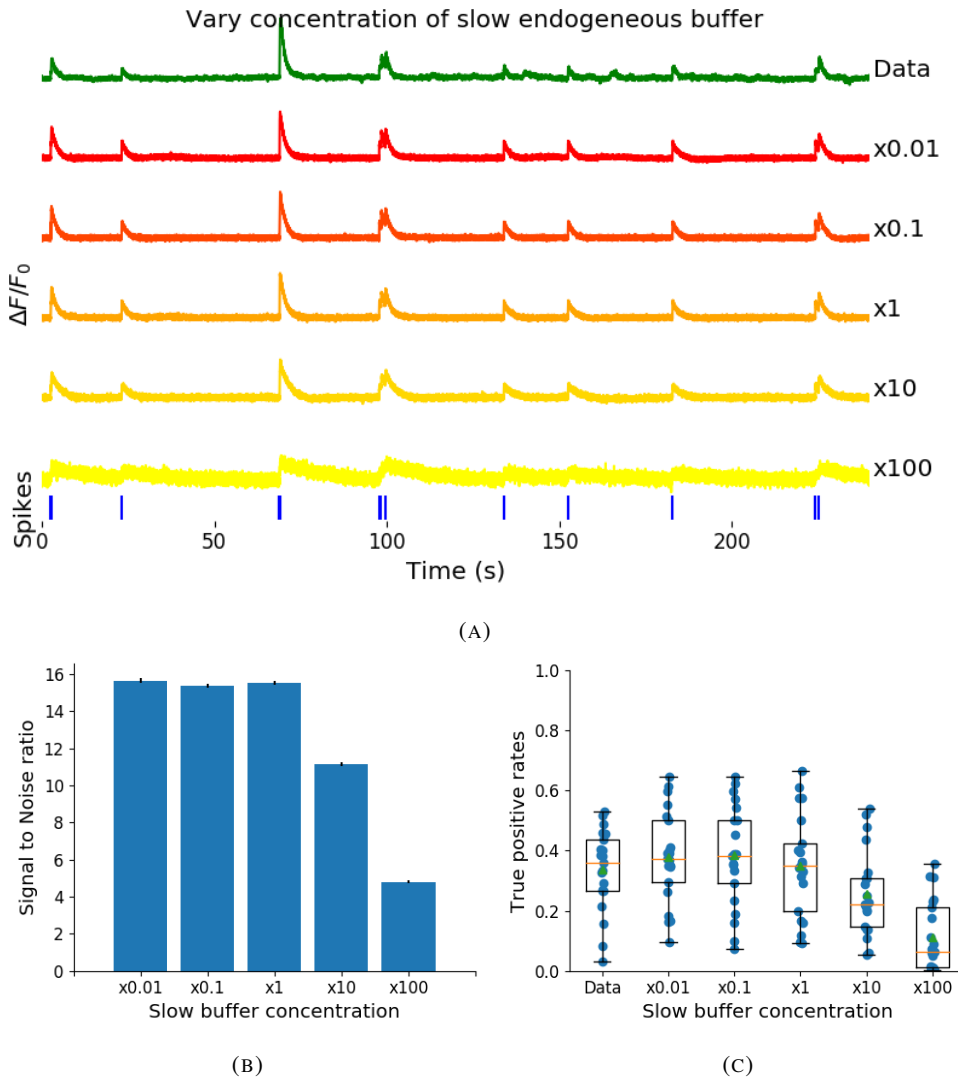


FIGURE 2.6: (a) An example trace for each of the five perturbed values for the concentration of immobile endogenous buffer. (b) The signal-to-noise ratio of the modelled fluorescence traces using each of the four perturbed values, and the experimental value. The lower values for the immobile buffer produce the same SNR as the experimental value. But the higher perturbed values produce fluorescence traces with a lower SNR. (c) The true-positive rates of the deconvolution algorithm's predictions when inferring from the observed data, and inferring from modelled traces using the perturbed and experimental values.

799 calcium indicator time series. Many cells, especially several types of inhibitory interneurons,
 800 fire tonically at rates higher than 10Hz. We used the model to test whether spike inference
 801 accuracy depended on the neuron's firing frequency by driving the cell with spike trains sam-
 802 pled from a Poisson processes of varying frequency. We simulated a variable firing rate using
 803 an Ornstein-Uhlenbeck process, and simulated the spike trains using a Poisson distribution
 804 with its rate taken from this process. Because of the high frequency firing rate of these spike
 805 trains, we used the accuracy as the measure of spike inference quality. We simulated 30
 806 spike trains at average firing rate of 1, 5, and 10Hz, and measured the spike inference quality
 807 of all these traces. Spike inference accuracy decreased with increasing firing rate, for up to
 808 10Hz Poisson spike trains (figure 2.8(left)). Although, the accuracy remained above 90% for
 809 each of the three frequencies. We also plotted the average $\Delta F/F_0$ as a function of stimula-
 810 tion firing rate. We found that it increased monotonically as a function of firing rate (figure
 811 2.8(right)).

812 We expected lower spike inference quality as the average spiking frequency increased.
 813 Since the fluorescence trace, in some sense, is a low pass filtered version of the spike train, a
 814 tightly packed groups of spikes will be more difficult to infer than isolated spikes. However,
 815 the increasing amplitude of the fluorescence trace with increasing frequency suggests that
 816 some spike inference algorithm could be developed based on this amplitude.

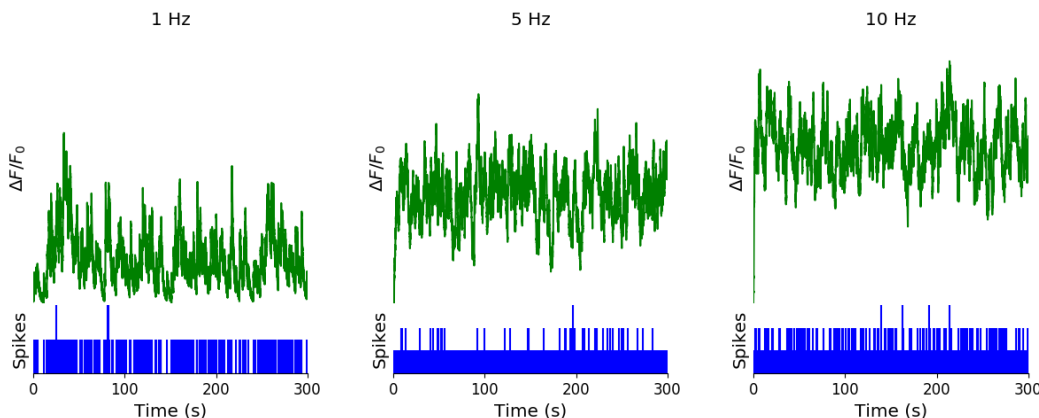


FIGURE 2.7: **Simulating fluorescence traces at different firing rates** Example modelled traces created using simulated spike trains with a mean fir-
 ing rate of 1Hz (left column), 5Hz (middle column), and 10Hz (right col-
 umn). Note the difference in amplitude with different mean firing rates.

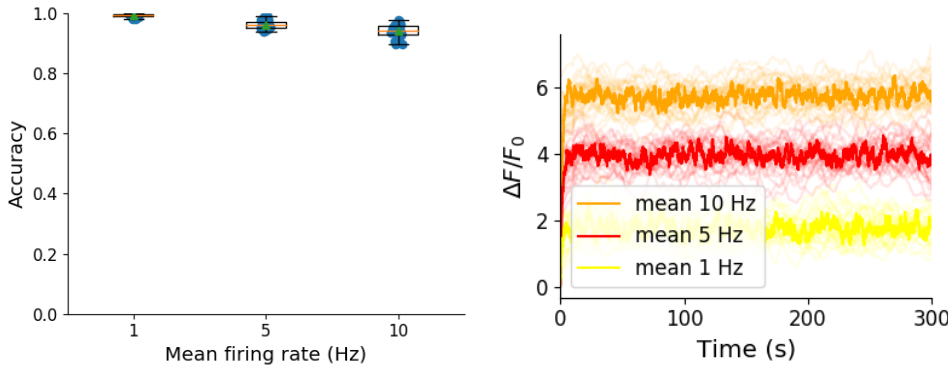


FIGURE 2.8: **Inference quality and $\Delta F/F_0$ vs Firing rate** (left) The spike inference accuracy when applied to 30 traces created using simulated spike trains with mean firing rates of 1, 5, and 10 Hz. (right) The mean $\Delta F/F_0$ across those 30 traces for each frequency.

817 2.3 Discussion

818 We designed a biophysical model for the changes in free calcium and bound calcium con-
 819 centrations within a cell soma with a fluorescent calcium indicator. We used this model to
 820 model the fluorescence trace resulting from a spike train in this cell. We fit the free parame-
 821 ters of the model by matching the power spectrum and amplitude of fluorescence traces with
 822 simultaneously measured spike trains. We inferred spikes from real fluorescence traces and
 823 modelled fluorescence traces, and measured the quality of the spike inference in both cases.
 824 We found that the spike inference quality was similar in both cases. We perturbed the concen-
 825 tration of the calcium buffers in the model, and the binding/unbinding rates of those buffers
 826 in the model, and measured the effect on the signal-to-noise ratio (SNR) of the modelled
 827 fluorescence traces and the spike inference quality.

828 For the fluorescent calcium indicator, we found that any large perturbation away from
 829 the experimental value led to a reduction in SNR, and spike inference quality. For the bind-
 830 ing/unbinding rates, we kept the ratio of these rates constant, but altered their values in paral-
 831 lel. The lower values caused a reduction in SNR, and a reduction in spike inference quality.
 832 For the endogenous buffer concentration, an increase above the experimental value caused a
 833 reduction in SNR and spike inference quality.

834 Although the model produced visually similar time series to the real data, there were a
 835 few aspects it did not capture. First, the real data featured some low-frequency components
 836 that did not appear related to the spike events. These were not captured by the models we
 837 used in this study, but could be added in future by adding a suitable low-frequency term to the
 838 resulting time series. Second, the real data seemed to have some nonlinearities not captured in

839 the model, for example the response to two nearby spikes was greater than expected from the
840 linear sum of two single spikes. This may be due to the co-operative binding of Calmodulin
841 to calcium, which gives calmodulin a supra-linear sensitivity to calcium concentration. The
842 model, in contrast behaved much more linearly, but could be extended in future to include
843 such nonlinearities. Third, in the real data the fluorescence peak amplitude seemed to vary
844 from spike to spike, even for well-isolated spike events. However in our model we assumed
845 each spike lead to the same fixed-amplitude injection of calcium to the cell, leading to much
846 greater regularity in fluorescence peak amplitudes. This variability could be added in future
847 versions of the model by making the injected calcium peak a random variable. Fourth, we
848 modelled the soma as a single compartment, but in reality there is likely a non-uniform spatial
849 profile of calcium concentration. This may matter because some endogenous buffers might
850 access calcium right as it influxes from the extracellular space, whereas the majority of the
851 fluorescence signal is more likely coming from the bulk of the cytoplasm. Future models
852 could attempt to model these spatial dependencies to assess whether they affect the overall
853 spike inference procedure.

854 As well as the optimised parameters, the model has 14 fixed parameters than can be
855 changed to simulate different types of calcium indicators. This model could be used to test
856 the theoretical performance of proposed new types of calcium indicator. The model could
857 also be used by developers of spike inference algorithms to test the effects of changing cal-
858 cium indicator parameters on spike inference, or to test the affects of changing spiking char-
859 acteristics on spike inference. For example, high firing rate vs low firing rate, or bursting vs
860 no bursting. Given the increasing amplitude of the fluorescence trace with increasing mean
861 firing rate, it would be possible to build a spike inference algorithm on this principle at least
862 in part.

863 Our model has already been used as a tool by our colleagues, for simulating fluorescence
864 traces in response to cells that can fire with a continuous rate between 10 and 20Hz, but do
865 not always do so. Our colleagues found that a combination of the amplitude and the variance
866 of the simulated fluorescence trace was the best indicator of firing rate. For example, when
867 a cell was not firing, the amplitude and variance of the fluorescence trace was relatively low.
868 When the cell fired with a low firing rate \sim 1Hz, the mean amplitude was still low but
869 the variance of the fluorescence trace was high, and for high firing rate \sim 10 – 20Hz, the
870 fluorescence amplitude was high, and the variance was low. In this way, our model may be
871 useful for investigating firing rates underlying real fluorescence traces in response to cells
872 which can fire in these rage ranges.

873 A recent paper by Greenberg et al (2018) described a biophysical model for spike train
874 inference called the ‘Sequential binding model’. Similar to our model, this model included
875 parameters for two types of endogenous buffer. But this model also included dynamics for
876 calcium binding to and unbinding from these endogenous buffers. Furthermore, this model
877 included dynamics for calcium binding to and unbinding from the four binding sites present
878 on a GCaMPs6 molecule. In the accuracy measurements specified in that paper, this model
879 performed better than the MLspike algorithm, which is also partially a biophysically model,
880 and it performed better than the constrained non-negative deconvolution algorithm. The se-
881 quential binding model also biophysically interpretable parameters, and its fitted parameters
882 for quantites such as buffering capacity and calcium influx upon action potential firing fall in
883 line with experimental values (Greenberg et al., 2018). Biophysical models like this appear
884 to be the way forward for spike inference algorithms.

885 **2.4 Methods**

886 **2.4.1 Calcium dynamics model**

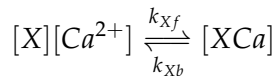
887 We wrote a biophysical model of the calcium dynamics within a cell soma. When a neu-
888 ron fires an action potential, voltage-dependent calcium ion-channels open up that allow a
889 current of Ca^{2+} to flow into the neuron (Koch, 1999). The increase in the free calcium ion
890 concentration inside of the cell, along with changes in the concentration of potassium and
891 sodium, causes the change in cell membrane potential, which must be depolarised. The de-
892 polarising process consists of free calcium ions leaving the cell through open ion channels,
893 or binding to molecules within the cell called buffers, or calcium storage by organelles such
894 as the endoplasmic reticulum. A diagram illustrating the cell, its channels, and its buffers
895 can be seen in figure 2.1A. There are several different types of calcium buffer, each with
896 different dynamics and different concentrations within different types of excitable cell. The
897 fluorescent calcium indicator is another calcium buffer, with the useful property that when it
898 is bound to a calcium ion, the bound molecule may become excited by a photon and release
899 a photon in return. This is what creates the fluorescence. After the action potential has taken
900 place, the free calcium concentration within the cell will return to a baseline level (Maravall
901 et al., 2000).

902 We modelled the the dynamics of five molecular concentrations,

- 903 • Free calcium ion concentration, $[\text{Ca}^{2+}]$

- 904 ● Fluorescent indicator bound calcium, $[BCa]$
- 905 ● Endogenous mobile buffer bound calcium, $[ECa]$
- 906 ● Endogenous immobile buffer bound calcium, $[ImCa]$
- 907 ● Excited buffered calcium, $[BCa^*]$

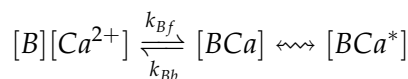
The term ‘buffering’ refers to free calcium ions coming into contact with buffer molecules and binding together. Diagrammatically:



908 where $[X]$ represents any buffer molecule, and k_{X_f} and k_{X_b} represent the binding and un-
909 binding (dissociation) rates in units of per molar concentration per second ($M^{-1} s^{-1}$) and per
910 second (s^{-1}) respectively. The speed of this chemical reaction is determined by the binding
911 and unbinding rates.

912 There are a number different endogenous buffers in any neuron. Which buffers are
913 present, and the buffers’ concentrations vary from cell to cell. In order to capture the ef-
914 fects of mobile and immobile endogenous buffers without introducing several parameters,
915 they were modelled as two buffers. One representing mobile buffers and the other represent-
916 ing immobile buffers. Each with their own binding and unbinding rates.

The fluorescent calcium indicator behaves similarly to the other calcium buffers. The calcium is buffered by the indicator in the same way. But an indicator bound calcium molecule can become excited by absorbing the energy from a photon. An excited indicator bound calcium molecule can then release a photon to go back to its ‘relaxed’ state.



917 The released photons are captured by a photon collector. This gives us the fluorescence trace.
918 Ignoring the baseline level of free calcium in a neuron, the system of equations we used
919 to model all of these interactions is as follows:

$$\begin{aligned} \frac{d[Ca^{2+}]}{dt} = & k_{Bb}[BCa] + k_{Eb}[ECa] + k_{Imb}[ImCa] \\ & - k_{Bf}[B][Ca^{2+}] - k_{Ef}[E][Ca^{2+}] - k_{Imf}[Im][Ca^{2+}] \\ & + \beta([Ca_0^{2+}] - [Ca^{2+}]) \end{aligned} \quad (2.1)$$

$$\frac{d[BCa]}{dt} = k_{Bf}[B][Ca^{2+}] - k_{Bb}[BCa] + r[BCa^*] - e[BCa] \quad (2.2)$$

$$\frac{d[ECa]}{dt} = k_{Ef}[E][Ca^{2+}] - k_{Eb}[ECa] \quad (2.3)$$

$$\frac{d[ImCa]}{dt} = k_{Imf}[Im][Ca^{2+}] - k_{Imb}[ImCa] \quad (2.4)$$

$$\frac{d[BCa^*]}{dt} = \eta[BCa] - r[BCa^*] \quad (2.5)$$

where $[Ca_0^{2+}]$ is the baseline calcium concentration within the cell soma, β is a rate defining how quickly free calcium enters or leaves the cell in the absence of an action potential, η is the excitation rate for indicator bound calcium, r is the photon release rate for the excited indicator bound calcium, and f and b are used to indicate the forward and backward rates for chemical reactions respectively. The excitation rate defines the proportion of indicator bound calcium that becomes excited at each time step. The photon release rate defines the proportion of excited indicator bound calcium that releases a photon and returns to its relaxed state at each time step. An action potential is modelled as a discontinuous increase in the free calcium concentration to an appropriate value (Maravall et al., 2000).

Note that each of the three pairs of binding and unbinding terms in the first equation has a corresponding pair in one of the subsequent three equations. Binding removes a free calcium molecule and adds a bound calcium molecule, and unbinding does the opposite.

When using this model to simulate a fluorescence trace, the system of equations above are first solved over a period of 25s without action potentials. This lets each of the five tracked chemical concentrations reach their steady state. Then we use the given spike train and the parameters to model the fluorescence trace.

Note that since the model has no spatial component, the mobile and immobile buffers only differ in their binding and unbinding rates.

Photon release & capture

We used a simple model for the photon release. The number of photons released at each time step was controlled by the number of excited indicator bound calcium molecules in the cell and a parameter called the ‘release rate’. The release rate is an optimised free parameter of the model.

As for the photon capture, in two-photon excitation microscopy the photons scattered by the fluorescent indicator get scattered in all directions. Therefore the number of photons detected is stochastic. This made the process for capturing photons the natural source of noise in the system. The number of photons captured, and therefore the intensity of the

947 fluorescence, is modelled using a binomial distribution. The number of photons released was
948 used as the number of trials. The probability of success, or ‘capture rate’ was a free parameter
949 of the model that we optimised.

950 **2.4.2 Parameter optimisation**

951 The free parameters of the model are as follows:

952 **Calcium rate, β** Controls how quickly the concentration of free calcium will be driven to
953 the baseline concentration.

954 **Capture rate, p** The average proportion of photons captured by the photon detector.

955 **Excitation rate, η** The number of indicator bound calcium molecules that become excited
956 by photon bombardment at each time step.

957 **Release rate, r** The number of excited indicator bound calcium molecules that release a
958 photon at each time step.

959 To optimise the free parameters given a fluorescence trace, we applied the following proce-
960 dure:

- 961 1. The frequency power spectrum of the trace was measured.
- 962 2. The power spectrum was smoothed using a boxcar smoother (aka. sliding average, box
963 smoother).
- 964 3. The log of the smoothed power spectrum was measured.
- 965 4. Use the model to create a modelled fluorescence trace.
- 966 5. Apply steps 1, 2, and 3 to the modelled fluorescence trace.
- 967 6. Calculate the root mean squared difference between the log power of the actual fluo-
968 rescence trace, and the log power of the modelled fluorescence trace.
- 969 7. Calculate the root mean squared difference between the actual fluorescence trace and
970 the modelled fluorescence trace.
- 971 8. Use an optimisation algorithm to reapply this process, attempting to minimize the sum
972 of the two root mean squared differences at each iteration.

973 Using the root mean squared difference of the log power spectra as part of the objective
974 function forces the model to match the noise frequency of the actual fluorescence. Using
975 the root mean squared difference of the traces themselves forces the model to match the
976 amplitude of the fluorescence trace more accurately.

977 In order to minimise the objective function, a suite of meta-heuristic optimisation (aka.
978 black-box optimisation) algorithms were implemented on each of the traces in the dataset.
979 These methods were chosen because they don't require a gradient for the objective function
980 (gradient-free) and they are particularly useful for minimising stochastic objective functions
981 like the one we used here. The free parameters were optimised for each individual fluores-
982 cence trace. The most successful method for each trace was recorded. The method that was
983 most often successful was probabilistic descent, and the second most successful method was
984 generating set search. Both of these methods are examples of pattern search. These two
985 methods were the best optimisers on about 75% of the traces in the dataset.

986 Although this optimisation procedure minimises the value of the optimisation function,
987 the value never reaches zero for a number of reasons. Firstly, the fluorescence traces carry low
988 frequency fluctuations that cannot be captured by the model. Secondly, the model assumes
989 that the process of calcium binding to the fluorescent indicator is linear in time (see equation
990 1), but there are more complicated dynamics involved here. Fluorescent calcium indicators
991 are often built upon the calcium binding protein called 'calmodulin'. This protein has four
992 calcium binding sites. These sites are locally split into two pairs. Each pair has a different
993 affinity for calcium, and the affinity of the binding sites is affected by the occupancy of
994 the other binding sites (Kilhoffer et al., 1992). So the calcium to calcium indicator binding
995 process is non-linear, but the model does not take this into account.

996 **Fixed parameters**

997 As well as the optimised parameters mentioned in section 2.4.2, the model also has thirteen
998 fixed parameters. Please see table 2.1 for details of these parameters and their values. In
999 an application of the model, these parameters can be changed in order to model any given
1000 fluorescent calcium indicator.

1001 **2.4.3 Julia**

1002 The programming language used to write and execute the model was 'Julia'. Julia is a dy-
1003 namic programming language designed for technical computing. Julia was designed specif-
1004 ically to provide a convenient high-level dynamic language similar to MATLAB, or Python,

Parameter	Description	Value	Source
baseline	The baseline concentration of free calcium within the cell soma	$4.5 \times 10^{-8} M$	(Maravall et al., 2000)
cell radius	The radius of the soma (assumed to be spherical)	$10^{-5} M$	(Fiala and Harris, 1999)
endogenous	The concentration of endogenous mobile buffer within the cell soma	$10^{-4} M$	(Faas et al., 2011)
frequency	The frequency at which the spike trains are sampled.	100Hz	
immobile	The concentration of endogenous immobile buffer within the cell soma	$7.87 \times 10^{-5} M$	(Bartol et al., 2015)
indicator	The concentration of fluorescent indicator within the cell soma	$10^{-4} M$	(Maravall et al., 2000)
k_{Bb}	The unbinding rate of the fluorescent calcium indicator	$160 s^{-1}$	(Bartol et al., 2015)
k_{Bf}	The binding rate of the fluorescent calcium indicator	$7.77 \times 10^8 s^{-1} M^{-1}$	(Bartol et al., 2015)
k_{Eb}	The unbinding rate of the endogenous mobile buffer	$10^4 s^{-1}$	(Bartol et al., 2015)
k_{ef}	The binding rate of the endogenous mobile buffer	$10^8 s^{-1} M^{-1}$	(Bartol et al., 2015)
k_{Imb}	The unbinding rate of the endogenous immobile buffer	$524 s^{-1}$	(Bartol et al., 2015)
k_{Imf}	The binding rate of the endogenous immobile buffer	$2.47 \times 10^8 s^{-1} M^{-1}$	(Bartol et al., 2015)
peak	The increase in free calcium concentration within the cell induced by an action potential	$2.9 \times 10^{-7} M$	(Maravall et al., 2000)

TABLE 2.1: **Fixed parameters** A table of the parameters fixed before optimising the model. The values of these parameters could be changed to model different fluorescent calcium indicators.

1005 with improved performance. Julia’s type system and Julia’s direct interfaces with C and
1006 Fortran allow this aim to be achieved (Bezanson et al., 2012). The Julia version of the
1007 ‘Sundials’ package for ODE solving was used to solve the system of equations above. The
1008 BlackBoxOptim.jl package for Julia was used to perform the optimisation.

1009 **2.4.4 Spike inference**

1010 We used spike inference algorithms to compare the quality of spike inference using the mod-
1011 elled traces to the quality of spike inference using the observed traces. We also used the
1012 spike inference algorithms to assess the effect of parameter perturbation on the spike infer-
1013 ence. Three algorithms were used:

1014 **Constrained non-negative deconvolution algorithm (aka Pnevmatikakis algorithm)** This
1015 algorithm uses a constrained version of non-negative Weiner deconvolution to infer a
1016 calcium signal and a ‘spiking activity signal’ from the fluorescence trace (Vogelstein
1017 et al., 2010; Pnevmatikakis et al., 2016). The spiking activity signal is a non-negative
1018 vector of real numbers reflecting the cell’s activity rather than an actual spike train. We
1019 inferred a spike train by choosing an optimised threshold for the spiking activity sig-
1020 nal. Whenever the spiking activity signal exceeded that threshold, an action potential
1021 was inferred. The threshold was optimised by minimising the difference between the
1022 number of spikes observed and the number of spikes predicted.

1023 **ML-Spike algorithm** This algorithm uses a generalised version of the Viterbi algorithm to
1024 return the spike train that maximises the likelihood of producing the given fluorescence
1025 trace. The Viterbi algorithm is an algorithm for estimating the most likely sequence
1026 of hidden states resulting in a sequence of observed states in a discrete-time finite-
1027 state Markov process (Forney, 1973). In this case, each hidden state is defined by the
1028 presence or absence of an action potential, and each observed state is the value of the
1029 fluorescence trace at each time step. This algorithm assumes that the concentration of
1030 calcium within the cell will decay to a drifting baseline, rather than a fixed baseline
1031 (Deneux et al., 2016).

1032 **Online Active Set method to Infer Spikes (OASIS)** This algorithm is once again based on
1033 an auto-regressive model of the fluorescence trace, but can be generalised to any or-
1034 der. The algorithm itself is a generalisation of the pool adjacent violators algorithm
1035 (PAVA) that is used in isotonic regression. The OASIS algorithm works through the

1036 fluorescence trace from beginning to end, this combined with the speed of the algo-
1037 rithm means that it could be used for real-time online spike inference (Friedrich and
1038 Paninski, 2016). Given a fluorescence trace, the algorithm will return the most likely
1039 spike train and an inferred denoised fluorescence signal.

1040 In order to quantify the quality of spike inference for a given algorithm, we ran that algorithm
1041 on all of the fluorescence traces in dataset number eight of the spike finder datasets. Then we
1042 measured some binary classification measures on the results. These measures included

- 1043 ● Accuracy
- 1044 ● True positive rate (aka recall, sensitivity, hit rate)
- 1045 ● True negative rate (aka specificity)
- 1046 ● Precision
- 1047 ● Negative predicted value
- 1048 ● False negative rate (aka miss rate)
- 1049 ● False positive rate (aka fall-out)
- 1050 ● False discovery rate
- 1051 ● False omission rate

1052 In making these measurements, we allowed a tolerance of two subsequent time bins for spike
1053 prediction. For example, the spike train data is a vector of 0s and 1s, with one element for
1054 each time bin. A ‘0’ denotes inactivity, a ‘1’ denotes the presence of at least one action
1055 potential. The inferred spike trains produced by the spike inference algorithms take the same
1056 form. In our analysis, if a spike appeared in the inferred spike train up to two time frames
1057 after a spike in the observed spike train, that spike was considered correctly inferred i.e. a true
1058 positive. However, once a spike in the inferred spike train was matched to a spike from the
1059 observed spike train, the inferred spike could not be matched to another observed spike. To
1060 illustrate, if two spikes were inferred in the two time bins following an isolated observed
1061 spike, the first inferred spike was considered correctly inferred, but the second inferred spike
1062 was considered incorrectly inferred, i.e. a false positive.

1063 The most useful measure was the true positive rate. This is because the spiking is sparse
1064 and this measurement is sensitive to the number of spikes observed and inferred, but is not
1065 affected by the true negative or false negative rates. After optimising the parameters for each

1066 fluorescence trace we measured the spike inference quality for the observed fluorescence
1067 traces, and compared this to the spike inference quality for the modelled traces.

1068 When measuring the spike inference quality for higher frequency spike train (1 – 10Hz),
1069 we used the accuracy as our binary classification measure. At these frequencies the variance
1070 of the fluorescence trace was much higher than for sparser spiking regimes, therefore we
1071 wanted to take into account the number of false negatives inferred by the algorithm.

1072 **Comparing spike inference quality**

1073 In order to compare spike inference quality we had to use methods for comparing samples.
1074 When comparing the true positive rate distributions arising from two different datasets, or
1075 two different algorithms on the same dataset, we compared the distributions using a paired
1076 t-test.

1077 **2.4.5 Perturbation analysis**

1078 In order to measure the sensitivity of spike inference to changes in a given model parameter,
1079 we perturbed the parameter and compared the quality of spike inference with the perturbed
1080 parameters to the quality of spike inference with the experimental or optimised parameters.
1081 In order to maximise the possibility of observing a difference due to the perturbation, we
1082 perturbed the chosen parameter by a relatively large amount. For example, the experimen-
1083 tal value for the molar concentration of the fluorescent indicator within the cell was 10^{-4}M
1084 (Maravall et al., 2000). The perturbed values used for this parameter were 10^{-2}M , 10^{-3}M ,
1085 10^{-5}M , and 10^{-6}M . The quality of the inference was compared by measuring the true posi-
1086 tive rate for each perturbed value and using a t-test to compare the distributions of the results.

1087 This analysis was performed firstly without any optimisation of the free parameters for
1088 use with the perturbed parameters. Then the analysis was performed after the optimised
1089 parameters for each perturbed value were calculated.

1090 **2.4.6 Signal-to-noise ratio**

1091 To assess the effect of perturbation on the modelled traces, we measured and compared the
1092 signal to noise ratio (SNR) on each of the modelled traces. We calculated the SNR as the
1093 peak change in fluorescence divided by the standard deviation of the baseline fluctuation of
1094 the fluorescence trace (Tada et al., 2014). We measured these values by running the model
1095 on a spike train consisting a long period of inactivity followed by one action potential. We
1096 ran the model on this spike train one hundred times. We then measured the mean change

1097 in fluorescence and standard deviation of baseline activity across the one hundred modelled
1098 fluorescence traces, and calculated the SNR.

1099 **2.4.7 Data sources**

1100 All of the data used in this project was sourced from the ‘Spike Finder’ project (spikefinder.codeneuro.org).
1101 The data consisted of a collection of datasets with simultaneously measured fluorescence
1102 traces and action potentials (Berens et al., 2018).

1103 **Chapter 3**

1104 **Functional networks expand across**
1105 **anatomical boundaries as correlation**
1106 **time-scale increases**

1107 *Abstract*

1108 Decades of research has established that correlated spiking plays a crucial role in represent-
1109 ing sensory information. One drawback associated with the recent improvement in recording
1110 technology and consequent large datasets is the difficulty in analysing higher order correla-
1111 tions in large neuronal ensembles. One benefit of these datasets that has not yet been explored
1112 is the opportunity to compare correlations within anatomical regions to correlations across
1113 anatomical regions. In this work, we measured correlations between neurons residing in
1114 nine different brains regions in three awake and behaving mice. Using the these correlation
1115 measurements, we created weighted undirected graph networks and applied network science
1116 methods to detect functional communities in our neural ensembles. We compared these func-
1117 tional communities to their anatomical distribution. We repeated the analysis, using different
1118 timescales for our correlation measurements, and found that functional communities were
1119 more likely to be dominated by neurons from a single brain region at shorter timescales
1120 (< 100ms).

1121 3.1 Introduction

1122 Decades of research has established that correlations play a crucial role in representing sen-
1123 sory information. For example, the onset of visual attention has been shown to have a greater
1124 affect on the correlations in the macaque V4 region than on the firing rates in that region
1125 (Cohen and Maunsell, 2009). Recent findings show that spontaneous behaviours explain cor-
1126 relations in parts of the brain not associated with motor control (Stringer et al., 2019), that
1127 satiety state appears to have a brain wide representation (Allen et al., 2019), and that subject
1128 exploratory and non-exploratory states are represented in the amygdala (Gründemann et al.,
1129 2019). So, behavioural states are likely represented across many regions of the brain, not just
1130 motor related areas. In order to understand the brain, we must understand the interactions
1131 between neurons and regions.

1132 Because of limitations in recording technology almost all research has explored corre-
1133 lations between neurons within a given brain region, or within only two regions at most
1134 (Wierzynski et al., 2009; Patterson et al., 2014; Girard, Hupé, and Bullier, 2001). Rela-
1135 tively little is known about correlations between neurons in many different brain regions.
1136 However, the recent development of ‘Neuropixels’ probes (Jun et al., 2017) has allowed
1137 extracellular voltage measurements to be collected from multiple brain regions simultane-
1138 ously routinely, and in much larger numbers than traditional methods. In this project we
1139 used a publicly-available Neuropixels dataset to analyse correlations between different brain
1140 regions (Stringer et al., 2019).

1141 A drawback associated with the improvement in recording technology is an increase in
1142 the difficulty in analysing these data. For example, analysing the i th order interactions of
1143 N neurons generally requires estimation of N^i parameters. A number that becomes astro-
1144 nomical for large N . New methods are required for analysing these new large datasets. We
1145 attempted to address this requirement in this piece of research by applying a cutting-edge
1146 network science community detection method to neural data.

1147 Another unexplored area of research is the changes in cell interactions at different timescales.
1148 Studies have shown different timescales for fluctuations in spiking activity (Murray et al.,
1149 2014), and different time scales for event representation (Baldassano et al., 2017) across dif-
1150 ferent brain regions. Still most studies focus on quantifying interactions at a given timescale.
1151 But neurons may interact differently, or may interact with different neurons at different
1152 timescales. Here we explore correlated communities of neurons at different timescales.

1153 In this work, we measured correlations between binned spike counts from neurons from

1154 nine different regions of the mouse brain. These measurements induced a weighted undi-
1155 rected graph or network where each neuron is represented by a node, and the strength of
1156 the connection between these nodes/neurons is the strength of the correlation between their
1157 spike counts. We then applied newly invented network methods (Humphries et al., 2019)
1158 to this network to find any community structure, and place the neurons in these correlation
1159 based communities. Finally, we compared these functional communities to the anatomical
1160 membership of the neurons.

1161 To investigate the functional communities and their relationship with anatomy at different
1162 time scales, we repeated these analyses using different length bin widths when binning spike
1163 times.

1164 To find and analyse functional networks while controlling for the subject's behaviour, we
1165 conditioned the binned spike counts on data from a video of the subject's face, and repeated
1166 our analysis for spike count correlations (or noise correlations) and signal correlations.

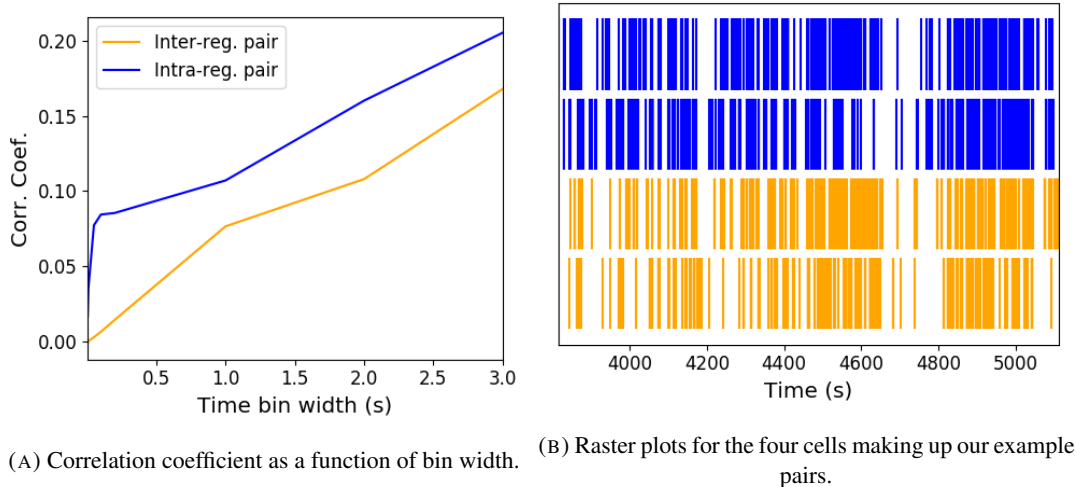
1167 3.2 Results

1168 Note that in the following text, we refer to the correlation coefficient between two sequences
1169 of spike counts from two different cells as the *total correlation*. We refer to the correlation
1170 between spike counts in response to a certain stimulus as the *spike count correlation* aka
1171 *noise correlation*, and we refer to the correlation between mean or expected responses to
1172 different stimuli as the *signal correlation* (Cohen and Kohn, 2011).

1173 The nine different brain regions from which we had data were the caudate putamen (CP),
1174 frontal motor cortex (FrMoCtx), hippocampus (HPF), lateral septum (LS), midbrain (MB),
1175 primary visual cortex (V1), superior colliculus (SC), somatomotor cortex (SomMoCtx), and
1176 thalamus (TH).

1177 3.2.1 Average correlation size increases with increasing time bin width

1178 First we inspected the affect of time bin width on total correlations. We know that using short
1179 time bins results in artificially small correlation measurements (Cohen and Kohn, 2011), so
1180 we expected to see an increase in correlation amplitude with increasing time bin width. That
1181 is exactly what we observed. Taking 50 cells at random, we calculated the total correla-
1182 tion between every possible pair of these cells, using different time bin widths ranging from
1183 0.005s to 3s. We found that the longer the time bin width, the greater the correlations (see
1184 figure 3.2a).



(A) Correlation coefficient as a function of bin width. (B) Raster plots for the four cells making up our example pairs.

FIGURE 3.1: (A) An example of the correlation coefficients between two different pairs of cells, one where both cells are in the same brain region (intra-regional pair), and one where both cells are in different brain regions (inter-regional pair). The correlation coefficients have been measured using different time bin widths, ranging from 5ms to 3s. Note the increasing amplitude of the correlations with increasing bin width. (B) A raster plot showing the spike times of each pair of cells.

1185 We also separated the positively correlated pairs from the negatively correlated pairs
 1186 using the mean correlation of each pair across all bin widths (see section 3.5.2). We found
 1187 that the positively correlated pairs become more positively correlated with increasing time bin
 1188 width, and the negatively correlated pairs become more negatively correlated with increasing
 1189 time bin width (see figures 3.2b and 3.2c).

1190 In figure 3.1a we plot correlations from two example pairs, one pair from within a region,
 1191 and one pair between regions. It can be seen that the correlation coefficient increases with
 1192 bin width. The correlations can be observed by eye in the raster plot for these cells in figure
 1193 3.1b.

1194 When taking the mean across all pairs, the positively correlated pairs dominate in terms
 1195 of both number of pairs, and amplitude of correlations. Therefore the mean across all pairs
 1196 is positive.

1197 These results were observed in each of the three mouse subjects from which we had data.

1198 3.2.2 Goodness-of-fit for Poisson and Gaussian distributions across increasing 1199 time bin widths

1200 We wanted to investigate if the width of the time bin used to bin spike times into spike counts
 1201 had an effect on the distribution of spike counts. We used the χ^2 statistic as a goodness-of-fit
 1202 measure for Poisson and Gaussian (normal) distributions to the spike count of 100 randomly

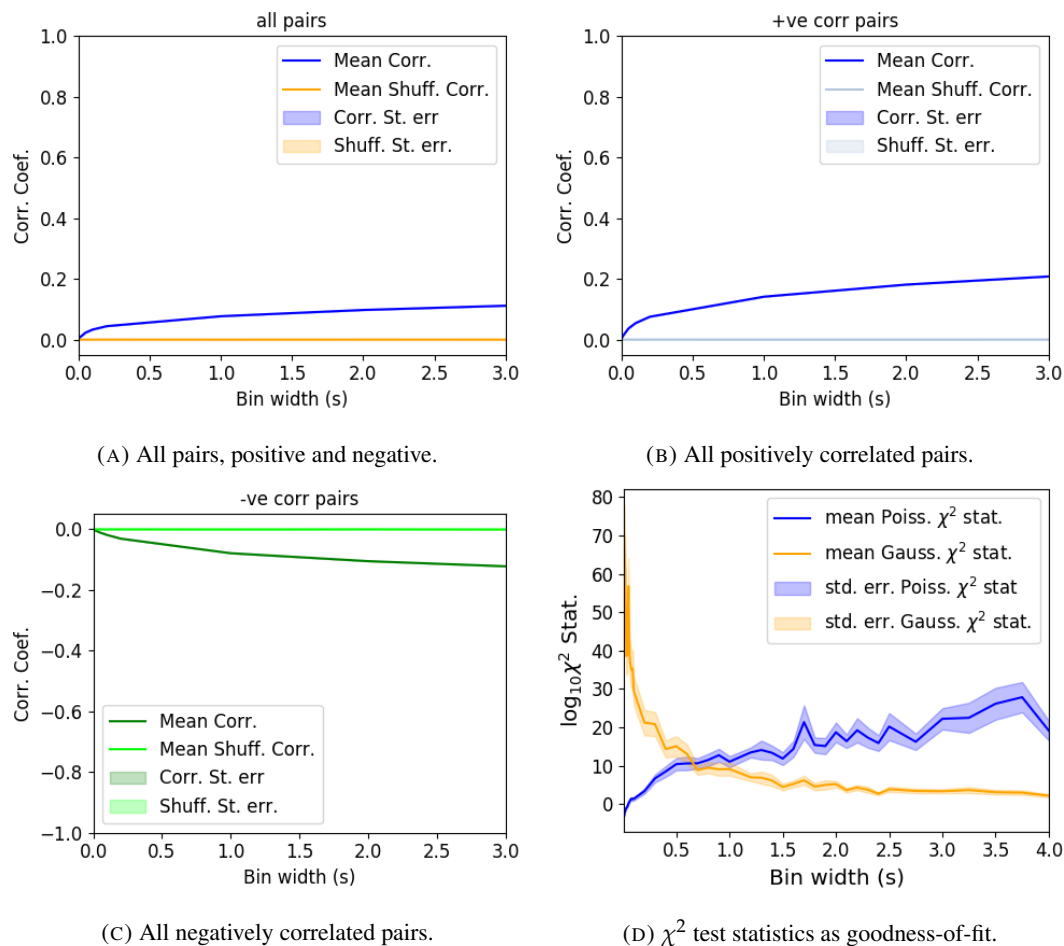


FIGURE 3.2: Mean correlation coefficients measured from pairs of 50 randomly chosen neurons. (A) All possible pairs, (B) positively correlated pairs, and (C) negatively correlated pairs. (D) Mean and standard error of χ^2 test statistics for Poisson and Gaussian distributions fitted to neuron spike counts.

1203 chosen neurons for a number of bin widths ranging from 0.01s to 4s. For the χ^2 statistic, the
1204 higher the value, the worse the fit.

1205 We expected a Poisson distribution to be a better fit for shorter time bin widths because
1206 spike counts must be non-negative, therefore any distribution of spike counts with mass dis-
1207 tributed at or close to 0 will be skewed. The distribution of spike counts is more likely to be
1208 distributed close to 0 when the time bin widths used to bin spike times into spike counts are
1209 small relative to the amount of time it takes for a neuron to fire an action potential ($\sim 1\text{ms}$ in
1210 the case of non-burst firing neurons).

1211 We expected a Gaussian distribution to be a better fit for longer time bin widths, because
1212 a Poisson distribution with a large rate is well approximated by a Gaussian distribution with
1213 mean and variance equal to the Poisson rate. Therefore, a Gaussian distribution would ap-
1214 proximate the mean of a collection of large spike counts, and have more flexibility than a
1215 Poisson distribution to fit the variance.

1216 We found that that a Poisson distribution is the best fit for shorter time bins less than 0.7s
1217 in length. Then a Gaussian distribution is a better fit for time bins greater than 0.7s in length
1218 (see figure 3.2d).

1219 **3.2.3 Differences between and inter- and intra- regional correlations decrease
1220 with increasing bin width**

1221 We investigated the differences in distribution between inter-regional correlations, i.e. corre-
1222 lations between neurons in different brain regions, and intra-regional correlations, i.e. corre-
1223 lations between neurons in the same brain region.

1224 Firstly, we investigated these quantities for all possible pairs of ~ 500 neurons taken
1225 from across all the 9 brain regions from which we had data. We distributed these neurons as
1226 evenly as possible across all of the regions, so that cells from one region would not dominate
1227 our data. We observed that the mean intra-regional correlations were always higher than the
1228 mean inter-regional correlations for every value of time bin width used. We also observed
1229 that as the time bin width increased these mean correlations increased and the difference
1230 between the mean inter-regional and intra-regional correlations grew (see figure 3.3 (Left)).

1231 Stringer et al. (2019) had a similar finding using the same data. They used only one value
1232 for the time bin width, 1.2s. Using this time bin width to bin spike times and measure total
1233 correlations, they found that the mean ‘within-region’ correlations were always greater than
1234 the ‘out-of-region’ correlations (Stringer et al., 2019). The figure from their paper showing
1235 this result can be seen in figure 3.3 (Right).

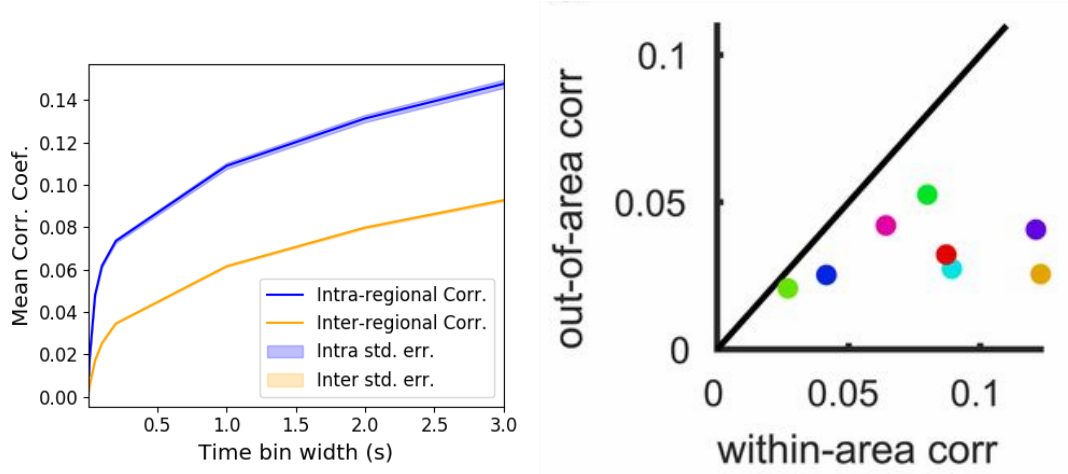


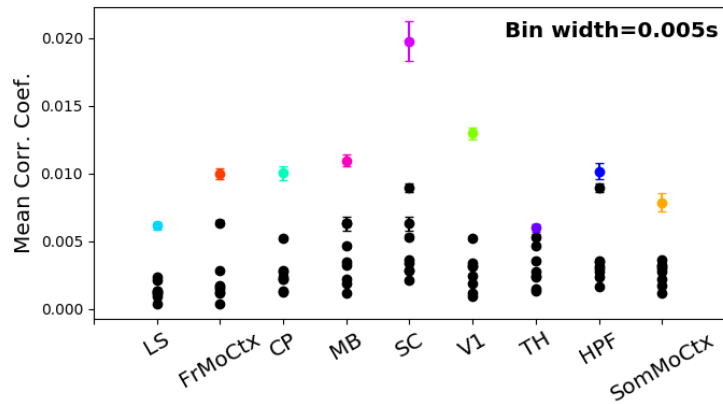
FIGURE 3.3: (Left) The mean intra-region and inter-region correlations using all possible pairs of ~ 500 neurons, spread across 9 different brain regions. (Right) Courtesy of Stringer et al. (2019), mean inter-regional (out-of-area) correlation coefficients vs mean intra-regional (within-area) correlation coefficients for a bin width of 1.2s. Note that the intra-regional coefficients are higher in each case.

1236 Examples of the correlations of one intra-regional pair and one inter-regional pair can be
 1237 seen in figure 3.1.

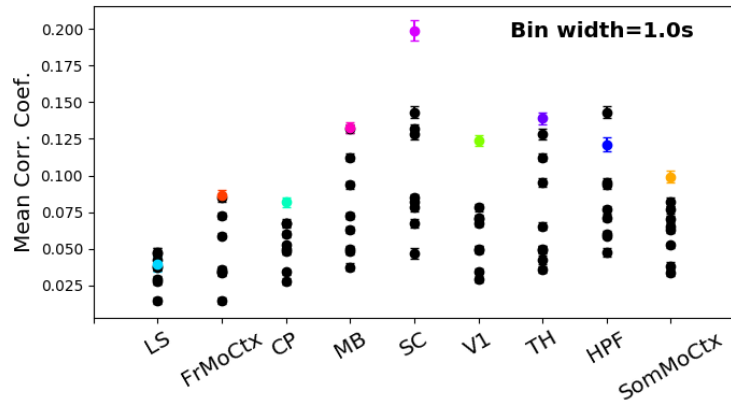
1238 Secondly, we separated those pairs into intra-regional and inter-regional groups. We
 1239 noted that the mean intra-regional correlations (coloured dots in figures 3.4a and 3.4b) for
 1240 a given region tended to be higher than the mean inter-regional correlations (black dots in
 1241 figures 3.4a and 3.4b) involving cells from that region. However, in contrast with our previous
 1242 result, we noted that the difference between the mean intra-regional correlations and most
 1243 highly correlated inter-regional correlations reduced as we increased the time bin width (see
 1244 figures 3.4a and 3.4b). This shows that the mean correlations shown in figure 3.3 are not
 1245 distributed evenly across all region pair combinations.

1246 Finally, to see these regional mean correlations in a bit more detail, to examine the indi-
 1247 vidual pair combinations in particular, we displayed these data in a matrix of mean corre-
 1248 lations (see figure 3.5), showing the mean intra-regional correlations on the main diagonal, and
 1249 the mean inter-regional correlations off diagonal. Comparing a version of this figure created
 1250 using a short time bin width of 5ms (figure 3.5a) and a version using a longer time bin width
 1251 of 1s (figure 3.5b) we observed that the mean intra-regional correlations are always relatively
 1252 high in comparison to the mean inter-regional correlations, but the mean correlations in some
 1253 inter-regional pairs are relatively much higher when using the longer time bin width.

1254 This could indicate information being processed quickly at a local or within-region level,
 1255 and the local representations of this information spreading between regions at longer timescales.



(A) Mean inter-regional and intra-regional correlations using a time bin width of 5ms.



(B) Mean inter-regional and intra-regional correlations using a time bin width of 1s.

FIGURE 3.4: The mean intra-regional correlations (coloured dots) and mean inter-regional correlations (black dots) for a given region, indicated on the x-axis, for different time bin widths. Each black dot represents the mean inter-regional correlations between the region indicated on the x-axis and one other region. (A) shows these measurements when we used a time bin width of 5ms. (B) shows these measurements when we used a time bin width of 1s. Note that the difference between the mean inter-regional correlations and mean intra-regional correlations is smaller for 1s bins.

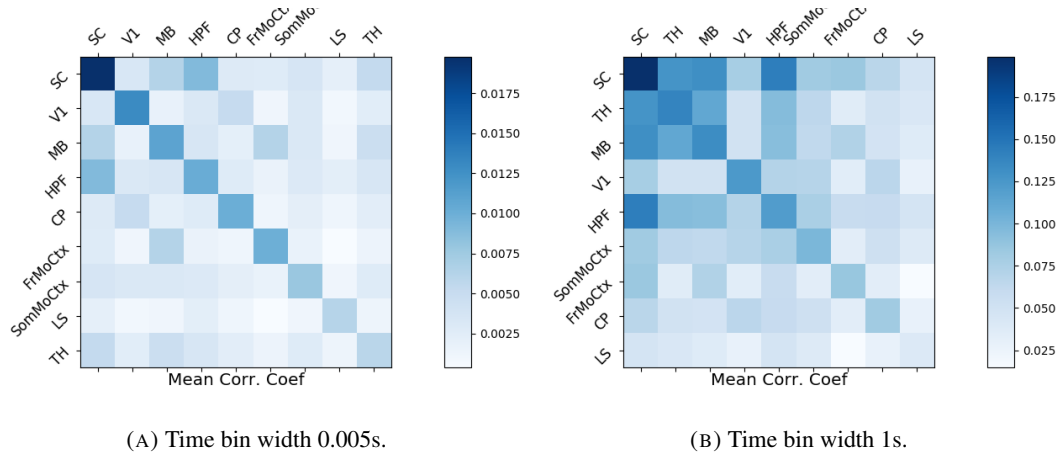


FIGURE 3.5: Mean inter-regional (main diagonal) and intra-regional (off diagonal) correlation coefficients. (A) Shows these measurements when spike times were binned using 5ms time bins. (B) Shows the same, using 1s time bins. Note that the matrices are ordered according to the main diagonal values, therefore the ordering is different in each subfigure.

1256 These results were consistent across the three mouse subjects. But, the relative magni-
 1257 tudes of the mean intra-regional and inter-regional correlations were not consistent. For ex-
 1258 ample, the region with the highest mean intra-regional correlations when using 1s bin widths
 1259 for subject one is the superior colliculus (SC), but for subject two it is the midbrain (MB).

1260 **3.2.4 Connected and divided structure in correlation based networks reduces
 1261 in dimension with increasing bin width**

1262 We used the correlation measurements to create weighted undirected graphs/networks where
 1263 each node represents a neuron, and the weight of each edge is the pairwise correlation be-
 1264 tween those neurons represented by the nodes at either end of that edge. We aimed to find
 1265 communities of neurons within these networks, and compare the structure of these commu-
 1266 nities to the anatomical division of those neurons. The first step of this process involved
 1267 applying the ‘spectral rejection’ technique developed by Humphries et al (2019) (Humphries
 1268 et al., 2019). This technique compares our data network to a chosen null network model, and
 1269 finds any additional structure in the data network beyond that which is captured in the null
 1270 network model (if there is any such structure).

1271 By comparing the eigenspectrum of the data network to the eigenspectrum of many sam-
 1272 ples from the null network model, this technique allows us to estimate the dimensionality of
 1273 the additional structure in the data network, and gives us a basis for that vector space. It also
 1274 divides the additional structure into connected structure, and k -partite (or divided) structure.
 1275 For example, if our algorithm found two dimensions of additional connected structure, and

1276 one dimension of additional divided structure. We might expect to find three communities,
1277 that is groups more strongly connected within group than without, and we might expect to
1278 find bi-partite structure, that is two sets that are more strongly connected between groups
1279 than within groups.

1280 The technique also finds which nodes contribute to this additional structure, and divides
1281 our data network into signal and noise networks. The details of spectral rejection and node
1282 rejection can be found in sections 3.5.5 and 3.5.5 respectively, and a full overview can be
1283 found in (Humphries et al., 2019).

1284 We chose the sparse weighted configuration model (see section 3.5.5) as our null network
1285 model. This model matches the sparsity and the total weight of the original network but
1286 distributes the weight at random across the sparse network.

1287 We applied the spectral rejection method to our networks based on total correlations using
1288 different values for the time bin width. We observed that for smaller time bin widths, our data
1289 networks had both k -partite structure, and community structure. As the width of the time bin
1290 increased, we found that the k -partite structure disappeared from our data networks, and the
1291 dimension of the community structure reduced in two of the three mice from which we had
1292 data (see figure 3.6).

1293 3.2.5 Detecting communities in correlation based networks

1294 We applied the community detection procedure described in section 3.5.5 to our signal net-
1295 works for our various time bin widths. We detected a greater number of smaller communities
1296 at shorter time bin widths, and a smaller number of larger communities for longer time bin
1297 widths (see figure 3.7). This was expected after the results found in section 3.2.4. We found
1298 more dimensions of additional structure at shorter time bin widths, therefore we found more
1299 communities at shorter time bin widths.

1300 We also noticed that at short time bin widths the communities detected tended to be
1301 dominated by cells from one region. Whereas communities existing in networks created
1302 using wider time bin widths tended to contain cells from many different brain regions. More
1303 on this in the next section.

1304 3.2.6 Functional communities resemble anatomical division at short timescales

1305 In order to quantify the similarity of the communities detected to the anatomical division of
1306 the cells. We treated both the anatomical division and the communities as clusterings of these
1307 cells. We then used measures for quantifying the difference or similarity between clusterings

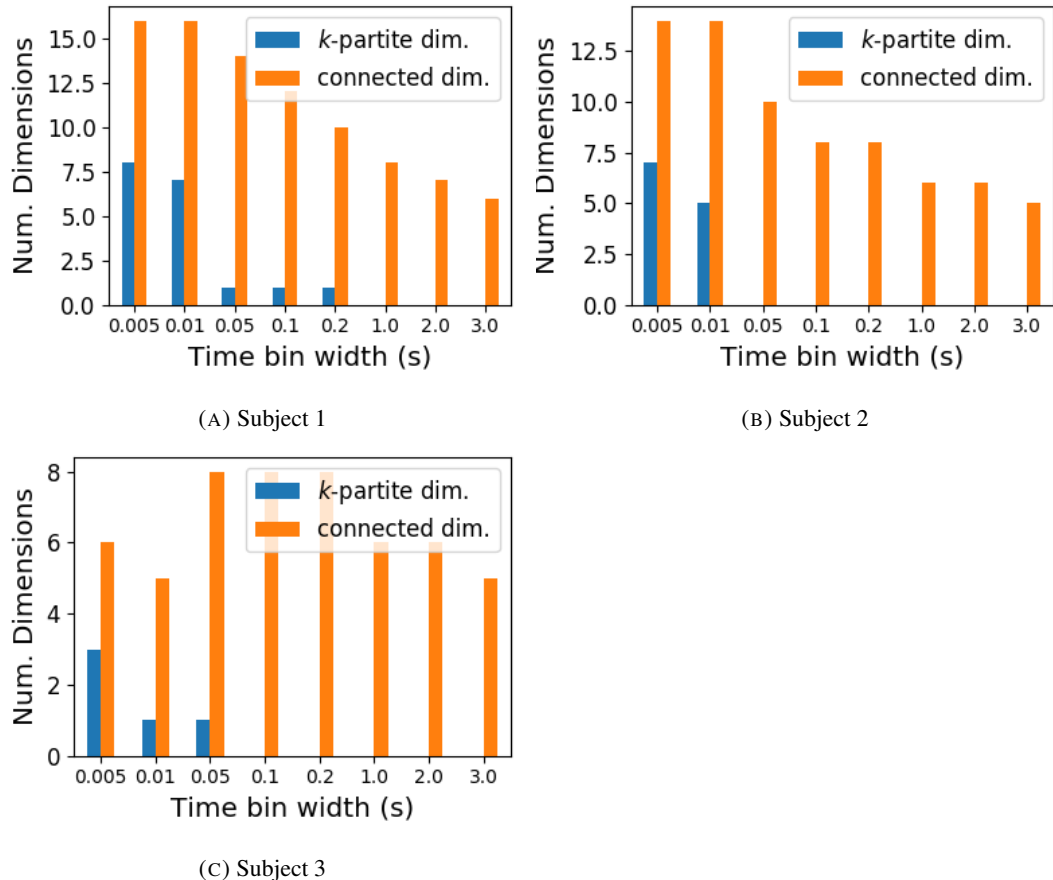


FIGURE 3.6: The number of dimensions in the *k*-partite and connected structure in the correlation based networks beyond the structure captured by a sparse weighted configuration null network model (see section 3.5.5), shown for different time bin widths. Note that the *k*-partite structure disappears for time bin width greater than 200ms for all three subjects. The dimension of the connected structure reduces with increasing bin width for 2 of the 3 subjects (top row).

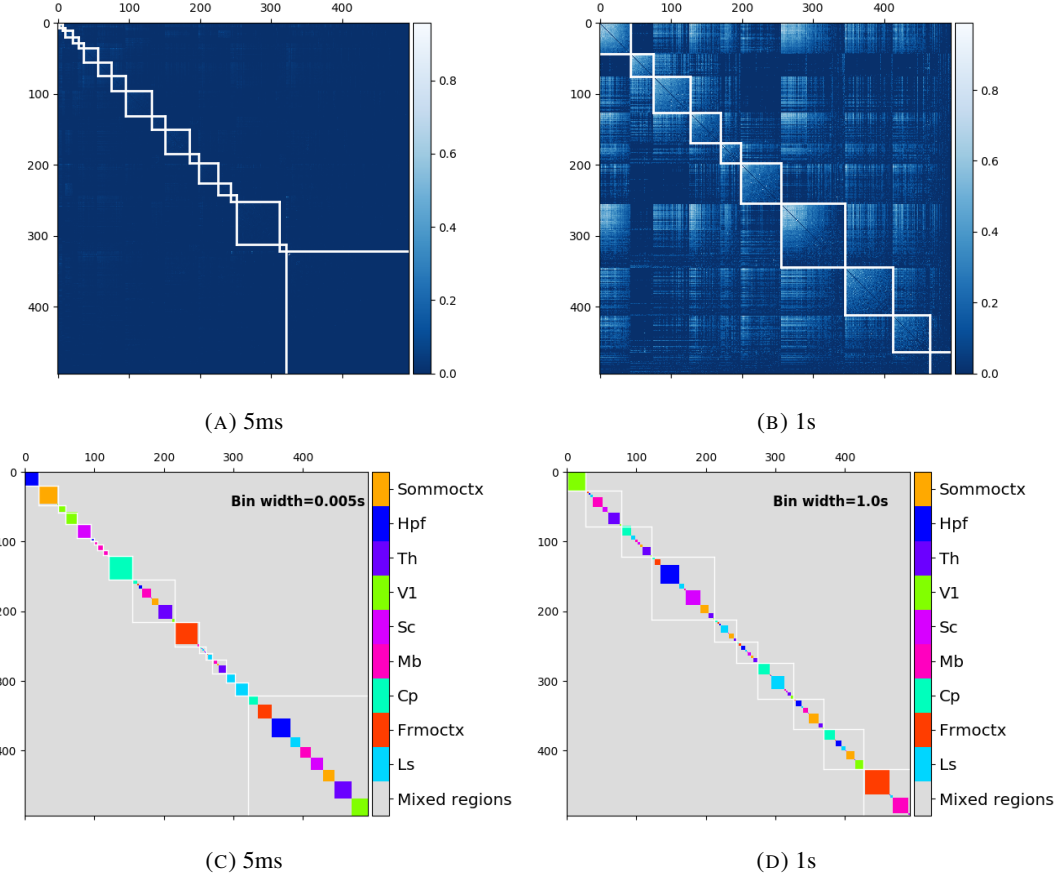


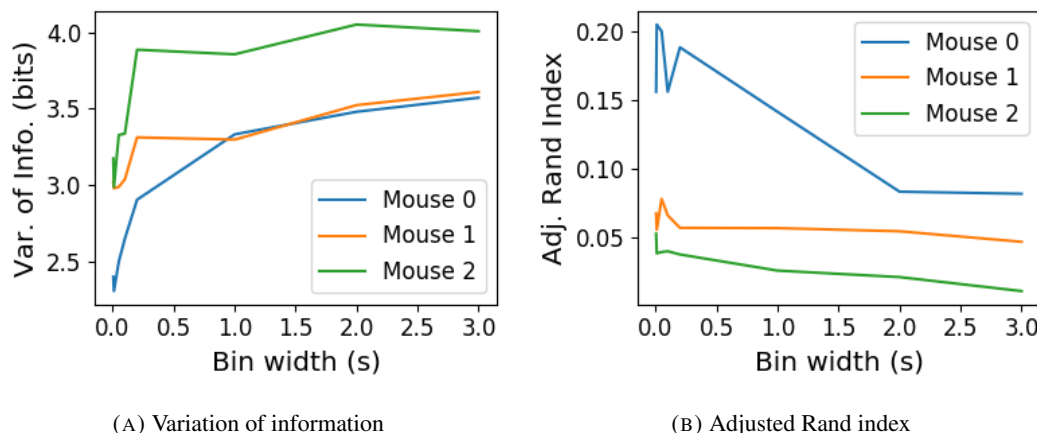
FIGURE 3.7: (A-B) Correlation matrices with detected communities indicated by white lines. Each off main diagonal entry in the matrix represents a pair of neurons. Those entries within a white square indicate that both of those neurons are in the same community as detected by our community detection procedure. Matrices shown are for 5ms and 1s time bin widths respectively. Main diagonal entries were set to 0. (C-D) Matrices showing the anatomical distribution of pairs along with their community membership. Entries where both cells are in the same region are given a colour indicated by the colour bar. Entries where cells are in different regions are given the grey colour also indicated by the colour bar.

to quantify the difference or similarity between the detected communities and the anatomical division. Details of these measures can be found in section 3.5.6 or in (Vinh, Epps, and Bailey, 2010).

We used two different types of measures for clustering comparison; information based measures (see section 3.5.6) and pair counting based measures (see section 3.5.6). We include one example of each in figure 3.8.

The variation of information is the information based measure included in figure 3.8a. This measure forms a metric on the space of clusterings. The larger the value for the variation of information, the more different the clusterings.

The adjusted Rand index is the pair counting based measure included in figure 3.8b. In contrast with the variation of information, the adjusted Rand index is a normalised similarity measure. The adjusted Rand index takes value 1 when the clusterings are identical, and takes value 0 when the clusterings are no more similar than chance.



(A) Variation of information

(B) Adjusted Rand index

FIGURE 3.8: (A) The variation of information is a measure of distance between clusterings. The distance between the anatomical ‘clustering’ and community detection ‘clustering’ increases with increasing time bin width. (B) The adjusted Rand index is a normalised similarity measure between clusterings. The anatomical and community detection clusterings become less similar as the time bin width increases.

Both measures indicated that the detected communities and the anatomical division of the cells were more similar when we used shorter time bins widths (see figure 3.8). This indicates that correlated behaviour in neuronal ensembles is more restricted to individual brain regions at short timescales (< 250ms), and the correlated activity spreads out across brain regions over longer time scales.

1326 **3.2.7 Conditional correlations & signal correlations**

1327 In light of the excellent research of Stringer et al (2019) showing that spontaneous behaviours
 1328 can drive activity in neuronal ensembles across the visual cortex and midbrain (Stringer et
 1329 al., 2019), we decided to control for the mouse’s behaviour when performing our analyses.
 1330 It is possible that our community detection process may be detecting communities across
 1331 multiple brain regions at longer time scales due to aggregating neuronal activity driven by
 1332 several spontaneous behaviours occurring during the time interval covered by a given time
 1333 bin. A time bin of 1s, for example, could contain a spike count where those spikes were driven
 1334 by different spontaneous behaviours. We aimed to investigate this possibility by applying our
 1335 community detection analysis to conditional correlation measures.

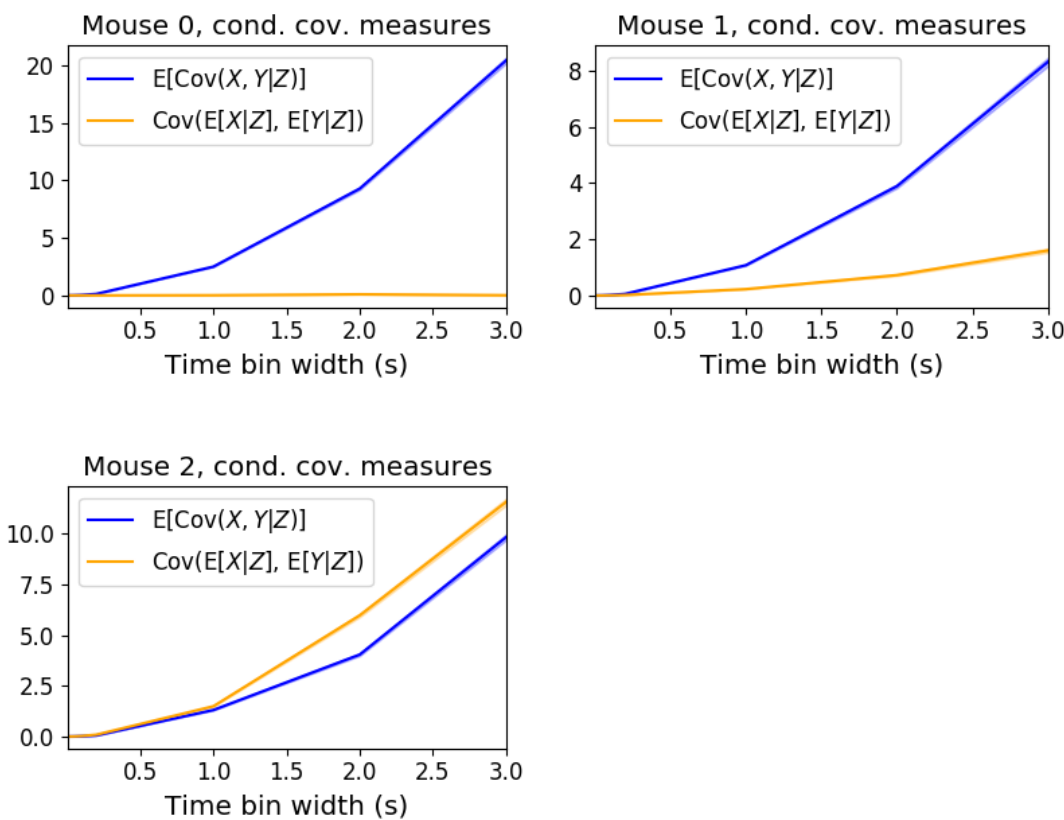


FIGURE 3.9: Comparing the components of the total covariance across different values for the time bin width. We observed a consistent increase in $E[\text{cov}(X, Y|Z)]$ as the time bin width increased. But we saw different trends for $\text{cov}(E[X|Z], E[Y|Z])$ for each mouse.

1336 We used the top 500 principal components of a video of the mouse’s face as a measure of
 1337 the mouse’s behaviour (see section 3.4.2). We modelled the spike counts as a linear combi-
 1338 nation of the principal components using linear regression with ElasticNet regularisation (see

section 3.5.3). Using this model, we quantified the expected spike count given the mouse’s behaviour $E[X|Z_1, \dots, Z_{500}]$.

We used these expected values to measure $\text{cov}(E[X|Z], E[Y|Z])$, and we used that value, the covariance $\text{cov}(X, Y)$, and the *law of total covariance* (see section 3.5.3) to measure $E[\text{cov}(X, Y|Z)]$. Here X and Y represent spike counts from individual cells, and Z is shorthand for the 500 principal components mentioned above. The two components of the covariance, $\text{cov}(E[X|Z], E[Y|Z])$ and $E[\text{cov}(X, Y|Z)]$, represent a ‘signal covariance’ and expected value of a ‘spike count covariance’ respectively, analogous to the signal correlation and spike count correlation (Cohen and Kohn, 2011).

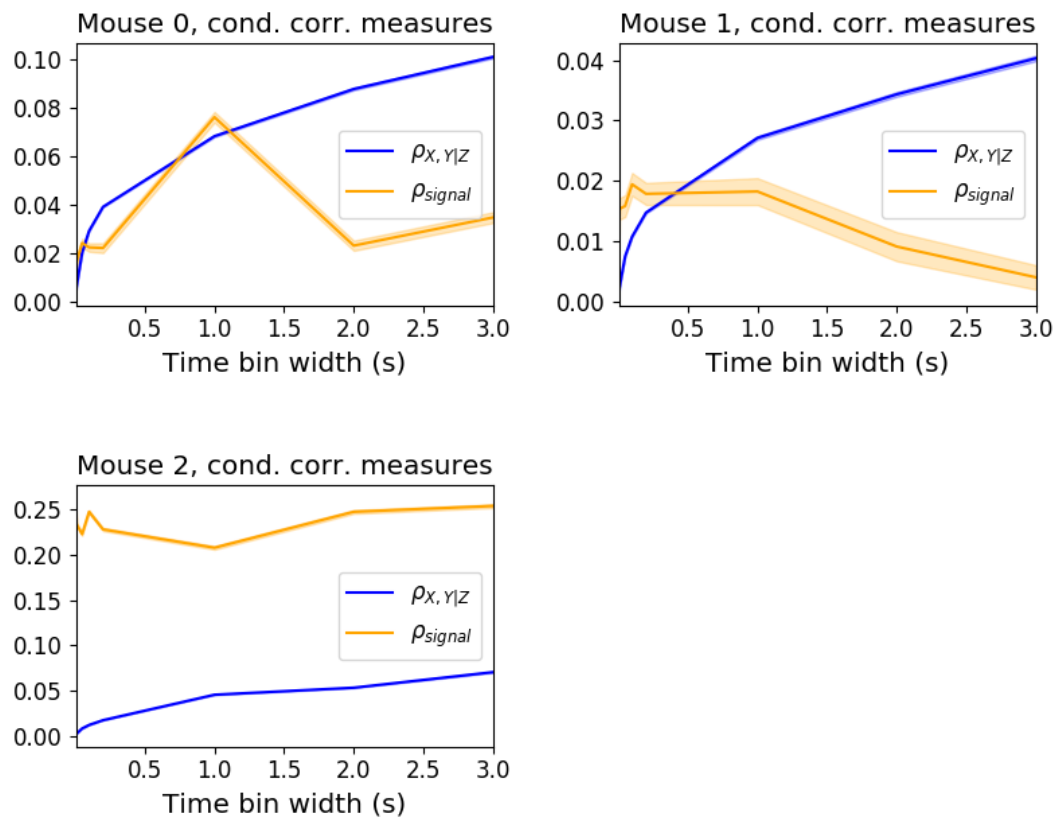


FIGURE 3.10: Comparing the components of the total covariance across different values for the time bin width. We saw a consistent increase in $\rho_{X,Y|Z}$ as the time bin width increased in all three subjects. But we saw different trends in ρ_{signal} for each of the subjects.

We examined the means of these components for different values of the time bin width (see figure 3.9). We observed a consistent increase in $E[\text{cov}(X, Y|Z)]$ as the time bin width increased. But we saw different trends for $\text{cov}(E[X|Z], E[Y|Z])$ for each mouse.

Using $\text{cov}(E[X|Z], E[Y|Z])$ we measured the signal correlation, ρ_{signal} , and using $E[\text{cov}(X, Y|Z)]$ we measured the event conditional correlation, $\rho_{X,Y|Z}$ (see section 3.5.3 for more details).

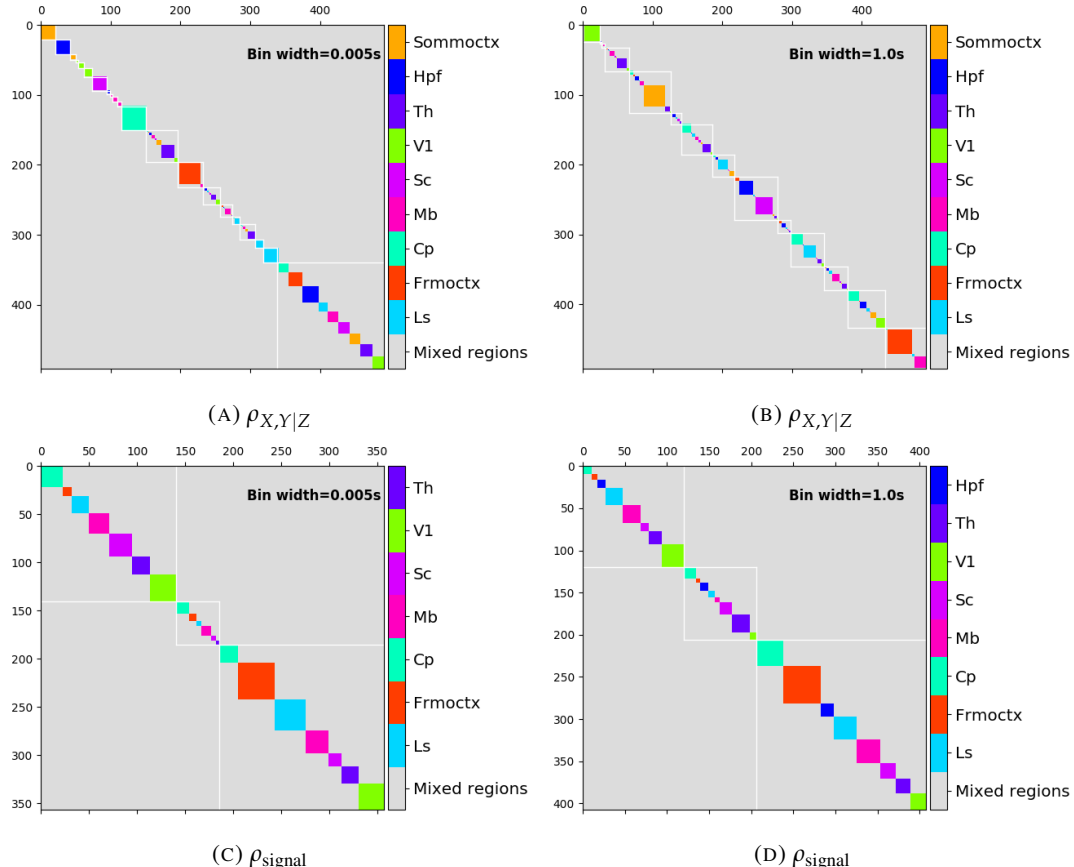


FIGURE 3.11: Matrices showing the regional membership of pairs by colour, and the communities in which those pairs lie. (A-B) Detected communities and regional membership matrix for network based on rectified spike count correlation $\rho_{X,Y|Z}$, using time bin widths of 0.005s and 1s respectively. (C-D) Detected communities and regional membership matrix for network based on rectified signal correlation ρ_{signal} , using time bin widths of 0.005s and 1s respectively.

1353 We saw a consistent increase in $\rho_{X,Y|Z}$ as the time bin width increased, this corresponds to
 1354 the result for $E[\text{cov}(X, Y|Z)]$. We observed different trends for ρ_{signal} for each mouse, this
 1355 corresponds to the result for $\text{cov}(E[X|Z], E[Y|Z])$.

1356 We applied our network noise rejection and community detection process to networks
 1357 based on the spike count correlations $\rho_{X,Y|Z}$ and the signal correlations ρ_{signal} . We noted that
 1358 the community detection on $\rho_{X,Y|Z}$ behaved similarly to the community detection on the total
 1359 correlation. We can see this in figures 3.11a and 3.11b. At very short time bin widths, we
 1360 detect more communities, and those communities often contain cells from one brain region
 1361 only. At longer time bin widths, we detect fewer communities, and those communities tend
 1362 to contain cells from multiple brain regions. When we examine the distance between (or
 1363 similarity between) the anatomical division of the cells, and the detected communities we
 1364 notice that the two clusterings are more similar at shorter time bin widths (see figure 3.12).

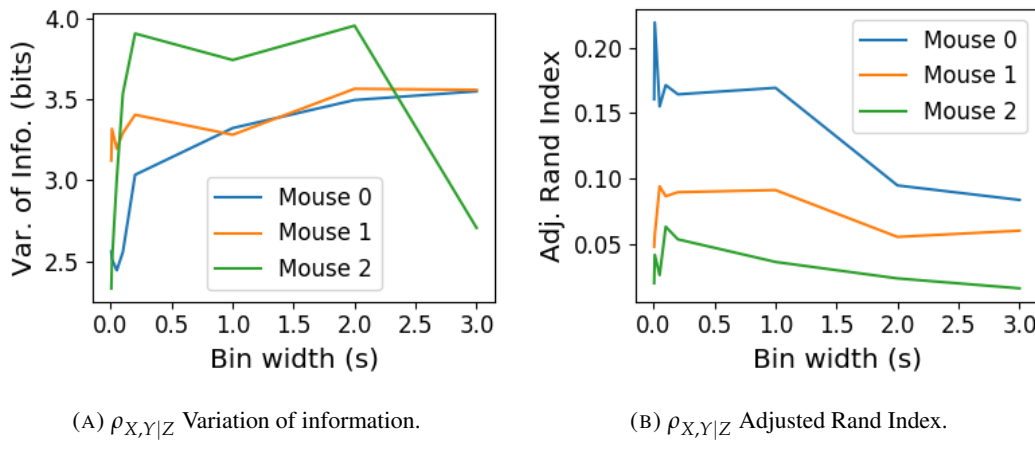
(A) $\rho_{X,Y|Z}$ Variation of information.(B) $\rho_{X,Y|Z}$ Adjusted Rand Index.

FIGURE 3.12: Distance and similarity measures between the anatomical division of the neurons, and the communities detected in the network based on the spike count correlations $\rho_{X,Y|Z}$. (A) The variation of information is a ‘distance’ measure between clusterings. The distance between the anatomical ‘clustering’ and the community clustering increases as the time bin width increases. (B) The adjusted Rand index is a similarity measure between clusterings. The detected communities become less similar to the anatomical division of the cells as the time bin width increases.

1365 When we applied the network noise rejection and community detection process to the
 1366 networks based on the signal correlations ρ_{signal} we found the number of communities we
 1367 detected reduced with increasing time bin width. But the number of communities detected
 1368 was less than that for the total correlations or the spike count correlations. The commu-
 1369 nities detected always tended to contain cells from multiple regions at both short and long
 1370 timescales (see figures 3.11c and 3.11d). The communities detected bore very little relation
 1371 to the anatomical division of the cells. The adjusted Rand index between the community

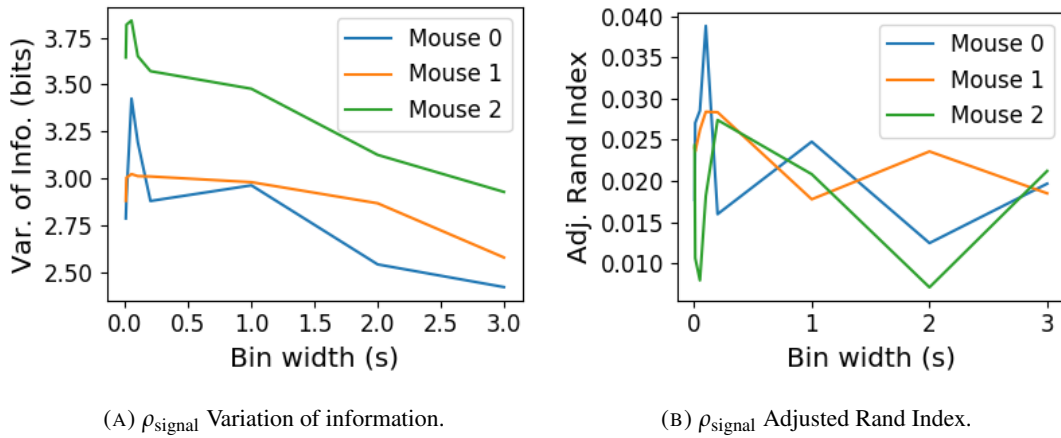


FIGURE 3.13: Distance and similarity measures between the anatomical division of the neurons, and the communities detected in the network based on the signal correlations ρ_{signal} . (A) The variation of information is a ‘distance’ measure between clusterings. The distance between the anatomical ‘clustering’ and the community clustering increases as the time bin width increases. (B) The adjusted Rand index is a similarity measure between clusterings. The detected communities become less similar to the anatomical division of the time bin width increases.

1372 clustering and the anatomical ‘clustering’ is close to zero for every time bin width (see figure
 1373 3.13b). This indicates that the similarity between the clusterings is close to chance. We did
 1374 observe a slight downward trend in the variation of information with increasing bin width
 1375 (see figure 3.13a), but this is more likely due to a decrease in the number of communities
 1376 detected rather than any relationship with anatomy.

1377 We also observed that the network noise rejection process rejected some of the cells
 1378 when applied to the network based on the signal correlations. This means that those cells
 1379 did not contribute to the additional structure of the network beyond that captured by the
 1380 sparse weighted configuration model. This is why the matrices in figures 3.11c and 3.11d are
 1381 smaller than their analogues in figures 3.11a and 3.11b.

1382 3.2.8 Absolute correlations and negative rectified correlations

1383 At the moment, the network noise rejection protocol can only be applied to weighted undi-
 1384 rected graphs with non-negative weights. This meant that we had to rectify our correlated
 1385 networks before applying the network noise rejection and community detection process. We
 1386 wanted to investigate what would happen if instead of rectifying the correlations, we used the
 1387 absolute value, or reversed the signs of the correlations and then rectified.

1388 When we used the absolute value of the correlations, we found very similar results to

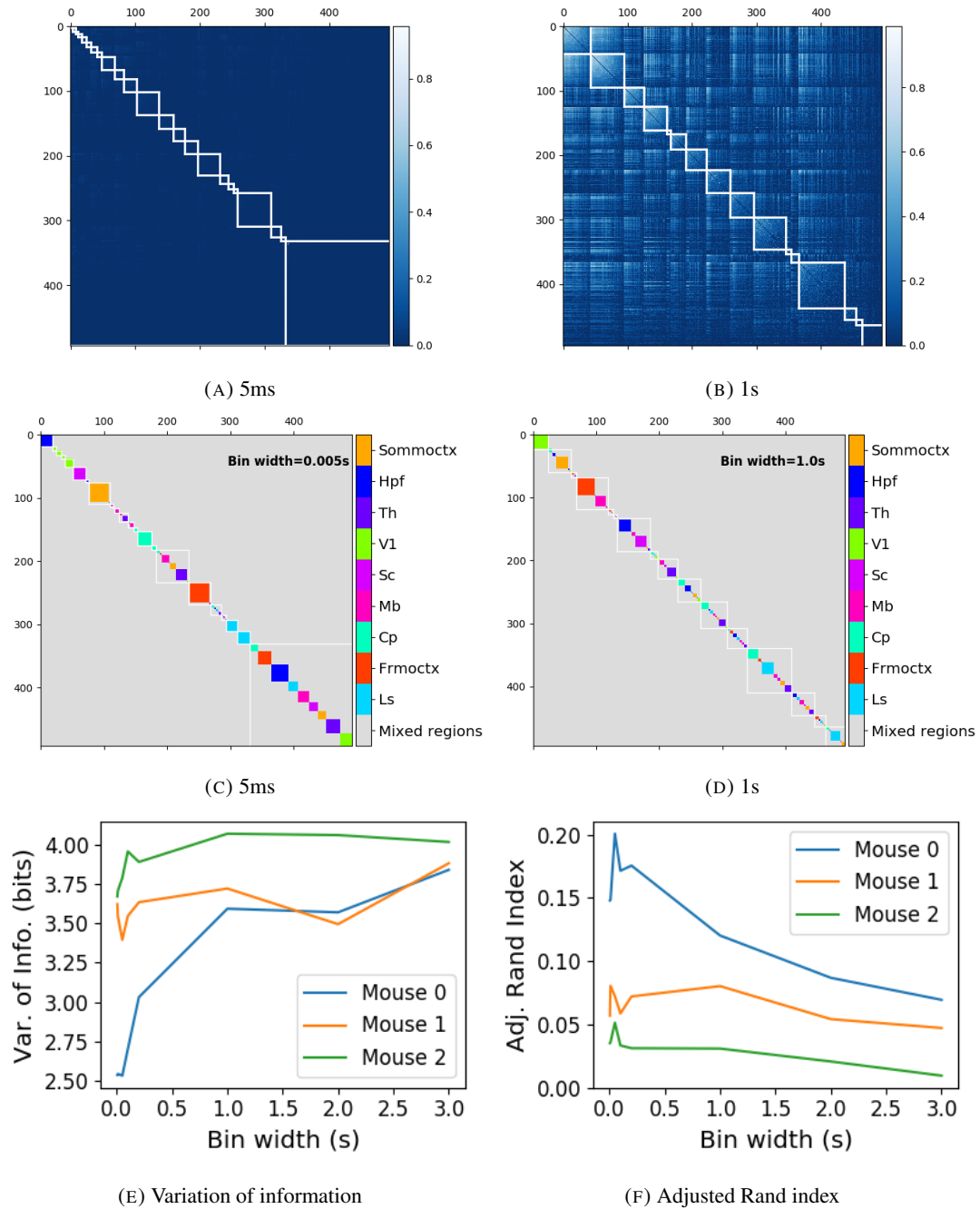


FIGURE 3.14: (A-B) Absolute correlation matrices with detected communities indicated by white lines. These communities are based on the absolute value of the total correlation between each pair of cells. Those entries within a white square indicate that both of those neurons are in the same community. Matrices shown are for 5ms and 1s time bin widths respectively. Main diagonal entries were set to 0. (C-D) Matrices showing the anatomical distribution of pairs along with their community membership. Regional membership is indicated by the colour bar. (E) Variation of information between the anatomical division of the cells, and the detected communities. (F) Adjusted Rand index between the anatomical division, and the detected communities.

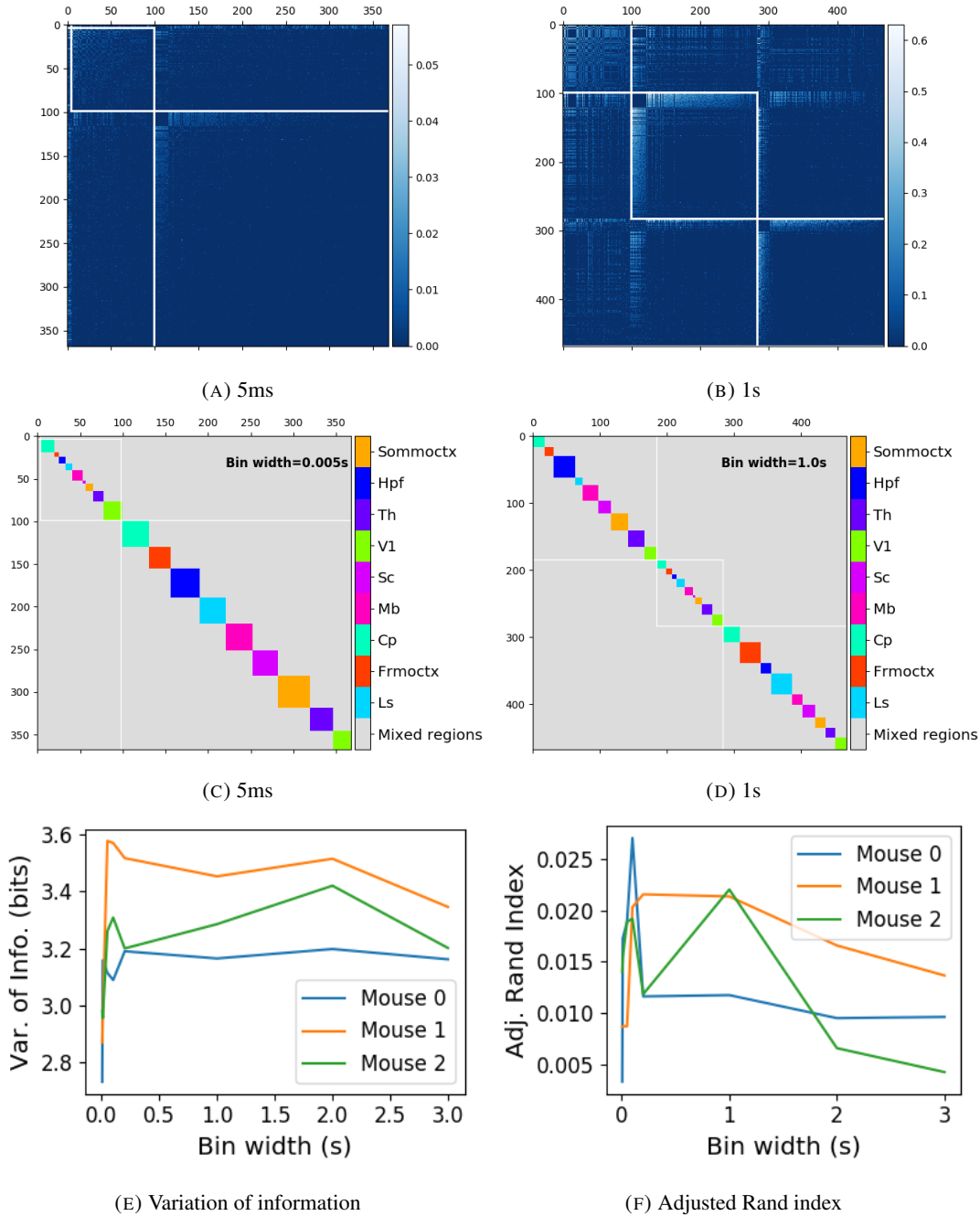


FIGURE 3.15: (A-B) Sign reversed rectified correlation matrices with detected communities indicated by white lines. Those entries within a white square indicate that both of those neurons are in the same community. Matrices shown are for 5ms and 1s time bin widths respectively. Main diagonal entries were set to 0. (C-D) Matrices showing the anatomical distribution of pairs along with their community membership. Regional membership is indicated by the colour bar. (E) Variation of information between the anatomical division of the cells, and the detected communities. (F) Adjusted Rand index between the anatomical division, and the detected communities.

1389 those shown above for the rectified total correlations and the rectified spike count corre-
1390 lations. We detected more communities using shorter bin widths, and these communities
1391 were more similar to the brain’s anatomy than those communities detected using a longer bin
1392 width (see figure 3.14). The only exception being that we detected more communities. This
1393 could indicate that we detected both positively and negatively correlated communities, but
1394 we haven’t done any further investigation so we cannot say for sure.

1395 When we used the sign reversed rectified correlated networks, we tended to find fewer
1396 communities. Each community contained cells from many different anatomical regions, at
1397 both long and short bin widths (see figures 3.15a, 3.15b, 3.15c, 3.15d). The communities
1398 bore little relation to the anatomical distribution of the cells, this can be seen in figure 3.15f,
1399 the values close to zero indicate that the similarity between the two clusterings are around
1400 chance level. This indicates that there was not much structure in the negatively correlated
1401 networks beyond that captured by the sparse weighted configuration model.

1402 3.3 Discussion

1403 It is well established that the brain uses correlated behaviour in neuronal ensembles to repre-
1404 sent the information taken in through sensation (Cohen and Maunsell, 2009; Litwin-Kumar,
1405 Chacron, and Doiron, 2012; deCharms and Merzenich, 1996). However, most studies that
1406 examine the nature of these correlations in-vivo, study an ensemble of cells from only one
1407 or two brain regions (Cohen and Kohn, 2011; Wierzynski et al., 2009; Patterson et al., 2014;
1408 Girard, Hupé, and Bullier, 2001). Furthermore, recent results have shown that behaviour can
1409 drive correlated activity in multiple brain regions, including those not normally associated
1410 with motor control (Stringer et al., 2019; Gründemann et al., 2019; Allen et al., 2019). In this
1411 study, we utilised one of the newly recorded large datasets containing electrophysiological
1412 recordings from multiple brain regions simultaneously. We investigated correlated behaviour
1413 in these different brain regions and we investigated correlated behaviour between neurons in
1414 different regions, during spontaneous behaviour.

1415 A number of studies have found that the timescale of correlated behaviour induced by a
1416 stimulus can be modulated by the stimulus structure and behavioural context. For example,
1417 the spike train correlations between cells in weakly electric fish are modulated by the spa-
1418 tial extent of the stimulus (Litwin-Kumar, Chacron, and Doiron, 2012), and neurons in the
1419 marmoset primary auditory cortex modulate their spike timing (and therefore correlation) in
1420 response to stimulus features without modulating their firing rate (deCharms and Merzenich,

1421 1996). Furthermore, the width of the time bins over which spike counts are measured has
1422 been shown to have an effect on the magnitude of those correlations (Cohen and Kohn, 2011).
1423 Despite this, very little research has been done comparing correlation measures from the same
1424 dataset at different timescales. We investigated this by varying the time bin width used to bin
1425 spike times into spike counts from as short as 5ms up to 3s.

1426 In order to further investigate the effect of these correlations at different timescales, we
1427 regarded our neuronal ensemble as a weighted undirected graph, where each neuron is rep-
1428 resented by a node, and the weight on each edge is the correlation between the neurons
1429 connected by that edge. We then applied a novel clustering method from network science
1430 (Humphries et al., 2019) to identify communities in these networks. Communities in a net-
1431 work graph refer to sets of nodes that are more strongly connected to each other than the
1432 nodes outside of their set. Another way to put this is to say that the nodes in a community
1433 are more strongly connected than *expected*. What connection strength might be expected is
1434 defined by a null network model. We chose a null network model that matched the sparsity
1435 and total strength of our correlation based data networks. So, if two cells were in the same
1436 community, those cells were more correlated than would be expected given the correlation
1437 strength of their ensemble.

1438 These networks, and the community detection process, were completely agnostic of the
1439 anatomical division of the cells in our ensemble. When we compared the detected commu-
1440 nities with the anatomical division of the cells using distance and similarity measures for
1441 clusterings, we found that the detected communities were more similar to the anatomical
1442 division at shorter timescales. That is, when we used a wider time bin to count spikes, and
1443 computed pairwise correlations with these spike counts, the correlated communities tended to
1444 exist within anatomical regions at shorter timescales, and tended to span anatomical regions
1445 at longer timescales. This could reflect localised functional correlations at short time scales
1446 rippling outwards across brain regions at longer timescales. The brain may be processing
1447 some information quickly locally, and carrying out further, perhaps more detailed, represen-
1448 tation over a longer timescale across many regions using the representations that were just
1449 built locally.

1450 These changes in communities across timescales could also be driven by the anatomy
1451 of the individual cells. For example, it may simply take longer to transmit action potentials
1452 over longer distances, hence correlated activity over longer timescales will exist between
1453 anatomical regions, rather than within. However, the switch to almost exclusively multi-
1454 regional functional networks at 1s bin widths, rather than a mixture of multi-region, and

1455 single-region suggests that the inter-regional correlations either overpower, or inhibit the
1456 local correlations. So there may be more at play than just timescales.

1457 We acknowledged that the region spanning correlated communities that we detected at
1458 longer time scales could exist due to collating activity driven by distinct spontaneous activi-
1459 ties. In order to account for this, we modelled the spike counts as a linear function of the
1460 top 500 principal components of a video of the mouse's face filmed simultaneously with the
1461 electrophysiological readings. We applied our network noise rejection and community de-
1462 tected process to the weighted undirected networks formed by the spike count correlations
1463 (or noise correlations) and the signal correlations that we calculated using our model. For the
1464 spike count correlation networks, we found much the same results as for the total correlations
1465 as described above. For the signal correlations, the communities detected in these networks
1466 bore little relation to the anatomical division of the cells. Recent findings have shown that
1467 behavioural data accounts for correlations in many brain regions that would otherwise be
1468 dismissed as noise (Stringer et al., 2019), our finding to shows that these correlations are still
1469 governed by the timescale division between local communication and across-region commu-
1470 nication.

1471 There is a lot of room for further investigation based on this research. For a start, the
1472 data that we used here were collected from nine different regions in the mouse brain, but
1473 none of these regions were part of the somatosensory cortex. Given that a mouse experiences
1474 so much of its environment through its sense of smell, some data from this region would be
1475 interesting to investigate. On the same theme, the mice in the experiment from which the
1476 data were collected were headfixed and placed on a rotating ball, but were otherwise behav-
1477 ing spontaneously. Had these mice been exposed to a visual, aural, or olfactory stimulus,
1478 we could have examined the responses of the cells in the brain regions corresponding to vi-
1479 sion, hearing, and olfaction, and compared these responses to the responses from the other
1480 brain regions. Furthermore, we could have investigated the interaction between the sets of
1481 responses.

1482 Another space for further investigation is the community detection. The algorithm that we
1483 used here never detects overlapping communities. But functional communities could indeed
1484 have overlaps. Clustering methods that detect overlapping clusters do exist (Baadel, Thabtah,
1485 and Lu, 2016). Applying one of those algorithms could yield some interesting results. Also,
1486 the community detection algorithm that we used here cannot process graphs with negative
1487 weights, this forced us to separate positive and negative correlations before applying our
1488 network noise rejection and community detections process, or use the absolute value of our

1489 correlations. A community detection algorithm that can work on weighted undirected graphs
1490 with negative weights could yield some interesting results here.

1491 3.4 Data

1492 The data that we used in this project were collected by Nick Steinmetz and his lab members
1493 (Stringer et al., 2019).

1494 3.4.1 Brain regions

1495 Neuropixels probes were used to collect extracellular recordings (Jun et al., 2017) from three
1496 different mice. The mice were awake, headfixed, and engaging in spontaneous behaviour.
1497 The mice were of different sexes and different ages. One mouse was ‘wild-type’, the others
1498 were mutants. Details as follows:

- 1499 1. male, wild type, P73.
- 1500 2. female, TetO-GCaMP6s, Camk2a-tTa, P113
- 1501 3. male, Ai32, Pvalb-Cre, P99

1502 Eight probes were used to collect readings from 2296, 2668, and 1462 cells respectively.

1503 Data were collected from nine brain regions in each mouse:

- 1504 • Caudate Putamen (CP)
- 1505 • Frontal Motor Cortex (Frmoctx)
- 1506 • Hippocampal formation (Hpf)
- 1507 • Lateral Septum (Ls)
- 1508 • Midbrain (Mb)
- 1509 • Superior Colliculus (Sc)
- 1510 • Somatomotor cortex (Sommocortex)
- 1511 • Thalamus (Th)
- 1512 • Primary visual cortex (V1)

1513 Readings were continuous and lasted for about 1 hour (Stringer et al., 2019). Locations of
1514 each of the probes can be seen in figure 3.16.

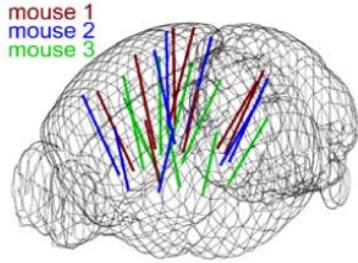


FIGURE 3.16: **Probe Locations:** The locations of the probes in each of the three mouse brains (Stringer et al., 2019).

3.4.2 Video recordings

Video recordings of the mouse's face were taken during the spontaneous behaviour. We had access to the top 500 principle components and top 500 eigenvectors of the processed videos. The frequency of recording was slightly less than 40Hz. Each frame contained 327×561 pixels. These principal components were used as behavioural data. We controlled for these components when taking measurements conditioned on behaviour.

3.5 Methods

3.5.1 Binning data

We transformed the spike timing data into binned spike count data by dividing the experimental period into time bins and counting the spikes fired by each cell within the time period covered by each of those bins. The data were divided into time bins of various widths ranging from 0.01s to 4s.

If the total length of the recording period was not an integer multiple of the time bin width, we cut off the remaining time at the end of the recording period. This period was at most 3.99s. This is far less than the total recording time of around 1 hour. So, this detail would not affect our results.

3.5.2 Correlation coefficients

We calculated Pearson's correlation coefficient for pairs of spike counts from pairs of neurons. For jointly distributed random variables X and Y , Pearson's correlation coefficient is

defined as:

$$\rho_{XY} = \frac{\text{cov}(X, Y)}{\sigma_X \sigma_Y} \quad (3.1)$$

$$= \frac{E[(X - \mu_X)(Y - \mu_Y)]}{\sigma_X \sigma_Y} \quad (3.2)$$

1532 where E denotes the expected value, μ denotes the mean, and σ denotes the standard deviation.
 1533 The correlation coefficient is a normalised measure of the covariance. It can take values
 1534 between 1 (completely correlated) and -1 (completely anti-correlated). Two independent
 1535 variables will have a correlation coefficient of 0. But, having 0 correlation does not imply
 1536 independence.

If we do not know the means and standard deviations required for equation 3.1, but we have samples from X and Y , Pearson's sample correlation coefficient is defined as:

$$r_{XY} = \frac{\sum_{i=1}^n (x_i - \bar{x})(y_i - \bar{y})}{\sqrt{\sum_{i=1}^n (x_i - \bar{x})^2} \sqrt{\sum_{i=1}^n (y_i - \bar{y})^2}} \quad (3.3)$$

1537 where $\{(x_i, y_i)\}$ for $i \in \{1, \dots, n\}$ are the paired samples from X and Y , and $\bar{x} = \frac{1}{n} \sum_{i=1}^n x_i$,
 1538 and $\bar{y} = \frac{1}{n} \sum_{i=1}^n y_i$ are the sample means.

1539 In practice we used the python function `scipy.stats.pearsonr` to calculate the
 1540 correlation coefficients.

1541 **Total correlations, r_{SC}**

1542 The total correlation (r_{SC}) of two cells is the correlation between the spike counts of those
 1543 cells in response to a given stimulus condition.

1544 **Shuffled total correlations**

1545 We measured the shuffled total correlations between two neurons by randomly permuting one
 1546 of the neuron's spike counts and measuring the total correlations. These shuffled correlations
 1547 were useful when measuring the effect of time bin width on correlations, and when decid-
 1548 ing which correlations should be preserved when creating correlation networks (see section
 1549 3.5.5).

1550 **Separating Correlations & Anti-correlations**

1551 In order to compare the effect of bin width on measures of negative r_{SC} (anti-correlation) and
 1552 positive r_{SC} separately, we had to separate correlated and anti-correlated pairs. To do this, we

simply measured the mean r_{SC} , taking the mean across all the bin widths. If this quantity was positive or zero we regarded the pair as positively correlated. If this quantity was negative we regarded the pair as anti-correlated.

3.5.3 Conditioning on behavioural data

Our behavioural data consisted of the top 500 principal components (PCs) of a processed video recording of the mouse's face (see section 3.4.2). Denoting the spike count of a given cell by X , and the PCs by Z_1, \dots, Z_{500} , we wanted to model X as a function of Z_1, \dots, Z_{500} in order to estimate

$$E[X|Z_1, \dots, Z_{500}] = \int_{x \in X} x P(X = x|Z_1, \dots, Z_{500}) dx \quad (3.4)$$

$$= \int_{x \in X} x \frac{P(X = x, Z_1, \dots, Z_{500})}{P(Z_1, \dots, Z_{500})} dx \quad (3.5)$$

Given the 500 components, a naïve estimation of $P(Z_1, \dots, Z_{500})$ or $P(X, Z_1, \dots, Z_{500})$ by histogramming was impossible. Therefore we modelled X as a linear combination of the PCs.

Linear regression

We modelled the spike count of a given cell, X , as a linear combination of the PCs of the video of the mouse's face, $\mathbf{Z} = Z_1, \dots, Z_{500}$. We tried three different types of regularization

• $L1$ or 'Lasso'

• $L2$ or 'Ridge regression'

• 'Elastic net' regularisation (a linear combination of both $L1$ and $L2$ regularisation penalties)

The elastic net regularisation performed the best, so we stuck with that.

Elastic net regularisation

Suppose we wish to model n observations of a random variable X , $\mathbf{x} = (x_1, \dots, x_n)$ using n instances of m predictors $\mathbf{Z} = (Z_1, \dots, Z_m)$. The naïve elastic net criterion is

$$L(\lambda_1, \lambda_2, \boldsymbol{\beta}) = |\mathbf{x} - \mathbf{Z}\boldsymbol{\beta}|^2 + \lambda_2|\boldsymbol{\beta}|_2 + \lambda_1|\boldsymbol{\beta}|_1 \quad (3.6)$$

where

$$|\boldsymbol{\beta}|_2 = \sum_{j=1}^m \beta_j^2 \quad (3.7)$$

$$|\boldsymbol{\beta}|_1 = \sum_{j=1}^m |\beta_j| \quad (3.8)$$

The naïve elastic net estimator $\hat{\boldsymbol{\beta}}$ is the minimiser of the system of equations 3.6 (Zou and Hastie, 2005)

$$\hat{\boldsymbol{\beta}} = \arg \min_{\boldsymbol{\beta}} L(\lambda_1, \lambda_2, \boldsymbol{\beta}) \quad (3.9)$$

1569 We implemented the model using the `ElasticNetCV` method of Python's
1570 `sklearn.linear_models` package.

1571 As well as using the PCs, we also tried fitting the models using the raw video data recon-
1572 structed from the PCs and eigenvectors. These models performed worse than those using the
1573 PCs. We expected this because each representation contains the same amount of information,
1574 but the raw video representation spreads this information across many more components.
1575 This requires more parameter fitting, but given the same information.

1576 **Conditional covariance**

We calculated the expected value of the conditional covariance using the law of total covari-
ance.

$$\text{cov}(X, Y) = E[\text{cov}(X, Y|Z)] + \text{cov}(E[X|Z], E[Y|Z]) \quad (3.10)$$

1577 where these expected values are calculated with respect to the distribution of Z as a random
1578 variable.

1579 The law of total covariance breaks the covariance into two components. The first com-
1580 ponent $E[\text{cov}(X, Y|Z)]$ is the expected value, under the distribution of Z , of the conditional
1581 covariance $\text{cov}(X, Y|Z)$. This covariance could be interpreted as the unnormalised version
1582 of what Cohen et al. (2011) call the spike count correlation (Cohen and Kohn, 2011), aka.
1583 the noise correlation. In particular, this is the covariance of the spike counts in response to
1584 repeated presentation of identical stimuli.

1585 The second component is analogous to what Cohn et al. (2011) call the *signal correlation*
1586 (Cohen and Kohn, 2011). In particular, $\text{cov}(E[X|Z], E[Y|Z])$ is the covariance between

1587 spike counts in response to different stimuli.

Using our linear model, we calculated $E[X|Z_1, \dots, Z_{500}]$ for each cell X. Then we proceeded to calculate

$$E[\text{cov}(X, Y|Z_1, \dots, Z_{500})] = \text{cov}(X, Y) - \quad (3.11)$$

$$\text{cov}(E[X|Z_1, \dots, Z_{500}], E[Y|Z_1, \dots, Z_{500}]) \quad (3.12)$$

1588 **Measures of conditional correlation**

As a measure of expected correlation, we measured the ‘event conditional correlation’ (Maugis, 2014)

$$\rho_{XY|Z} = \frac{E[\text{cov}(X, Y|Z)]}{\sqrt{E[\text{var}(X|Z)]}E[\text{var}(Y|Z)]} \quad (3.13)$$

1589 Although this is not an actual correlation, it is an intuitive analogue to the correlation as a
1590 normalised version of the covariance.

For comparison, we also measured the ‘signal correlation’

$$\rho_{\text{signal}} = \frac{\text{cov}(E[X|Z], E[Y|Z])}{\sqrt{\text{var}(E[X|Z])}\sqrt{\text{var}(E[Y|Z])}} \quad (3.14)$$

1591 this is an actual correlation.

1592 **3.5.4 Information Theory**

1593 **Entropy $H(X)$**

The entropy of a random variable X, with outcomes x_1, \dots, x_N , and corresponding probabilities p_1, \dots, p_N is defined as

$$H(X) = - \sum_{n=1}^N p_n \log_2 p_n \quad (3.15)$$

1594 This quantity is also known as the information entropy or the ‘surprise’. It measures the
1595 amount of uncertainty in a random variable. For example, a variable with a probability of 1
1596 for one outcome, and 0 for all other outcomes will have 0 bits entropy, because it contains no
1597 uncertainty. But a variable with a uniform distribution will have maximal entropy as it is the
1598 least predictable. This quantity is analogous to the entropy of a physical system (Shannon,

1599 1948). Note that any base may be used for the logarithm in equation 3.15, but using base 2
 1600 means that the quantity will be measured in ‘bits’.

The joint entropy of two jointly distributed random variables X and Y , where Y has outcomes y_1, \dots, y_M , is defined as

$$H(X, Y) = - \sum_{n=1}^N \sum_{m=1}^M P(X = x_n, Y = y_m) \log_2 P(X = x_n, Y = y_m) \quad (3.16)$$

1601 If X and Y are independent then $H(X, Y) = H(X) + H(Y)$. Otherwise $H(X, Y) <$
 1602 $H(X) + H(Y)$. When X and Y are completely dependent $H(X, Y) = H(X) = H(Y)$.

The conditional entropy of Y conditioned on X is defined as

$$H(Y|X) = - \sum_{n=1}^N \sum_{m=1}^M P(X = x_n, Y = y_m) \log_2 \frac{P(X = x_n, Y = y_m)}{P(X = x_n)} \quad (3.17)$$

1603 When X and Y are independent $H(Y|X) = H(Y)$. Intuitively, we learn nothing of Y by
 1604 knowing X , so Y is equally uncertain whether we know X or not. If Y is totally dependent
 1605 on X , then the fraction in the logarithm is 1, which gives $H(Y|X) = 0$.

1606 These entropy measures are the basis of the mutual information measure.

1607 Maximum entropy limit

When spiking data is binned into spike counts there is an upper limit on the entropy of these data. The maximum entropy discrete distribution is the discrete uniform distribution. A random variable with this distribution will take values from some finite set with equal probabilities. Binned spike count data will take values between 0 and some maximum observed spike count n_{\max} . A neuron with responses that maximises entropy will take these values with equal probability, i.e. if $i \in \{0, \dots, n_{\max}\}$ then $P(X = i) = \frac{1}{n_{\max}+1}$. The entropy of this neuron will be

$$\begin{aligned} H(X) &= - \sum_{i=0}^{n_{\max}} P(X = i) \log_2 P(X = i) \\ &= - \sum_{i=0}^{n_{\max}} \frac{1}{n_{\max}+1} \log_2 \left(\frac{1}{n_{\max}+1} \right) \\ &= - \log_2 \left(\frac{1}{n_{\max}+1} \right) \\ &= \log_2 (n_{\max} + 1) \end{aligned}$$

1608 Therefore, the maximum entropy of the binned spike counts of a neuron is $\log_2(n_{\max} + 1)$.
 1609 Of course, it would be very unusual for a neuron to fire in accordance with the discrete
 1610 uniform distribution. Most measurements of entropy taken on binned spiking data will be
 1611 much lower than the maximum. See figure 3.17 to see the maximum entropy as a function of
 1612 the maximum observed spike count.

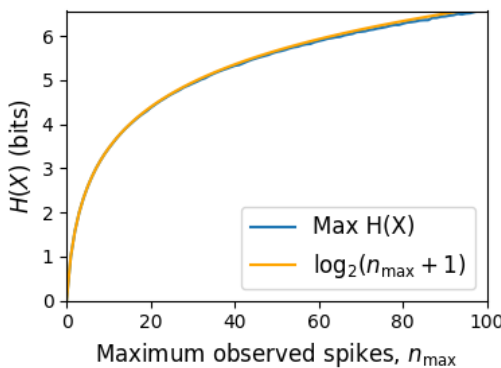


FIGURE 3.17: **Entropy Limit:** The upper limit on entropy of binned spike count data as a function of the maximum observed spike count. The orange line is the analytical maximum. The blue line is the entropy of samples with $N = 1000$ data points taken from the discrete uniform distribution.

1613 **Mutual Information $I(X; Y)$**

1614 The mutual information can be defined mathematically in a number of ways, all of which are
 1615 equivalent. These definitions illustrate the different ways of interpreting the mutual informa-
 1616 tion.

For two jointly distributed random variables X and Y , the mutual information $I(X; Y)$ is defined as

$$I(X; Y) = H(Y) - H(Y|X) \quad (3.18)$$

$$= H(X) - H(X|Y) \quad (3.19)$$

1617 Equation 3.18 fits with the following intuition: The mutual information between X and Y is
 1618 the reduction in uncertainty about X gained by knowing Y , or vice versa. We could also say
 1619 the mutual information is the amount of information gained about X by knowing Y , or vice
 1620 versa.

Another useful entropy based definition for the mutual information is

$$I(X; Y) = H(X) + H(Y) - H(X, Y) \quad (3.20)$$

1621 This definition is useful because it does not require the calculation of conditional probabilities.
 1622

The mutual information can also be defined in terms of marginal, joint, and conditional distributions. For example,

$$I(X;Y) = - \sum_{n=1}^N \sum_{m=1}^M P(X = x_n, Y = y_m) \log_2 \frac{P(X = x_n, Y = y_m)}{P(X = x_n)P(Y = y_m)} \quad (3.21)$$

Notice that this can be rewritten as a Kullback–Leibler divergence.

$$I(X;Y) = D_{KL}(P(X,Y) || P(X)P(Y)) \quad (3.22)$$

1623 So, we can also think of the mutual information as a measure of the difference between
 1624 the joint distribution of X and Y , and the product of their marginal distributions. Since the
 1625 product of the marginal distributions is the joint distribution for independent variables, we
 1626 can think of the mutual information as a measure of the variables' dependence on one another.

1627 The minimum value that $I(X;Y)$ can take is 0. This occurs when the random variables
 1628 X and Y are independent. Then we have $H(X|Y) = H(X)$, and $H(Y|X) = H(Y)$, which
 1629 according to equation 3.18, gives $I(X;Y) = 0$. We also have that $H(X,Y) = H(X) +$
 1630 $H(Y)$ in this case, which according equation 3.20, gives $I(X;Y) = 0$. Finally, we also have
 1631 $P(X,Y) = P(X)P(Y)$, which leaves us with 1 in the argument for the logarithm in equation
 1632 3.21, which again gives $I(X;Y) = 0$.

1633 The mutual information reaches its maximum value when one of the variables X and
 1634 Y is completely determined by knowing the value of the other. In that case $I(X;Y) =$
 1635 $\min\{H(X), H(Y)\}$.

1636 Variation of Information $VI(X,Y)$

The variation of information is another information theoretical quantity based on the mutual information. It is defined as

$$VI(X;Y) = H(X) + H(Y) - 2I(X;Y) \quad (3.23)$$

We can rewrite this as the summation of two positive quantities

$$VI(X;Y) = [H(X) - I(X;Y)] + [H(Y) - I(X;Y)] \quad (3.24)$$

1637 In English, the variation of information is the summation of the uncertainty in the random
1638 variables X and Y excluding the uncertainty shared by those variables.

1639 This measure will become more relevant when we go on to talk about clusterings because
1640 $VI(X; Y)$ forms a metric on the space of clusterings.

1641 **Measuring entropies & mutual information**

1642 In practice, we measured the mutual information between spike counts using Python and the
1643 python package `pyitlib`. We used the PT-bias correction technique to estimate the bias of
1644 our measurements when measuring the mutual information between the spike counts of two
1645 cells (Treves and Panzeri, 1995).

1646 When measuring the mutual information between clusterings we used Python, but we
1647 used the `mutual_info_score`, `adjusted_mutual_info_score`, and
1648 `normalized_mutual_info_score` functions from the `sklearn.metrics` part of
1649 the `sklearn` package.

1650 **3.5.5 Network analysis**

1651 **Correlation networks**

1652 In order to analyse functional networks created by the neurons in our ensemble, we mea-
1653 sured the total correlation between each pair of neurons. These measurements induced an
1654 undirected weighted graph/network between the neurons. The weight of each connection
1655 was equal to the total correlation between each pair of neurons.

1656 We followed the same procedure for total correlations 3.5.2, spike count correlations, and
1657 signal correlations 3.5.3.

1658 **Rectified correlations**

1659 At the time of writing, the community detection method outlined in (Humphries et al., 2019)
1660 could only be applied to networks with positively weighted connections. But many neuron
1661 pairs were negatively correlated. To apply the community detection method, we *rectified* the
1662 network, by setting all the negative weights to zero.

1663 We also looked for structure in the network created by negative correlations by reversing
1664 the signs of the correlations, and rectifying these correlations before applying our network
1665 analysis.

1666 Finally, we used the absolute value of the correlations as the weights for the graph/network.
1667 By doing this, we hoped to identify both correlated and anti-correlated functional communi-
1668 ties of neurons.

1669 **Sparsifying data networks**

1670 When creating our correlation networks, we wanted to exclude any correlations that could
1671 be judged to exist ‘by chance’. To do this, we measured the 5th and 95th percentile of
1672 the shuffled correlations (see section 3.5.2) for the given mouse and time bin width. We
1673 then set all the data correlations between these two values to 0. This excluded any ‘chance’
1674 correlations from our network, and created a sparser network. This allowed us to make use
1675 of the ‘sparse weighted configuration model’ as described in section 3.5.5.

1676 **Communities**

1677 Given some network represented by an adjacency matrix \mathbf{A} , a community within that net-
1678 work is defined as a collection of nodes where the number of connections within these nodes
1679 is higher than the expected number of connections between these nodes. In order to quan-
1680 tify the ‘expected’ number of connections, we need a model of expected networks. This is
1681 analogous to a ‘null model’ in traditional hypothesis testing. We test the hypothesis that our
1682 data network departs from the null network model to a statistically significant degree. For
1683 undirected unweighted networks, the canonical model of a null network is the configuration
1684 model (Fosdick et al., 2016). Since we are working with weighted sparse networks, we used
1685 more suitable null models, described below.

1686 **Weighted configuration model**

1687 The *weighted configuration model* is a canonical null network model for weighted networks.
1688 Given some data network, the weighted configuration model null network will preserve the
1689 degree sequence and weight sequence of each node in the data network. But the edges will
1690 be distributed randomly (Fosdick et al., 2016). Any structure in the data network beyond
1691 its degree sequence and weight sequence will not be captured in the weighted configuration
1692 model. So, this model can be used in testing the hypothesis that this extra structure exists.

1693 **Sparse weighted configuration model**

1694 The *sparse weighted configuration model* is another null network model. Similar in nature to
1695 the weighted configuration model (see section 3.5.5), but the sparsity of the data network is

1696 preserved in the null network. This is achieved by sampling from a probability distribution
 1697 for the creation or non-creation of each possible connection, then distributing the weight of
 1698 the data network randomly in this sparse network (Humphries et al., 2019). This is the null
 1699 network that we used when searching for additional structure in our data networks.

1700 **Spectral rejection**

1701 We made use of the spectral rejection algorithm as outlined in (Humphries et al., 2019). The
 1702 spectral rejection algorithm is a method for finding structure in a network not captured by a
 1703 supposed null model, if such structure exists.

To describe the method, we denote our data network matrix \mathbf{W} , we denote the expected network of our null network model as $\langle \mathbf{P} \rangle$. Then the departure of our data network from the null network can be described by the matrix

$$\mathbf{B} = \mathbf{W} - \langle \mathbf{P} \rangle \quad (3.25)$$

1704 a common choice for $\langle \mathbf{P} \rangle$ in community detection is the ‘configuration model’ (Fosdick et
 1705 al., 2016; Humphries, 2011). The matrix \mathbf{B} is often called the configuration matrix, in this
 1706 context we will use the term ‘deviation matrix’ as it captures the deviation of \mathbf{W} from the
 1707 null model.

1708 To test for structure in the network represented by \mathbf{W} , we examine the eigenspectrum of \mathbf{B}
 1709 and compare it to the eigenspectrum of our null model. Firstly, note that since our data model
 1710 doesn’t allow self loops, and is not directed, the matrix representing the network will be
 1711 symmetric and positive semi-definite, and will therefore be invertible with real eigenvalues.
 1712 We selected a null model with the same characteristics.

1713 To find the eigenspectrum of the null model, we generated N samples from our null
 1714 model P_1, \dots, P_N , and we measured their deviation matrices B_1, \dots, B_N . We then calculated
 1715 the eigenspectrum of each of those samples. We calculated the upper bound of the null model
 1716 eigenspectrum by taking the mean of the largest eigenvalues of B_1, \dots, B_N . We calculated a
 1717 lower bound on the null model eigenspectrum by taking the mean of the smallest eigenvalues
 1718 of B_1, \dots, B_N .

1719 We then calculated the eigenspectrum of \mathbf{B} , our data network deviation matrix. If any of
 1720 those eigenvalues lay outside of the upper or lower bounds of the null model eigenspectrum,
 1721 this is evidence of additional structure not captured by the null model. If we chose the sparse
 1722 weighted configuration model (see section 3.5.5) as our null network model, then eigenvalues

1723 lying below the lower bound indicate k -partite structure in the network. For example, if one
1724 eigenvalue lay below the lower bound, this would indicate some bipartite structure in the data
1725 network. If any eigenvalues lay above the upper bound of the null model eigenspectrum, this
1726 is evidence of community structure in the data network. For example, one eigenvalue of \mathbf{B}
1727 lying above the upper bound of the null model eigenspectrum indicates the presence of two
1728 communities in the network (Humphries, 2011).

1729 **Node rejection**

1730 If there are d data eigenvalues lying outside of the null network eigenspectrum, the d eigen-
1731 vectors corresponding to these eigenvalues will form a vector space. If we project the nodes
1732 of our network into this vector space, by projecting either rows or columns of the data ma-
1733 trix, we can see how strongly each node contributes to the vector space. Nodes that contribute
1734 strongly to the additional structure will project far away from the origin, nodes that do not
1735 contribute to the additional structure will project close to the origin. We want to use this
1736 information to discard those nodes that do not contribute.

1737 We can test whether a node projects *far* away from the origin or *close* to the origin
1738 using the eigenvalues and eigenvectors of B_1, \dots, B_N . The j th eigenvector and eigenvalue
1739 of B_i gives a value for a null network's projection into the j th dimension of the additional
1740 structure vector space. The matrices B_1, \dots, B_N give N projections into that dimension.
1741 These projections are a distribution of the null networks' projections. If the data node's
1742 projection exceeds that of the null network projections this node is judged to project *far* from
1743 the origin, and therefore contribute to the additional structure. Otherwise, the node is judged
1744 to project *close* to the origin, and is therefore rejected (Humphries et al., 2019).

1745 **Community detection**

1746 Another application for this d dimensional space is community detection. We first project
1747 all of the nodes into this d -dimensional space, then perform the clustering in this space. The
1748 clustering and community detection procedure is described in (Humphries, 2011).

1749 In practice, the procedure is carried out n times (we chose $n = 100$ times), this returns n
1750 clusterings. We resolve these n clusterings to one final clustering using *consensus clustering*.
1751 We used the consensus clustering method that uses an explicit null model for the consensus
1752 matrix, as outlined in (Humphries et al., 2019).

3.5.6 Clustering Comparison

A clustering \mathcal{C} is a partition of a set D into sets C_1, C_2, \dots, C_K , called clusters, that satisfy the following for all $k, l \in \{1, \dots, K\}$:

$$C_k \cap C_l = \emptyset \quad (3.26)$$

$$\bigcup_{k=1}^K C_k = D \quad (3.27)$$

If we consider two clusterings, \mathcal{C} with clusters C_1, C_2, \dots, C_K and \mathcal{C}' with clusters C'_1, C'_2, \dots, C'_K . There are a number of measurements we can use to compare \mathcal{C} and \mathcal{C}' . In the following, the number of elements in D is denoted by n , and the number of elements in cluster C_k is n_k .

Adjusted Rand Index

The *adjusted Rand Index* is a normalised similarity measure for clusterings based on pair counting.

If we consider the clusterings \mathcal{C} and \mathcal{C}' , and denote

- the number of pairs in the same cluster in \mathcal{C} and \mathcal{C}' by N_{11}

- the number of pairs in different clusters in \mathcal{C} and \mathcal{C}' by N_{00}

- the number of pairs in the same cluster in \mathcal{C} and different clusters in \mathcal{C}' by N_{10}

- the number of pairs in different clusters in \mathcal{C} and the same cluster in \mathcal{C}' by N_{01}

then the *Rand Index* is defined as

$$RI = \frac{N_{11} + N_{00}}{N_{11} + N_{00} + N_{10} + N_{01}} = \frac{N_{11} + N_{00}}{\binom{n}{2}} \quad (3.28)$$

The Rand Index is 1 when the clusterings are identical, and 0 when the clusterings are completely different.

The *adjusted Rand Index* intends on correcting the Rand Index for chance matching pairs.

This is defined as

$$ARI = \frac{2(N_{00}N_{11} - N_{01}N_{10})}{(N_{00} + N_{01})(N_{01} + N_{11}) + (N_{00} + N_{10})(N_{10} + N_{11})} \quad (3.29)$$

The adjusted Rand Index is 1 when the clusterings are identical, and 0 when the Rand Index is equal to its expected value.

1770 **Clusterings as random variables**

If we take any random element of D , the probability that this element is in cluster C_k of clustering \mathcal{C} is

$$P(K = k) = \frac{n_k}{n} \quad (3.30)$$

1771 this defines a probability distribution, which makes the clustering a random variable. Any
1772 clustering can be considered as a random variable this way.

This means that we can measure any of the information theoretic quantities defined in section 3.5.4 with respect to clusterings. For example, the entropy of a clustering is

$$H(\mathcal{C}) = - \sum_{k=1}^K \frac{n_k}{n} \log \frac{n_k}{n} \quad (3.31)$$

If we have two clusterings, the joint probability distribution of these clusterings is defined as

$$P(K = k, K' = k') = \frac{|C_k \cap C'_{k'}|}{n} \quad (3.32)$$

1773 The joint distribution allows us to define the mutual information between two clusterings,
1774 $I(\mathcal{C}; \mathcal{C}')$ (Meilă, 2007).

1775 **Information based similarity measures**

The mutual information between two clusterings is a similarity measure, with $I(\mathcal{C}; \mathcal{C}') = 0$ if \mathcal{C} and \mathcal{C}' are completely different, and $I(\mathcal{C}; \mathcal{C}') = H(\mathcal{C}) = H(\mathcal{C}')$ if \mathcal{C} and \mathcal{C}' are identical. This can be normalised in a number of different ways to make more similarity measures (Vinh, Epps, and Bailey, 2010)

$$NMI_{joint} = \frac{I(\mathcal{C}; \mathcal{C}')}{H(\mathcal{C}, \mathcal{C}')} \quad (3.33)$$

$$NMI_{max} = \frac{I(\mathcal{C}; \mathcal{C}')}{\max\{H(\mathcal{C}), H(\mathcal{C}')\}} \quad (3.34)$$

$$NMI_{sum} = \frac{2I(\mathcal{C}; \mathcal{C}')}{H(\mathcal{C}) + H(\mathcal{C}')} \quad (3.35)$$

$$NMI_{sqrt} = \frac{I(\mathcal{C}; \mathcal{C}')}{\sqrt{H(\mathcal{C})H(\mathcal{C}')}} \quad (3.36)$$

$$NMI_{min} = \frac{I(\mathcal{C}; \mathcal{C}')}{\min\{H(\mathcal{C}), H(\mathcal{C}')\}} \quad (3.37)$$

We can control for chance similarities between the two clusterings by measuring the *adjusted mutual information* between the clusterings. This is defined as

$$AMI_{sum} = \frac{I(\mathcal{C}; \mathcal{C}') - E\{I(\mathcal{C}; \mathcal{C}')\}}{\frac{1}{2}[H(\mathcal{C}) + H(\mathcal{C}')] - E\{I(\mathcal{C}; \mathcal{C}')\}} \quad (3.38)$$

1776 The first term in the denominator, taking the average of the marginal entropies, can be re-
1777 placed by taking the maximum, minimum, or the geometric mean (Vinh, Epps, and Bailey,
1778 2010).

1779 Information based metrics

The variation of information between two clusterings $VI(\mathcal{C}; \mathcal{C}')$ (see section 3.5.4) is a metric on the space of clusterings (Meilă, 2007). That is,

$$VI(\mathcal{C}; \mathcal{C}') \geq 0 \quad (3.39)$$

$$VI(\mathcal{C}; \mathcal{C}') = 0 \iff \mathcal{C} = \mathcal{C}' \quad (3.40)$$

$$VI(\mathcal{C}; \mathcal{C}') = VI(\mathcal{C}'; \mathcal{C}) \quad (3.41)$$

$$VI(\mathcal{C}; \mathcal{C}'') \leq VI(\mathcal{C}; \mathcal{C}') + VI(\mathcal{C}'; \mathcal{C}'') \quad (3.42)$$

Another metric is the *information distance* (Vinh, Epps, and Bailey, 2010)

$$D_{max} = \max\{H(\mathcal{C}), H(\mathcal{C}')\} - I(\mathcal{C}; \mathcal{C}') \quad (3.43)$$

Both of these can be normalised

$$NVI(\mathcal{C}; \mathcal{C}') = 1 - \frac{I(\mathcal{C}; \mathcal{C}')}{H(\mathcal{C}, \mathcal{C}')} \quad (3.44)$$

$$d_{max} = 1 - \frac{I(\mathcal{C}; \mathcal{C}')}{\max\{H(\mathcal{C}), H(\mathcal{C}')\}} \quad (3.45)$$

1780 Comparing detected communities and anatomical divisions

1781 In order to quantify the difference or similarity between the communities detected in our cor-
1782 relation network and the anatomical classification of the cells in that network, we considered
1783 the communities and the anatomical regions as clusters in two different clusterings, \mathcal{C}_{comm}
1784 and \mathcal{C}_{anat} , respectively. We then measured the similarity between the clusterings using the
1785 mutual information, the adjusted mutual information, and the normalised mutual informa-
1786 tion. We measured the difference between, or the distance between, the clusterings using the

1787 variation of information, the normalised variation of information, and the normalised infor-
1788 mation distance. We also measured the difference between the clusterings using the adjusted
1789 Rand Index, just to use a non-information based measure.

1790 We took all of these measures for communities detected using different time bin widths.
1791 This gave us an idea of the effect of time bin width on correlation networks in neural ensem-
1792 bles relative to anatomical regions within those ensembles.

1793 **Chapter 4**

1794 **A simple two parameter distribution
for modelling neuronal activity and
capturing neuronal association**

1797 *Abstract*

1798 Recent developments in electrophysiological technology have lead to an increase in the size
1799 of electrophysiology datasets. Consequently, there is a requirement for new analysis tech-
1800 niques that can make use of these new datasets, while remaining easy to use in practice. In
1801 this work, we fit some one or two parameter probability distributions to spiking data collected
1802 from a mouse exposed to visual stimuli. We show that the Conway-Maxwell-binomial dis-
1803 tribution is a suitable model for the number of active neurons in a neuronal ensemble at any
1804 given moment. This distribution fits these data better than binomial or beta-binomial distribu-
1805 tions. It also captures the correlated activity in the primary visual cortex induced by stimulus
1806 onset more effectively than simply measuring the correlations, at short timescales (< 10ms).
1807 We also replicate the finding of Churchland et al (2010) relating to stimulus onset quenching
1808 neural variability in cortical areas, and we show a correspondence between this quenching
1809 and changes in one of the parameters of the fitted Conway-Maxwell-binomial distributions.

4.1 Introduction

Recent advances in electrophysiological technology, such as ‘Neuropixels’ probes (Jun et al., 2017) have allowed extracellular voltage measurements to be collected from larger numbers of cells than traditional methods, in multiple brain regions simultaneously, and routinely. These larger datasets require innovative methods to extract information from the data in a reasonable amount of time, ‘reasonable’ being subjective in this case.

Theoretically, all the information at any given moment in an electrophysiological dataset with n neurons could be captured by calculating the probability distribution for every possible spiking pattern. This would require defining a random variable with 2^n possible values, a task that quickly becomes impossible as n increases. Attempts at approximating this random variable often involve measuring pairwise or higher order correlations (Schneidman et al., 2006; Flach, 2013; Ganmor, Segev, and Schneidman, 2011). But pairwise correlations may not be enough to characterise instantaneous neural activity (Tkačik et al., 2014). Furthermore, these kinds of models tend to ignore the temporal structure of neuronal data, in favour of smaller model size, and scalability.

Higher order correlations would be helpful here, but defining these correlations can be tricky, never-mind quantifying them. If we use the interaction parameters arising from the exponential family model as measures of higher order correlations, measuring these correlations becomes computationally impractical quite quickly also (the number of ‘three neuron correlations’ to measure scales with $(n \choose 3)$). In this paper, we dispense with measuring correlations directly, and attempt to characterise correlated behaviour by measuring ‘association’; a more general concept that includes correlation.

In this work, we examined the ability of simple distributions to model the number of active (spiking) neurons in a neuronal ensemble at any given timepoint. We compared a little-known distribution named the Conway-Maxwell-binomial distribution to the binomial distribution and the beta-binomial distribution. The binomial distribution is a probability distribution over the number of successes in a sequence of independent and identical Bernoulli trials. The beta-binomial distribution is similar, but allows for a bit more flexibility while still being a model for heterogeneity. Similar to the binomial and beta-binomial, the Conway-Maxwell-binomial distribution is a probability distribution over the number of successes in a series of Bernoulli trials, but allows over- and under-dispersion relative to the binomial distribution. This distribution should therefore be a good candidate for our purposes. We found that Conway-Maxwell-binomial distribution was usually the best candidate of the three that

1843 we examined.

1844 We also observed some interesting changes in the number of active neurons in the primary
1845 visual cortex and hippocampus at stimulus onset and some changes in this activity in the
1846 thalamus which were sustained for the full duration of the stimulus presentation. This let us
1847 know that there were some responses to model.

1848 We found that fitting a Conway-Maxwell-binomial distribution was a better method of
1849 capturing association between neurons than measuring the spike count correlation for the
1850 short time bins that we used (< 10ms).

1851 Finally, we also wanted to investigate parallels between the parameters of the Conway-
1852 Maxwell-binomial distribution and quantities that have been established as relevant to sen-
1853 sory processing. So, we replicated the findings made by Churchland et al. (2010) relating
1854 to a reduction in neural variability at stimulus onset in the macaque cortical regions, but for
1855 data taken from the mouse primary visual cortex. We compared these findings to the values
1856 of the fitted Conway-Maxwell-binomial distribution parameters.

1857 4.2 Data

1858 We used data collected by Nick Steinmetz and his lab ‘CortexLab at UCL’ (Steinmetz, Caran-
1859 dini, and Harris, 2019). The data can be found online ¹ and are free to use for research
1860 purposes.

1861 Two ‘Phase3’ Neuropixels (Jun et al., 2017) electrode arrays were inserted into the brain
1862 of an awake, head-fixed mouse for about an hour and a half. These electrode arrays recorded
1863 384 channels of neural data each at 30kHz and less than $7\mu\text{V}$ RMS noise levels. The sites
1864 are densely spaced in a ‘continuous tetrode’-like arrangement, and a whole array records
1865 from a 3.8mm span of the brain. One array recorded from visual cortex, hippocampus, and
1866 thalamus, the other array recorded from motor cortex and striatum. The data were spike-
1867 sorted automatically by Kilosort and manually by Nick Steinmetz using Phy. In total 831
1868 well-isolated individual neurons were identified.

1869 4.2.1 Experimental protocol

1870 The mouse was shown a visual stimulus on three monitors placed around the mouse at right
1871 angles to each other, covering about ± 135 degrees azimuth and ± 35 degrees elevation.

¹<http://data.cortexlab.net/dualPhase3/>

1872 The stimulus consisted of sine-wave modulated full-field drifting gratings of 16 drift di-
1873 rections ($0^\circ, 22.5^\circ, \dots, 337.5^\circ$) with 2Hz temporal frequency and 0.08 cycles/degree spatial
1874 frequency displayed for 2 seconds plus a blank condition. Each of these 17 conditions were
1875 presented 10 times in a random order across 170 different trials. There were therefore 160
1876 trials with a drifting-grating visual stimulus present, and 10 trials with a blank stimulus.

1877 **4.3 Methods**

1878 **4.3.1 Binning data**

1879 We converted the spike times for each cell into spike counts by putting the spike times into
1880 time bins of a given ‘width’ (in milliseconds). We used time bins of 1ms, 5ms, and 10ms.
1881 We used different time bin widths to assess the impact of choosing a bin width.

1882 **4.3.2 Number of *active* neurons**

1883 To count the number of active neurons in each neuronal ensemble, we split the time interval
1884 for each trial into bins of a given width. We counted the number of spikes fired by each cell
1885 in each bin. If a cell fired *at least* one spike in a given bin, we regarded that cell as active in
1886 that bin. We recorded the number of active cells in every bin, and for the purposes of further
1887 analysis, we recorded each cell’s individual spike counts.

1888 It should be noted that when we used a bin width of 1ms, the maximum number of
1889 spikes in any bin was 1. For the wider time bins, some bins had spike counts greater than
1890 1. Consequently when using a bin width of 1ms, the number of active neurons and the total
1891 spike count of a given bin were identical. But for wider bin widths, the total spike count was
1892 greater than the number of active neurons.

1893 So for the 1ms bin width, the activity of a neuron and the number of spikes fired by that
1894 neuron in any bin can be modelled as a Bernoulli variable. But for wider time bins, only the
1895 activity can be modelled in this way.

1896 **4.3.3 Moving windows for measurements**

1897 When taking measurements (e.g. moving average over the number of active neurons) or
1898 fitting distributions (eg. the beta binomial distribution) we slid a window containing a certain
1899 number of bins across the data, and made our measurements at each window position. For
1900 example, when analysing 1ms bin data, we used a window containing 100 bins, and we slid

Bin width (ms)	Window size (bins)	Window size (ms)	Windows per trial
1ms	100	100ms	296
5ms	40	200ms	286
10ms	40	400ms	266

TABLE 4.1: Details of the different bin width and analysis window sizes used when binning spike times, and analysing those data.

1901 the window across the time interval for each trial moving 10 bins at a time. So that for
 1902 3060ms of data, we made 296 measurements.

1903 For the 5ms bin width data, we used windows containing 40 bins, and slid the window 2
 1904 bins at a time when taking measurements.

1905 For the 10ms bin width data, we used windows containing 40 bins, and slid the window
 1906 1 bin at a time when taking measurements (see table 4.1 for concise details).

1907 By continuing to use windows containing 40 bins, we retained statistical power but sac-
 1908 rificed the number of measurements taken.

1909 There was an interval between each trial with a grey image in place of the moving of
 1910 the moving bar stimulus. This interval varied in time. But we included some of this interval
 1911 when recording the data for each trial. We started recording the number of active neurons,
 1912 and the number of spikes from each neuron from 530ms before each trial until 1030ms after
 1913 each trial. This way, we could see the change in our measurements at the onset of a stimulus
 1914 and the end of stimulus presentation.

1915 As mentioned in section 4.3.2, we recorded the number of active neurons in each bin, and
 1916 the spike count for each neuron in each bin. The actual measurements we took using these
 1917 data in each window were as follows:

1918 **Moving average** The average number of active cells in each window.

1919 **Moving variance** The variance of the number of active cells in each window.

1920 **Average correlation** We measured the correlation between the spike counts of each pair of
 1921 cells in the ensemble, and took the average of these measurements.

1922 **Binomial p** We fitted a binomial distribution to the data in each window and recorded the
 1923 fitted probability of success, p in each case.

1924 **Beta-binomial α, β** We fitted a beta-binomial distribution to the data in each window, and
 1925 recorded the values of the fitted shape parameters, α and β , of each distribution.

1926 **Conway-Maxwell-binomial distribution p, ν** We fitted a Conway-Maxwell-binomial dis-
 1927 tribution to the data in each window, and recorded the fitted values of p and ν for each
 1928 distribution.

1929 **Log-likelihoods** We also recorded the log-likelihood of each of the fitted distributions for
 1930 each window.

1931 **4.3.4 Fano factor**

The *Fano factor* of a random variable is defined as the ratio of the variable's variance to its mean.

$$F = \frac{\sigma^2}{\mu} \quad (4.1)$$

1932 We measured the Fano factor of the spike count of a given cell by measuring the mean and
 1933 variance of the spike count across trials, and taking the ratio of those two quantities. When
 1934 calculated in this way the Fano factor can be used as a measure of neural variability that
 1935 controls for changes in the firing rate. This is similar to the calculation used in (**churchland**).

1936 **4.3.5 Probability Distributions suitable for modelling ensemble activity**

1937 We present here three different probability distributions that could be suitable to model the
 1938 number of active neurons in an ensemble. Each distribution has the set $\{0, \dots, n\}$ as its sup-
 1939 port, where n is the number of neurons in the ensemble. These are simple distributions with
 1940 either two or three parameters each. However, we regard n as known when using these dis-
 1941 tributions for modelling, so in effect each distribution has either one or two free parameters.

1942 **Association**

1943 *Association* between random variables is similar to the correlation between random variables
 1944 but is more general in concept. The correlation is a measure of association; and association
 1945 doesn't have a mathematical definition like correlation does. Essentially, the association
 1946 between two random variables is their tendency to take the same or similar values. Positively
 1947 associated variables tend to take the same value, and negatively associated variables tend to
 1948 take different values. In this research, we work with probability distributions of the number of
 1949 successes in a set of Bernoulli trials. These Bernoulli variables may or may not be associated.

1950 A probability distribution over the number of successes in n Bernoulli trials, where the
 1951 Bernoulli variables may be associated, could constitute a good model for the number of active
 1952 neurons in an ensemble of n neurons.

1953 **Binomial distribution**

The binomial distribution is a two parameter discrete probability distribution that can be thought of as a probability distribution the number of successes from n independent Bernoulli trials, each with the same probability of success. The parameters of the binomial distribution are n the number of trials, and $0 \leq p \leq 1$, the probability of success for each of these trials. A random variable with the binomial distribution can take values from $\{0, \dots, n\}$. The probability mass function of the distribution is

$$P(k; n, p) = \binom{n}{k} p^k (1-p)^{n-k} \quad (4.2)$$

1954 As a model for the activity of a neuronal ensemble, the main problem with the binomial
 1955 distribution is that it treats each neuron, represented as a Bernoulli trial, as independent. It is
 1956 well known that neurons are not independent, and that correlated behaviour between neurons
 1957 is vital for representing sensory information (Cohen and Maunsell, 2009). The binomial dis-
 1958 tribution falls short in this regard, but it is useful as performance benchmark when assessing
 1959 the performance of other models.

1960 **Beta-binomial distribution**

1961 The beta distribution is the conjugate distribution of the binomial distribution. The beta-
 1962 binomial distribution is the combination of the beta distribution and the binomial distribution,
 1963 in that the probability of success for the binomial distribution is sampled from the beta dis-
 1964 tribution. This allows the beta-binomial distribution to capture some over dispersion relative
 1965 to the binomial distribution.

The beta-binomial distribution is a three parameter distribution, n the number of Bernoulli trials, and $\alpha \in \mathbb{R}_{>0}$ and $\beta \in \mathbb{R}_{>0}$ the shape parameters of the beta distribution. The probability mass function for the beta-binomial distribution is

$$P(k; n, \alpha, \beta) = \binom{n}{k} \frac{B(k + \alpha, n - k + \beta)}{B(\alpha, \beta)} \quad (4.3)$$

1966 where $B(\alpha, \beta)$ is the beta function.

This probability distribution can be reparametrised in a number of ways. One of which defines new parameters π and ρ by

$$\pi = \frac{\alpha}{\alpha + \beta} \quad (4.4)$$

$$\rho = \frac{1}{\alpha + \beta + 1} \quad (4.5)$$

1967 This reparametrisation is useful because π acts as a location parameter analogous to the p
 1968 parameter of a binomial distribution. A value of $\rho > 0$ indicates over-dispersion relative to a
 1969 binomial distribution.

1970 As a model for the activity of a neuronal ensemble, the beta-binomial distribution is
 1971 more suitable than a binomial distribution because the over-dispersion of the beta-binomial
 1972 distribution can be used to model positive association between the neurons. An extreme
 1973 example of this over-dispersion/positive association can be seen in figure 4.1b. In this figure,
 1974 the neurons are positively associated and so tend to take the same value, consequently the
 1975 probability mass of the beta-binomial distribution builds up close to $k = 0$ and $k = n$. It is
 1976 worth noting that the location parameter for each distribution has the same value, $p = \pi =$
 1977 0.5.

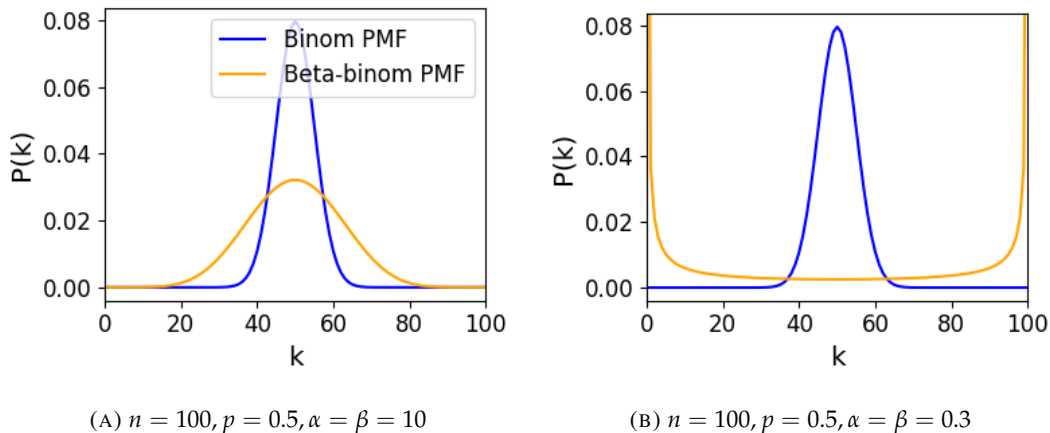


FIGURE 4.1: Figures showing the over-dispersion possible for a beta-binomial distribution relative to a binomial distribution. Parameters are shown in the captions.

1978 Conway-Maxwell-binomial distribution

1979 The Conway-Maxwell-binomial distribution (COMb distribution) is a three parameter generalisation of the binomial distribution that allows for over dispersion and under dispersion

relative to the binomial distribution. The parameters of the distribution are n the number of Bernoulli trials, and two shape parameters $0 \leq p \leq 1$, and $\nu \in \mathbb{R}$.

The probability mass function of the COMb distribution is

$$P(k; n, p, \nu) = \frac{1}{S(n, p, \nu)} \binom{n}{k}^{\nu} p^k (1-p)^{n-k} \quad (4.6)$$

where

$$S(n, p, \nu) = \sum_{j=0}^n \binom{n}{j}^{\nu} p^j (1-p)^{n-j} \quad (4.7)$$

The only difference between this PMF and the PMF for the standard binomial is the introduction of ν and the consequent introduction of the normalising function $S(n, p, \nu)$.

Indeed, if $\nu = 1$ the COMb distribution is identical to the binomial distribution with the same values for n and p . We can see in figure 4.2d that the KL-divergence $D_{KL}(P_{COMb}(n, p, \nu) || P_{Bin}(n, p)) = 0$ along the line where $\nu = 1$. The analytical expression for the divergence is

$$D_{KL}(P_{COMb}(k; n, p, \nu) || P_{Bin}(k; n, p)) = (\nu - 1) E_{P_{COMb}(k; n, p, \nu)} \left[\log \binom{n}{k} \right] \quad (4.8)$$

$$- \log S(n, p, \nu) \quad (4.9)$$

At $\nu = 1$, we have $S(n, p, 1)$ which is just the sum over the binomial PMF, so $S(n, p, 1) = 1$ and therefore $D_{KL}(P_{COMb}(n, p, \nu) || P_{Bin}(n, p)) = 0$.

If $\nu < 1$ the COMb distribution will exhibit over-dispersion relative to the binomial distribution. If $p = 0.5$ and $\nu = 0$ the COMb distribution is the discrete uniform distribution, and if $\nu < 0$ the mass of the COMb distribution will tend to build up near $k = 0$ and $k = n$. This over-dispersion represents positive association in the Bernoulli variables. An example of this over-dispersion can be seen in figure 4.2b.

If $\nu > 1$ the COMb distribution will exhibit under-dispersion relative to the binomial distribution. The larger the value of ν the more probability mass will build up at $n/2$ for even n , or at $\lfloor n/2 \rfloor$ and $\lceil n/2 \rceil$ for odd n . This under-dispersion represents negative association in the Bernoulli variables. An example of this under-dispersion can be seen in figure 4.2a.

It should be noted that the p parameter of the COMb distribution does not correspond to the mean of the distribution, as is the case for the binomial p parameter, and beta-binomial π parameter. That is, the COMb p parameter is not a location parameter. An illustration of this can be seen in figure 4.2c. This is because an interaction between the p and ν parameters skews the mean. There is no analytical expression for the mean of the COMb distribution.

ν	Relative dispersion	Association between neurons/variables
< 1	over	positive
1	none	none
> 1	under	negative

TABLE 4.2: Relative dispersion of the COMb distribution, and association between Bernoulli variables as represented by the value of the ν parameter.

2001 Since the COMb distribution has the potential to capture positive and negative associa-
 2002 tions between the neurons/Bernoulli variables, it should be an excellent candidate for mod-
 2003 elling the number of active neurons in a neuronal ensemble.

2004 We wrote a dedicated Python package to enable easy creation and fitting of COMb dis-
 2005 tribution objects. The format of the package imitates the format of other distribution objects
 2006 from the `scipy.stats` Python package. The COMb package can be found here:
 2007 https://github.com/thomasjdelaney/Conway_Maxwell_Binomial_Distribution

2008 4.3.6 Fitting

2009 We fitted binomial, beta-binomial, and Conway-Maxwell-binomial (COMb) distributions to
 2010 the neural activity in each of the overlapping windows covering each trial. To fit the distribu-
 2011 tions we minimised the appropriate negative log likelihood function using the data from the
 2012 window.

There is an analytical solution for maximum likelihood estimate of the binomial distribution's p parameter.

$$\hat{p} = \frac{1}{n} \sum_{i=1}^N k_i \quad (4.10)$$

2013 We minimised the negative log likelihood function of the beta-binomial distribution nu-
 2014 merically. We calculated the negative log likelihood for a sample directly, by taking the sum
 2015 of the log of the probability mass function for each value in the sample. We minimised the
 2016 negation of that function using the `minimise` function of the `scipy.optimize` Python
 2017 package.

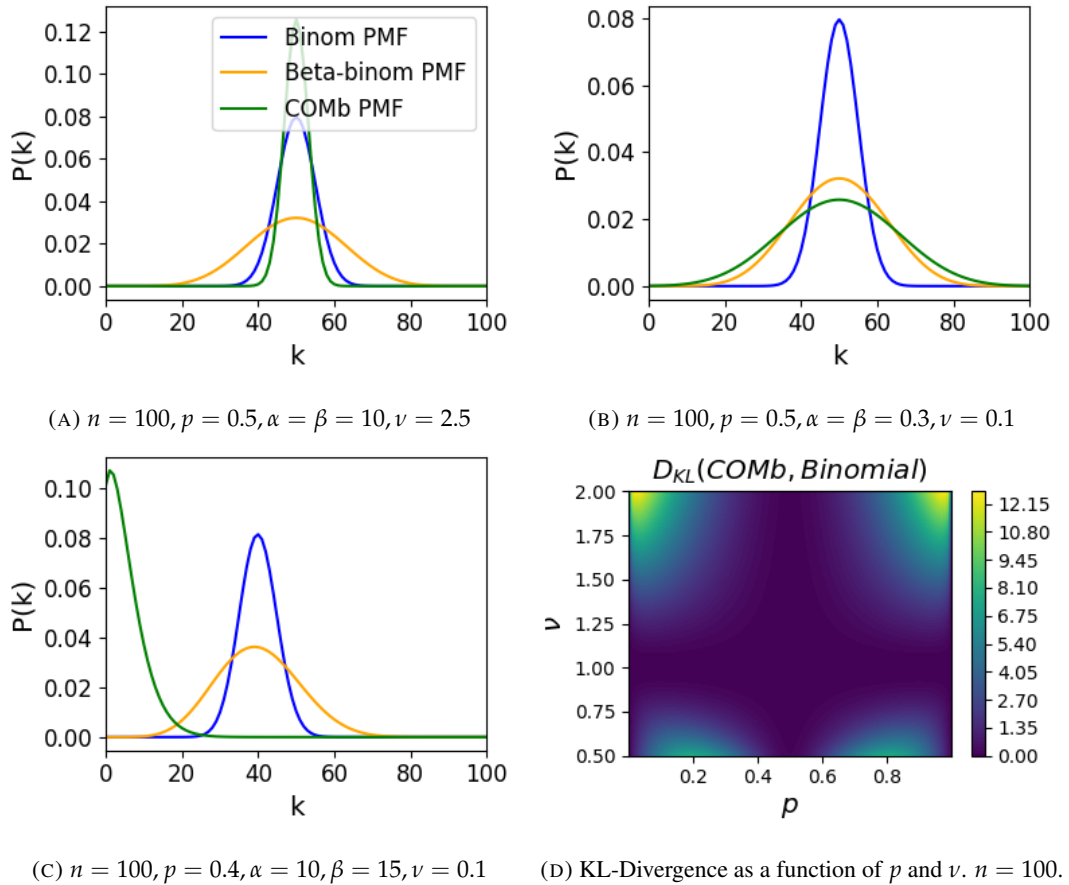


FIGURE 4.2: Figures showing (A) the under-dispersion and (B) over-dispersion permitted by the COMb distribution relative to a binomial distribution. (C) illustrates that the p parameter of the COMb distribution does not correspond to the mean of the distribution, as it does for the binomial and beta-binomial distributions. (D) shows a heatmap for the value of the Kullback-Liebler divergence between the COMb distribution and the standard binomial distribution with same value for n , as a function of p and ν . Parameters are shown in the captions.

The log likelihood function of the COMb distribution given some sample $\{k_1, \dots, k_N\}$ is

$$\ell(p, \nu | k_1, \dots, k_N) = N [n \log(1 - p) - \log S(n, p, \nu)] \quad (4.11)$$

$$+ \log \frac{p}{1 - p} \sum_{i=1}^N k_i \quad (4.12)$$

$$+ \nu \sum_{i=1}^N \log \binom{n}{k_i} \quad (4.13)$$

2018 We minimised the negation of this function using numerical methods. More specifically, we
2019 used the `minimise` function of the `scipy.optimize` Python package.

2020 **4.3.7 Goodness-of-fit**

2021 After fitting, we measured the goodness-of-fit of each model/distribution with their log like-
2022 lihood. We calculated this directly using the `logpmf` functions of the distribution objects in
2023 Python.

2024 **4.4 Results**

2025 We defined a neuron as *active* in a time bin if it fires at least one spike during the time interval
2026 covered by that bin. We measured the number of active neurons in the primary visual cortex
2027 of a mouse in 1ms bins across 160 trials of a moving bar visual stimulus. We then slid a
2028 100ms window across these 1ms bins taking measurements, and fitting distributions along
2029 the way. We did the same for neurons in the thalamus, hippocampus, striatum, and motor
2030 cortex. We repeated the analysis for 5ms time bins with 40 bin windows, and 10ms time bins
2031 with 40 bin windows.

2032 **4.4.1 Increases in mean number of active neurons and variance in number of
2033 active neurons at stimulus onset in some regions**

2034 We measured the average number of active neurons, and the variance of the number of active
2035 neurons in a 100ms sliding window starting 500ms before stimulus onset until 1000ms after
2036 stimulus onset. We found differences in the response across regions. There were no observed
2037 changes in response to the stimulus in the motor cortex or the striatum. The changes in the
2038 other regions are detailed below.

2039 **Primary visual cortex**

2040 We found a transient increase in both the average and variance of the number of active neu-
2041 rons at stimulus onset, followed by a fall to pre-stimulus levels, followed by another transient
2042 increase (see figure 4.3). The oscillation in both of these measurements appear to reflect the
2043 frequency of the stimulus (see Data section 4.2.1), and it is known that stimulus structure can
2044 influence response structure(Litwin-Kumar, Chacron, and Doiron, 2012). We see a similar
2045 but lower amplitude oscillation at the end of the stimulus presentation.

2046 **Hippocampus**

2047 In the hippocampus we observed a transient increase in the average number of active neurons
2048 and in the variance of the number of active neurons at stimulus onset (see figure 4.4). The
2049 increase lasted about 125ms, and the subsequent fall to baseline took the a similar amount of
2050 time.

2051 **Thalamus**

2052 In the thalamus we observed a transient increase in the both the average and variance of
2053 the number of active neurons on stimulus onset, followed by a fall to pre-stimulus levels,
2054 followed by a sustained increase until the stimulus presentation ends.

2055 As one you might expect for a visual stimulus, the change in the average number of active
2056 neurons was greatest in the primary visual cortex. In this region, this quantity doubled on
2057 stimulus onset. In contrast, in the hippocampus and the thalamus, the average number of
2058 active neurons only increased by a fraction of the unstimulated baseline value. The duration
2059 of the response in V1 and the hippocampus at stimulus onset was 300 – 400ms, but the
2060 response in the thalamus appeared to last for the duration of stimulus presentation. The V1
2061 also showed a change in the average number of active neurons at stimulus end. The change
2062 was similar to that observed at stimulus onset, but smaller in magnitude (see figures 4.3, 4.4,
2063 and 4.5)

2064 **4.4.2 Conway-Maxwell-binomial distribution is usually a better fit than bino-
2065 mial or beta-binomial**

2066 Since the Conway-Maxwell-binomial distribution has not been fitted to neuronal data before,
2067 it is not clear that it would be a better fit than the binomial or beta-binomial distributions.
2068 In order to find out which parametric distribution was the best fit for the largest proportion

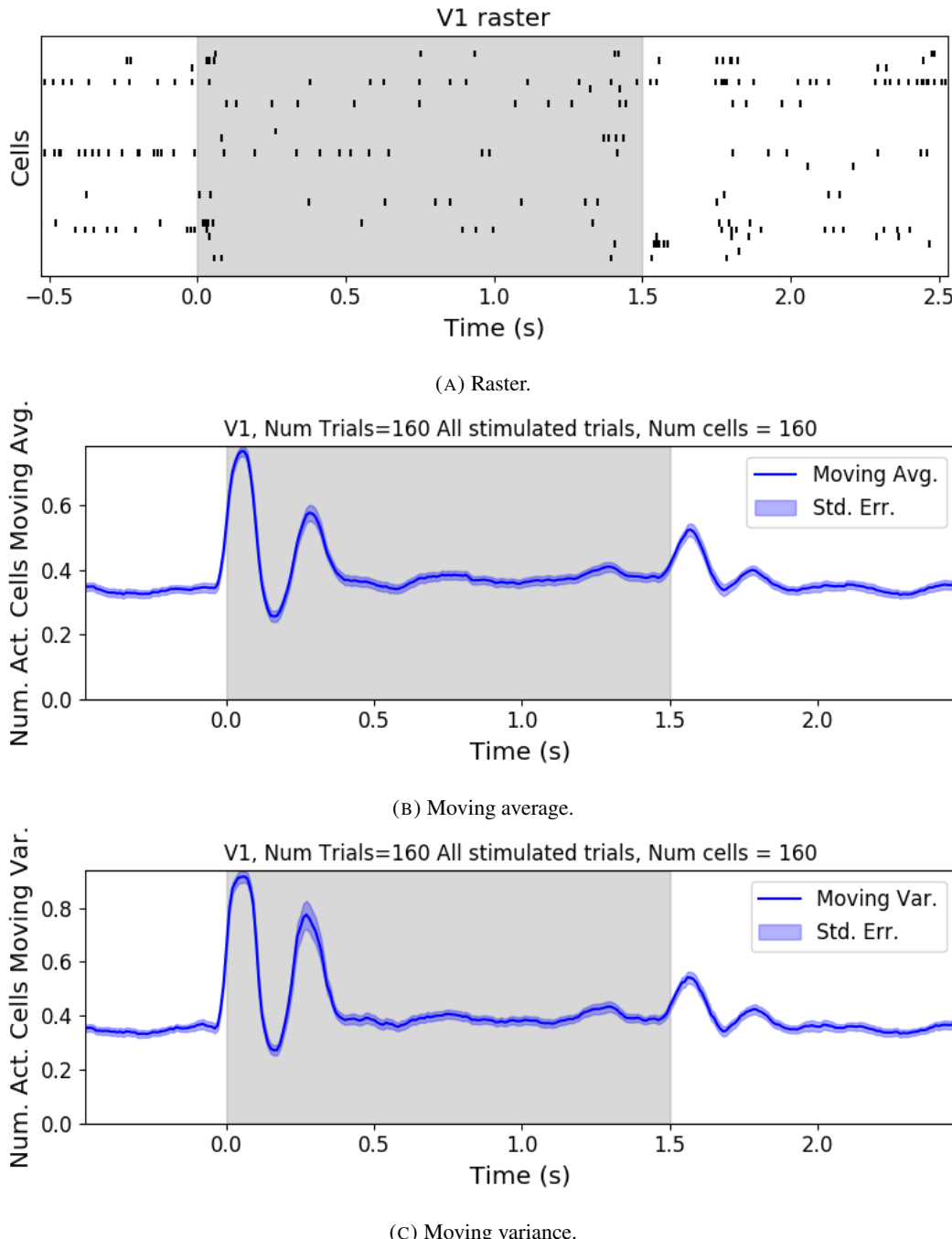


FIGURE 4.3: (A) Raster plot showing the spikes fired by 33 randomly chosen neurons in the primary visual cortex. (B-C) (B) average and (C) variance of the number of active neurons, measured using a sliding window 100ms wide, split into 100 bins. The midpoint of the time interval for each window is used as the timepoint (x-axis point) for the measurements using that window. The grey shaded area indicates the presence of a visual stimulus. The opaque line is an average across the 160 trials that included a visual stimulus of any kind. We can see a transient increase in the average number of active neurons and the variance of this number, followed by a fluctuation and another increase.

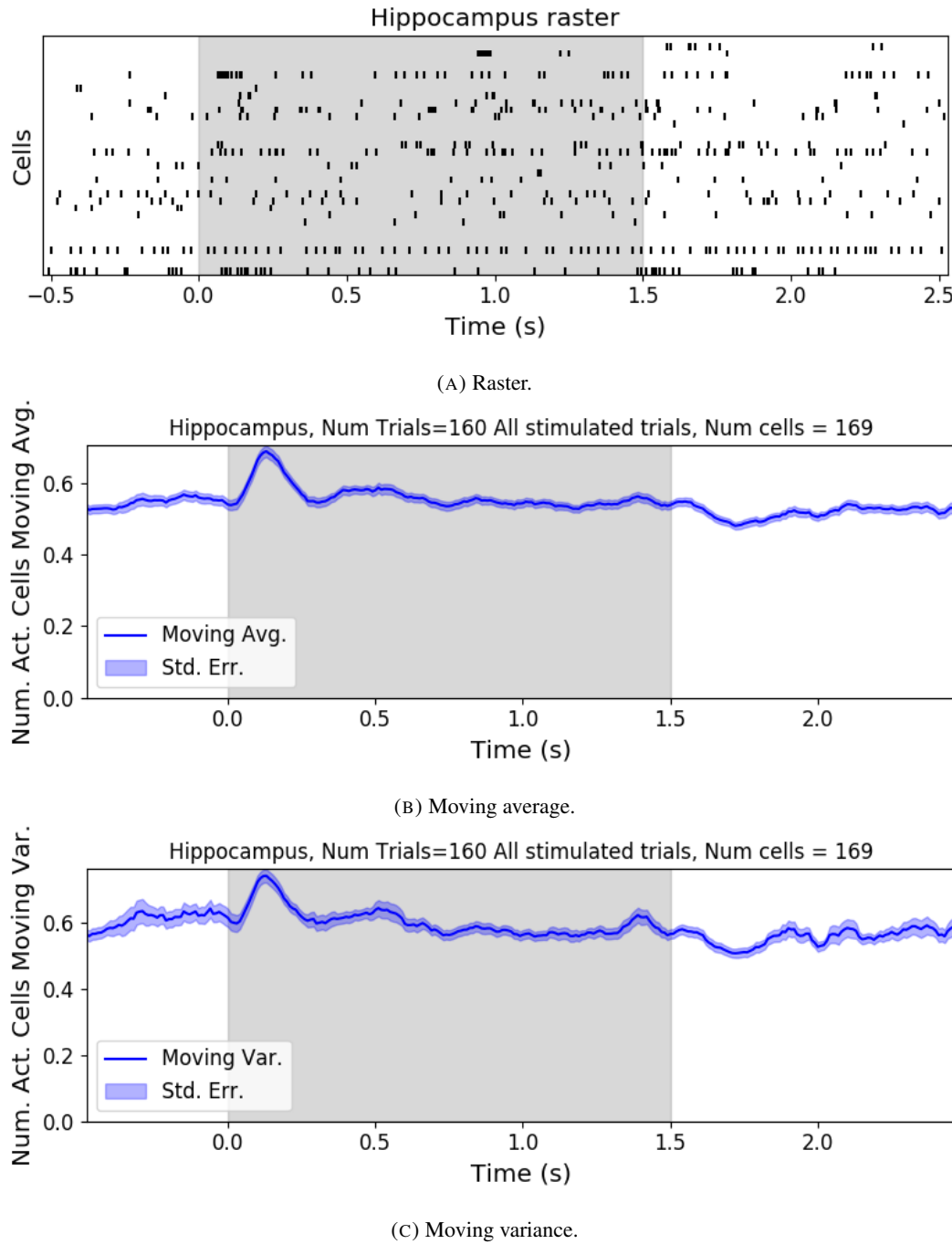


FIGURE 4.4: (A) Raster plot showing the spikes fired by 33 randomly chosen neurons in the hippocampus. (B-C) (B) average and (C) variance of the number of active neurons, measured using a sliding window 100ms wide, split into 100 bins. The midpoint of the time interval for each window is used as the timepoint (x-axis point) for the measurements using that window. The grey shaded area indicates the presence of a visual stimulus. The opaque line is an average across the 160 trials that included a visual stimulus of any kind. We can see a transient increase in the average number of active neurons and the variance of this number at stimulus onset.

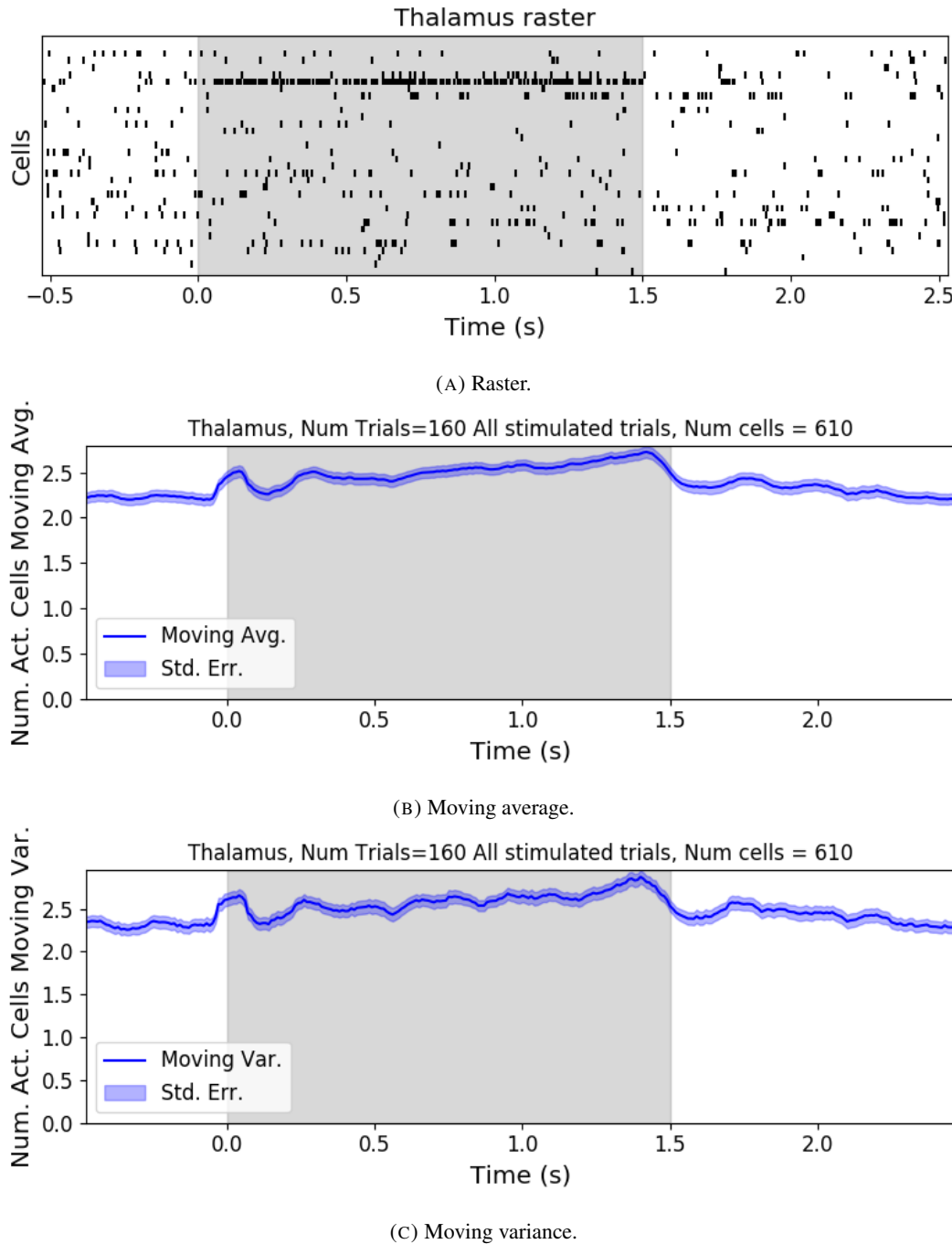
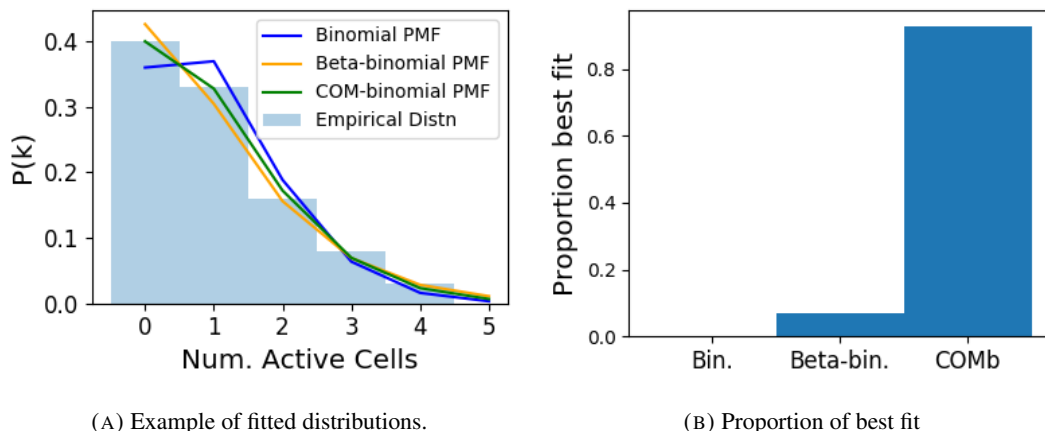


FIGURE 4.5: (A) Raster plot showing the spikes fired by 33 randomly chosen neurons in the thalamus. (B-C) (B) average and (C) variance of the number of active neurons, measured using a sliding window 100ms wide, split into 100 bins. The midpoint of the time interval for each window is used as the timepoint (x-axis point) for the measurements using that window. The grey shaded area indicates the presence of a visual stimulus. The opaque line is an average across the 160 trials that included a visual stimulus of any kind. We can see an immediate increase at stimulus onset, a subsequent fall, and another sustained increase until the stimulus presentation ends.

of our data, we fit a binomial, a beta-binomial, and a Conway-Maxwell-binomial (COMb) distribution to each window for each bin width, and each region. Then we assessed the goodness-of-fit of each distribution by calculating the log-likelihood of each fitted distribution using the associated sample. We measured the proportion of samples for which each distribution was the best fit, for each bin width value and each region.

We found that the COMb distribution was the best fit for most of the samples regardless of bin width or region. The bin width had an effect on the number of samples for which the COMb distribution was the best fit. The results are summarised in table 4.3. For a bin width of 1ms, the COMb distribution was the best fit for over 90% of samples, the beta-binomial distribution was the best fit for less than 10% of samples, and the binomial distribution was the best fit for less than 1% of samples, across regions. For 5ms bins, the COMb distribution was the best fit for 70 – 80% of samples, the beta-binomial distribution was the best fit for 20 – 30% of the samples, and again the binomial distribution was the best fit for less than 1% of samples, across regions. Finally, for 10ms bins, the COMb distribution was the best fit for 53 – 80% of samples, the beta-binomial distribution was the best fit for 20 – 47% of the samples, and the binomial distribution was the best fit for less than 0.1% of samples, across regions.



(A) Example of fitted distributions.

(B) Proportion of best fit

FIGURE 4.6: (A) An example of the binomial, beta-binomial, and Conway-Maxwell-binomial distributions fitted to a sample of neural activity. The Conway-Maxwell-binomial distribution is the best fit in this case. The histogram shows the empirical distribution of the sample. The probability mass function of each distribution is indicated by a different coloured line. (B) Across all samples in all trials, the proportion of samples for which each fitted distribution was the best fit. The Conway-Maxwell-binomial distribution was the best fit for 93% of the samples taken from V1 using a bin width of 1ms.

Bin Width (ms)	Binomial	Beta-binomial	COMb
1ms	< 1%	< 10%	> 90%
5ms	< 0.1%	20 – 30%	70 – 80%
10ms	< 0.1%	20 – 47%	53 – 80%

TABLE 4.3: Proportion of samples for which each distribution was the best fit, grouped by bin width. The COMb distribution is the best fit most of the time.

2086 **4.4.3 Conway-Maxwell-binomial distribution captures changes in association
2087 at stimulus onset**

2088 We fit a Conway-Maxwell-binomial (COMb) distribution to the number of active neurons in
2089 the 1ms time bins in a 100ms sliding window. We also measured the correlation coefficient
2090 between the spike counts of all possible pairs of neurons, and took the average of these
2091 coefficients. We did this for all the trials with a visual stimulus. We observed a reduction in
2092 the COMb distribution's ν parameter at stimulus onset from around 1 to between 0 and 1 (see
2093 figure 4.7a). A value of ν less than 1 indicates positive association between the neurons (see
2094 section 4.3.5). We might expect to see this positive association reflected in the correlation
2095 coefficients, but this is not the case. We see no change in the time series of average correlation
2096 measures at stimulus onset.

2097 This may be due to the very short time bin we used in this case. We know that using small
2098 time bins can artificially reduce correlation measurements (Cohen and Kohn, 2011). In this
2099 case, fitting the COMb distribution may be a useful way to measure association in a neuronal
2100 ensemble over very short timescales (< 10ms).

2101 **4.4.4 Replicating stimulus related quenching of neural variability**

2102 Churchland et al. (2010) inspected the effect of a stimulus on neural variability. One of the
2103 measures of neural variability that they employed was the Fano factor of the spike counts of
2104 individual cells (see section 4.3.4). They found a reduction in neural variability as measured
2105 by the Fano factor in various cortical areas in a macaque at the onset of various visual stimuli,
2106 or a juice reward (**churchland**).

2107 We measured the Fano factor of the spike count of each cell in each brain region, during
2108 each trial. We measured the mean and standard error of these Fano factors from 500ms
2109 before stimulus onset until 1000ms after stimulus end. For the primary visual cortex, we
2110 found a transient reduction in the Fano factor immediately after stimulus onset. We used
2111 a Mann-Whitney U test to check that the Fano factors measured in a window starting at

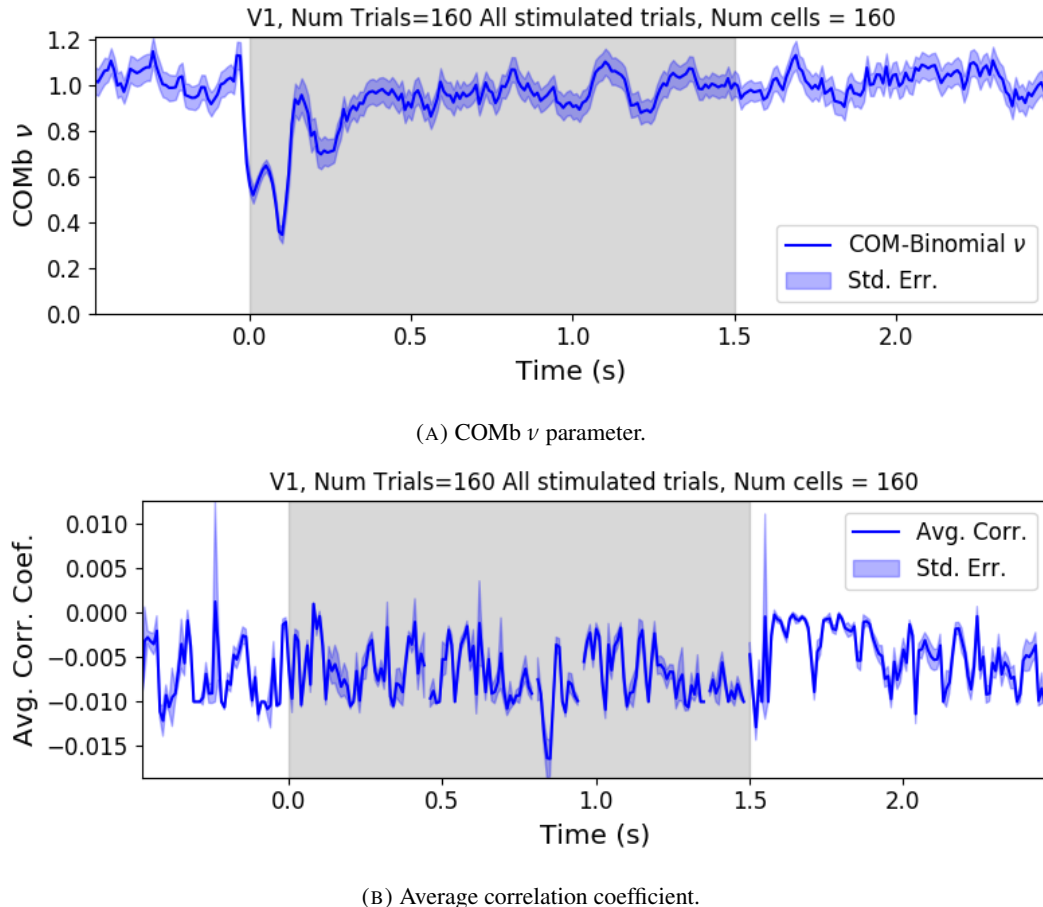


FIGURE 4.7: (A) We fit a Conway-Maxwell-binomial distribution to the number of active neurons in 1ms time bins of a 100ms sliding window. We did this for all trials with a visual stimulus and took the average across those trials. We see a transient drop in value for the distribution’s ν parameter at stimulus onset. This shows an increase in association between the neurons. (B) We measured the correlation coefficient between the spike counts of all possible pairs of neurons in the same sliding window. We took the average of those coefficients. We also did this for every visually stimulated trial, and took the average across trials. The increase in association is not reflected with an increase in average correlation.

stimulus onset and ending 100ms later were significantly lower than the factors measured in a window ending at stimulus onset ($p < 0.001$, see figure 4.8a). We did not get this statistically significant result in any other region.

Our findings agree with those of Churchland et al. for the primary visual cortex. However Churchland also found a reduction in the Fano factor in the dorsal premotor cortex (PMd) at stimulus onset. Our measurements from the mouse motor cortex show no change at stimulus onset (see figure 4.8b). This could indicate some difference in the functionality of the motor cortex in a macaque and the motor cortex of a mouse.

Similar to these findings in the Fano factor, we found a reduction in the ν parameter of the COMB distribution on stimulus onset in V1 (figure 4.7a) and in no other region from

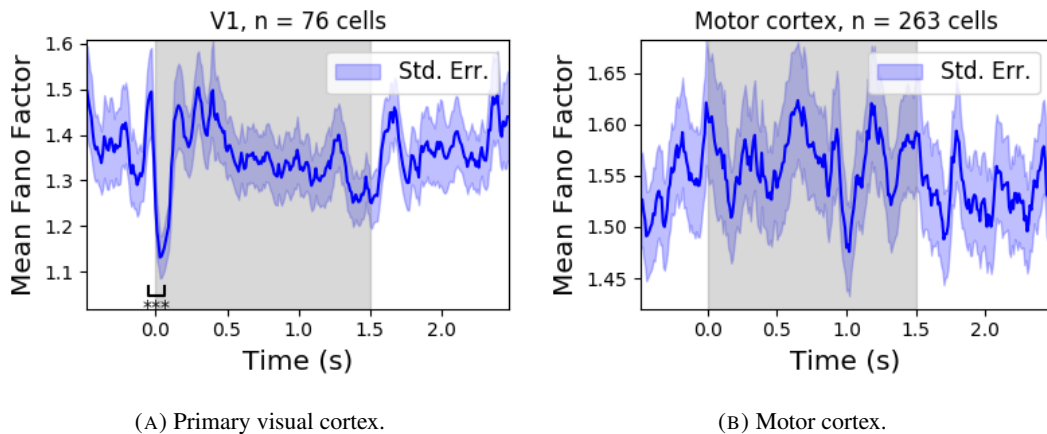


FIGURE 4.8: (A) The mean Fano factor of the spike counts of the cells in the primary visual cortex. Means were taken across cells first, then across trials. There was a significant decrease in the Fano factors immediately after stimulus onset. (B) The mean Fano factor of the spike counts of the cells in the motor cortex. No significant change in measurements at any point.

which we had data. Specifically, the ν parameter reduced from around 1, to between 1 and 0. This represents a change from no association between the neurons, to a positive association. It is possible that this positive association may be responsible for the reduction in the Fano factor.

4.5 Discussion

Our aim in this research was to develop a new statistical method for analysing the activity of a neuronal ensemble at very short timescales. We wanted our method to use information taken from the whole ensemble, but we also wanted the method to be quick and easy to implement. It is likely that analysis methods with these characteristics will become valuable as electrophysiological datasets include readings from more cells over longer time periods. In this case, we used the number of active, or spiking, neurons in a very short time bin ($< 10\text{ms}$) as a measure of ensemble activity.

First of all, we showed that there were changes in response that we could model at these very short time scales in some of the brain regions from which we had recordings. We observed changes in the average number of active neurons, and the variance of the number of active neurons in three different brain regions in response to visual stimuli. Since we know that correlated behaviour is associated with sensory perception (deCharms and Merzenich, 1996), we might hope to measure the pairwise correlations within the neuronal population in order to further investigate these responses. But, using such short time bins can produce

artificially small spike count correlation measurements (Cohen and Maunsell, 2009). Overcoming this limitation was one of our objectives for our new method. In order to do this, we abandoned the idea of measuring the correlations directly and embraced the concept of *association*. In order to quantify the association between neurons, we used the Conway-Maxwell-binomial distribution to model the number of active (spiking) neurons in an ensemble as a sum of possibly associated Bernoulli random variables.

We showed that the Conway-Maxwell-binomial distribution performed better than the more common options of the binomial and beta-binomial distributions. Furthermore, we showed that the positively associated behaviour between neurons in the primary visual cortex could be captured by fitting a Conway-Maxwell-binomial distribution, but was not captured by the more standard approach of measuring the spike count correlation. The associated behaviour could not be measured using spike count correlations, because of the very short bins required to capture short timescale behaviour.

We replicated a famous result from Churchland et al (2010) relating to the quenching of neural variability in cortical areas at stimulus onset, and in doing so, we established a correspondence between the association quantifying parameter of the Conway-Maxwell-binomial (COMb) distribution and the neural variability as measured by the Fano factor. We found a reduction in the ν parameter of the COMB distribution at stimulus onset, indicating a change from no association to positive association between neurons in V1. We found a corresponding reduction in the Fano factor of the individual cells in V1. The positive association between neurons induced by the stimulus would constrain the neurons to fire at the same time. The stimulus also induced a larger number of neurons to spike. These two actions combined could cause an increase in the firing rate of individual cells that is greater in magnitude than the increase in firing rate variability. If this is indeed the case, then the association as captured by the COMB distribution could be regarded as one of the ‘natural parameters’ of the ensemble response for short timescales. That is, a quantity that directly measures some aspect of the behaviour of the ensemble. In this case, it the correlated behaviour of the individual neurons is captured.

This work could be just a first step in creating analysis methods based on the Conway-Maxwell-binomial distribution, or similar statistical models. One way to extend the method would be to pair it up with the ‘Population Tracking model’ (O’Donnell et al., 2017). This model attempts to characterise the interaction between an ensemble and each member of the ensemble by quantifying the probability of spiking for a given a cell, given the number of active cells in the whole population. Combining this model with the COMB distribution

2175 would give us a model that could accurately fit the number of active neurons at any moment,
2176 and that gives a probability of firing for each cell, and therefore probabilities for full spiking
2177 patterns, without adding a huge number of parameters to fit.

2178 A more complex way to extend the model would be to fit a Conway-Maxwell-binomial
2179 distribution to data recorded from multiple brain regions simultaneously, with a different fit
2180 for each region, then to analyse the temporal relationship between the fitted parameters of
2181 each region. If we analysed the time series of the COMB distribution parameters from the
2182 different regions, looking at cross-correlations between regions, this may give some results
2183 relating to the timescales in which information is processed in different brain regions.

2184 **Chapter 5**

2185 **Studies with practical limitations &**
2186 **negative results**

2187 *Abstract*

2188 Here I will present some details on research topics that I started, but that unfortunately did not
2189 lead anywhere useful. There are two pieces of research, based on two papers. Each paper is
2190 related to the overall theme of my PhD of analysing and modelling behaviours of populations
2191 of neurons. The first part is based on a model of parallel spike trains including higher order
2192 interactions by Shimazaki et al (2012). The second part is based on a multiscale model for
2193 making inferences on hierarchical data.

2194 **5.1 Dynamic state space model of pairwise and higher order neu-**
2195 **ronal correlations**

2196 In their paper Shimazaki et al (2012) aimed to model spike trains from populations of neurons
2197 in parallel, with pairwise and higher order dynamic interactions between the trains. They
2198 modelled the spike trains as multi-variate binary processes using a log-linear model, and they
2199 extracted spike interaction parameters using a Bayesian filter/EM-algorithm. They developed
2200 a goodness-of-fit measure for the model to test if including these higher order correlations
2201 is necessary for an accurate model. Their measure was based on the Bayes factor but they
2202 also assessed the suitability of higher order models using the AIC and BIC. So the increase
2203 in the number of parameters associated with fitting higher order interactions was taken into
2204 account. They tested the performance of the model on synthetic data with known higher
2205 order correlations. They used the model to look for higher order correlations in data from
2206 awake behaving animals. They use the model to demonstrate dynamic appearance of higher
2207 order correlations in the monkey motor cortex (Shimazaki et al., 2012).

2208 We used the available Python repository to implement the model, and we successfully
2209 worked through the tutorial provided. But we found that the model did not scale well to
2210 larger populations. We attempted to fit the model to a population of 10 neurons and found we
2211 didn't manage to finish the process. Since, our goal was to find a model to scale to hundreds
2212 or thousands of neurons, we decided that this model was no longer worth pursuing.

2213 **5.2 A multiscale model for hierarchical data applied to**
2214 **neuronal data**

2215 In their paper Kolaczyk et al (2001) developed a framework for a modelling hierarchically
2216 aggregated data, and making inferences based on a model arising from this framework. They
2217 assumed that a hierarchical aggregation existed on the data in question, where each element at
2218 each level of the hierarchy had some associated measurements, an associated mean process,
2219 which was the expected value of these measurements. They also assumed that the measure-
2220 ments of each parent were equal to the sum of the measurements from all of its children.
2221 They showed that these assumptions gave rise to a relationship between parent and child
2222 measurements across all levels of the hierarchy, where the product of the likelihood of the
2223 parameters of the lowest level of the hierarchy can be expressed as products of conditional
2224 likelihoods of the elements of higher levels of the hierarchy (Kolaczyk and Huang, 2010).

2225 They gave examples of these expressions for measurements sampled from Gaussian dis-
2226 tributions, and Poisson distributions, and showed the definitions of the hierarchical param-
2227 eters which reparametrise the distribution of these data taking the hierarchy into account.
2228 They go on to suggest prior distributions for this multiscale model, and integrate these priors
2229 to give posterior distributions for the measurements from each element at each level in the hi-
2230 erarchy, and expressions for the MAP estimated parameters of each the associated processes
2231 (Kolaczyk and Huang, 2010).

2232 We implemented their model in Python by creating some synthetic data from Poisson
2233 distributions, and defining a hierarchy by agglomerating these data. We calculated the MAP
2234 estimates using our knowledge of the hierarchy, and using the expressions given in the paper.
2235 We found that the MAP estimates were far less accurate than would be achieved by simply
2236 ignoring the hierarchy during estimation, and using a maximum likelihood approach. After
2237 that, we decided to move on.

2238 **Chapter 6**

2239 **Discussion**

2240 Ideas (not in order):

2241 • Calcium imaging limitations (spike inference not always possible)

2242 • Judging by Greenberg biophysical modelling is the way to go.

2243 • our fluorescence model could be useful in a number of situations.

2244 • Applied new network science to new electrophysiological dataset.

2245 • Abandon calcium

2246 • Multi region calcium imaging dataset would be useful?

2247 • Results might be intuitive, but are new nonetheless (as far as I know)

2248 • Potential for more network science applications?

2249 • Applied the COMB distribution to neuronal data for the first time.

2250 • captures correlated behaviour by quantifying *association*.

2251 • Abandon correlations.

2252 • coupling with existing models could yield some nice models.

2253 • More statistical invention could be useful.

2254 Bibliography

- 2255 Allen, William E. et al. (2019). “Thirst regulates motivated behavior through modulation of
 2256 brainwide neural population dynamics”. In: *Science* 364.6437. ISSN: 0036-8075. DOI:
 2257 [10.1126/science.aav3932](https://doi.org/10.1126/science.aav3932). eprint: <https://science.sciencemag.org/content/364/6437/eaav3932.full.pdf>. URL: <https://science.sciencemag.org/content/364/6437/eaav3932>.
- 2258 Baadel, S., F. Thabtah, and J. Lu (2016). “Overlapping clustering: A review”. In: *2016 SAI Computing Conference (SAI)*, pp. 233–237. DOI: [10.1109/SAI.2016.7555988](https://doi.org/10.1109/SAI.2016.7555988).
- 2259 Baldassano, Christopher et al. (2017). “Discovering Event Structure in Continuous Narrative Perception and Memory”. In: *Neuron* 95.3, 709 –721.e5. ISSN: 0896-6273. DOI: <https://doi.org/10.1016/j.neuron.2017.06.041>. URL: <http://www.sciencedirect.com/science/article/pii/S0896627317305937>.
- 2260 Bartol, Thomas M. et al. (2015). “Computational reconstitution of spine calcium transients from individual proteins”. In: *Frontiers in Synaptic Neuroscience* 7, p. 17. ISSN: 1663-3563. DOI: [10.3389/fnsyn.2015.00017](https://doi.org/10.3389/fnsyn.2015.00017). URL: <https://www.frontiersin.org/article/10.3389/fnsyn.2015.00017>.
- 2261 Berens, Philipp et al. (May 2018). “Community-based benchmarking improves spike rate inference from two-photon calcium imaging data”. In: *PLOS Computational Biology* 14.5, pp. 1–13. DOI: [10.1371/journal.pcbi.1006157](https://doi.org/10.1371/journal.pcbi.1006157). URL: <https://doi.org/10.1371/journal.pcbi.1006157>.
- 2262 Bezanson, Jeff et al. (Sept. 2012). “Julia: A Fast Dynamic Language for Technical Computing”. In: *MIT*.
- 2263 Buccino, Alessio P. et al. (2019). “SpikeInterface, a unified framework for spike sorting”. In: *bioRxiv*. DOI: [10.1101/796599](https://doi.org/10.1101/796599). eprint: <https://www.biorxiv.org/content/early/2019/10/07/796599.full.pdf>. URL: <https://www.biorxiv.org/content/early/2019/10/07/796599>.
- 2264 Chen, Tsai-Wen et al. (July 2013). “Ultrasensitive fluorescent proteins for imaging neuronal activity”. In: *Nature* 499, 295–300. DOI: [10.1038/nature12354](https://doi.org/10.1038/nature12354). URL: <https://doi.org/10.1038/nature12354>.

- 2283 Churchland, Mark M. et al. (2010). “Stimulus onset quenches neural variability: a widespread
2284 cortical phenomenon”. eng. In: *Nature neuroscience* 13.3. 20173745[pmid], pp. 369–378.
2285 ISSN: 1546-1726. DOI: [10.1038/nrn.2501](https://doi.org/10.1038/nrn.2501). URL: <https://pubmed.ncbi.nlm.nih.gov/20173745>.
- 2287 Cohen, Marlene R. and Adam Kohn (2011). “Measuring and interpreting neuronal correla-
2288 tions”. In: *Nature Neuroscience* 14.7, pp. 811–819. ISSN: 1546-1726. DOI: [10.1038/nrn.2842](https://doi.org/10.1038/nrn.2842). URL: <https://doi.org/10.1038/nrn.2842>.
- 2290 Cohen, Marlene R. and John H. R. Maunsell (2009). “Attention improves performance pri-
2291 marily by reducing interneuronal correlations”. eng. In: *Nature neuroscience* 12.12. 19915566[pmid],
2292 pp. 1594–1600. ISSN: 1546-1726. DOI: [10.1038/nrn.2439](https://doi.org/10.1038/nrn.2439). URL: <https://pubmed.ncbi.nlm.nih.gov/19915566>.
- 2294 Dana, Hod et al. (Sept. 2014). “Thy1-GCaMP6 Transgenic Mice for Neuronal Population
2295 Imaging In Vivo”. In: *PloS one* 9, e108697. DOI: [10.1371/journal.pone.0108697](https://doi.org/10.1371/journal.pone.0108697).
- 2297 deCharms, R. Christopher and Michael M. Merzenich (1996). “Primary cortical represen-
2298 tation of sounds by the coordination of action-potential timing”. In: *Nature* 381.6583,
2299 pp. 610–613. ISSN: 1476-4687. DOI: [10.1038/381610a0](https://doi.org/10.1038/381610a0). URL: <https://doi.org/10.1038/381610a0>.
- 2301 Deneux, Thomas et al. (July 2016). “Accurate spike estimation from noisy calcium signals
2302 for ultrafast three-dimensional imaging of large neuronal populations in vivo”. In: *Nature
2303 Communications* 7.1. DOI: [10.1038/ncomms12190](https://doi.org/10.1038/ncomms12190). URL: <https://doi.org/10.1038/ncomms12190>.
- 2305 Faas, G. C. et al. (Mar. 2011). “Calmodulin as a direct detector of Ca²⁺ signals”. In: *Nature
2306 neuroscience* 14.3, pp. 301–304. DOI: [10.1038/nrn.2746](https://doi.org/10.1038/nrn.2746). URL: <https://doi.org/10.1038/nrn.2746>.
- 2308 Fiala, John C. and Kristen M. Harris (1999). *Dendrite Structure*.
- 2309 Flach, Boris (Sept. 2013). “A Class of Random Fields on Complete Graphs with Tractable
2310 Partition Function”. In: *IEEE transactions on pattern analysis and machine intelligence*
2311 35, pp. 2304–6. DOI: [10.1109/TPAMI.2013.99](https://doi.org/10.1109/TPAMI.2013.99).
- 2312 Forney, G. D. (1973). “The viterbi algorithm”. In: *Proceedings of the IEEE* 61.3, pp. 268–
2313 278. ISSN: 1558-2256. DOI: [10.1109/PROC.1973.9030](https://doi.org/10.1109/PROC.1973.9030).
- 2314 Fosdick, Bailey et al. (Aug. 2016). “Configuring Random Graph Models with Fixed Degree
2315 Sequences”. In: *SIAM Review* 60. DOI: [10.1137/16M1087175](https://doi.org/10.1137/16M1087175).

- 2316 Friedrich, Johannes and Liam Paninski (2016). “Fast Active Set Methods for Online Spike
2317 Inference from Calcium Imaging”. In: *Advances in Neural Information Processing Systems* 29. Ed. by D. D. Lee et al. Curran Associates, Inc., pp. 1984–1992. URL: <http://papers.nips.cc/paper/6505-fast-active-set-methods-for-online-spike-inference-from-calcium-imaging.pdf>.
- 2318
- 2319
- 2320
- 2321 Ganmor, Elad, Ronen Segev, and Elad Schneidman (2011). “Sparse low-order interaction
2322 network underlies a highly correlated and learnable neural population code”. In: *Proceedings of the National Academy of Sciences* 108.23, pp. 9679–9684. ISSN: 0027-8424. DOI:
2323 [10.1073/pnas.1019641108](https://doi.org/10.1073/pnas.1019641108). eprint: <https://www.pnas.org/content/108/23/9679.full.pdf>. URL: <https://www.pnas.org/content/108/23/9679>.
- 2324
- 2325
- 2326
- 2327 Girard, P., J. M. Hupé, and J. Bullier (2001). “Feedforward and Feedback Connections Be-
2328 tween Areas V1 and V2 of the Monkey Have Similar Rapid Conduction Velocities”. In:
2329 *Journal of Neurophysiology* 85.3. PMID: 11248002, pp. 1328–1331. DOI: [10.1152/jn.2001.85.3.1328](https://doi.org/10.1152/jn.2001.85.3.1328). eprint: <https://doi.org/10.1152/jn.2001.85.3.1328>. URL: <https://doi.org/10.1152/jn.2001.85.3.1328>.
- 2330
- 2331
- 2332 Greenberg, David et al. (Nov. 2018). “Accurate action potential inference from a calcium
2333 sensor protein through biophysical modeling.” in: DOI: [10.1101/479055](https://doi.org/10.1101/479055).
- 2334 Gründemann, Jan et al. (2019). “Amygdala ensembles encode behavioral states”. In: *Science*
2335 364.6437. ISSN: 0036-8075. DOI: [10.1126/science.aav8736](https://doi.org/10.1126/science.aav8736). eprint: <https://science.sciencemag.org/content/364/6437/eaav8736.full.pdf>. URL: <https://science.sciencemag.org/content/364/6437/eaav8736>.
- 2336
- 2337
- 2338
- 2339 Hodgkin, A. L. and A. F. Huxley (1939). “Action Potentials Recorded from Inside a Nerve Fi-
2340 bre”. In: *Nature* 144.3651, pp. 710–711. ISSN: 1476-4687. DOI: [10.1038/144710a0](https://doi.org/10.1038/144710a0).
2341 URL: <https://doi.org/10.1038/144710a0>.
- 2342 Humphries, Mark et al. (Jan. 2019). “Spectral rejection for testing hypotheses of structure in
2343 networks”. In:
- 2344 Humphries, Mark D. (2011). “Spike-Train Communities: Finding Groups of Similar Spike
2345 Trains”. In: *Journal of Neuroscience* 31.6, pp. 2321–2336. ISSN: 0270-6474. DOI: [10.1523/JNEUROSCI.2853-10.2011](https://doi.org/10.1523/JNEUROSCI.2853-10.2011). eprint: <https://www.jneurosci.org/content/31/6/2321.full.pdf>. URL: <https://www.jneurosci.org/content/31/6/2321>.
- 2346
- 2347
- 2348

- 2349 Jun, James J. et al. (2017). “Fully integrated silicon probes for high-density recording of
2350 neural activity”. In: *Nature* 551.7679, pp. 232–236. ISSN: 1476-4687. DOI: [10.1038/nature24636](https://doi.org/10.1038/nature24636). URL: <https://doi.org/10.1038/nature24636>.
- 2352 Kadane, Joseph B. (June 2016). “Sums of Possibly Associated Bernoulli Variables: The
2353 Conway–Maxwell-Binomial Distribution”. In: *Bayesian Anal.* 11.2, pp. 403–420. DOI:
2354 [10.1214/15-BA955](https://doi.org/10.1214/15-BA955). URL: <https://doi.org/10.1214/15-BA955>.
- 2355 Kilhoffer, Marie-Claude et al. (Sept. 1992). “Use of Engineered Proteins With Internal Tryp-
2356 tophean Reporter Groups and Perturbation Techniques to Probe the Mechanism of Ligand-
2357 Protein Interactions: Investigation of the Mechanism of Calcium Binding to Calmod-
2358 ulin”. In: *Biochemistry* 31.34, pp. 8098–8106. DOI: [10.1021/bi00149a046](https://doi.org/10.1021/bi00149a046). URL:
2359 <https://doi.org/10.1021/bi00149a046>.
- 2360 Koch, Christoff (1999). *Biophysics of Computation: Information Processing in Single Neu-*
2361 *rons*. Oxford University Press. ISBN: ISBN 0-19-510491-9.
- 2362 Kolaczyk, Eric and Haiying Huang (Sept. 2010). “Multiscale Statistical Models for Hier-
2363 archical Spatial Aggregation”. In: *Geographical Analysis* 33, pp. 95 –118. DOI: [10.1111/j.1538-4632.2001.tb00439.x](https://doi.org/10.1111/j.1538-4632.2001.tb00439.x).
- 2365 Lee, Suk-HO et al. (July 2000). “Differences in Ca2+ buffering properties between excitatory
2366 and inhibitory hippocampal neurons from the rat”. In: *The Journal of Physiology* 525.
2367 DOI: [10.1111/j.1469-7793.2000.t01-3-00405.x](https://doi.org/10.1111/j.1469-7793.2000.t01-3-00405.x).
- 2368 Litwin-Kumar, Ashok, Maurice Chacron, and Brent Doiron (Sept. 2012). “The Spatial Struc-
2369 ture of Stimuli Shapes the Timescale of Correlations in Population Spiking Activity”.
2370 In: *PLoS computational biology* 8, e1002667. DOI: [10.1371/journal.pcbi.1002667](https://doi.org/10.1371/journal.pcbi.1002667).
- 2372 Maravall, M et al. (May 2000). “Estimating intracellular calcium concentrations and buffer-
2373 ing without wavelength ratioing”. In: *Biophysical Journal* 78.5, pp. 2655–2667. DOI:
2374 [10.1016/S0006-3495\(00\)76809-3](https://doi.org/10.1016/S0006-3495(00)76809-3). URL: [https://doi.org/10.1016/S0006-3495\(00\)76809-3](https://doi.org/10.1016/S0006-3495(00)76809-3).
- 2376 Maugis, Pa (Jan. 2014). “Event Conditional Correlation: Or How Non-Linear Linear Depen-
2377 dence Can Be”. In:
- 2378 Meilă, Marina (2007). “Comparing clusterings—an information based distance”. In: *Journal*
2379 *of Multivariate Analysis* 98.5, pp. 873 –895. ISSN: 0047-259X. DOI: <https://doi.org/10.1016/j.jmva.2006.11.013>. URL: <http://www.sciencedirect.com/science/article/pii/S0047259X06002016>.

- 2382 Murray, John D. et al. (2014). “A hierarchy of intrinsic timescales across primate cortex”.
2383 In: *Nature Neuroscience* 17.12, pp. 1661–1663. ISSN: 1546-1726. DOI: [10.1038/nn.3862](https://doi.org/10.1038/nn.3862). URL: <https://doi.org/10.1038/nn.3862>.
- 2385 Neher, E. and G. J. Augustine (1992). “Calcium gradients and buffers in bovine chromaffin
2386 cells”. eng. In: *The Journal of physiology* 450. 1331424[pmid], pp. 273–301. ISSN: 0022-
2387 3751. DOI: [10.1113/jphysiol.1992.sp019127](https://doi.org/10.1113/jphysiol.1992.sp019127). URL: <https://pubmed.ncbi.nlm.nih.gov/1331424>.
- 2389 O’Donnell, Cian et al. (Jan. 2017). “The population tracking model: a simple, scalable statis-
2390 tical model for neural population data”. English. In: *Neural Computation* 29.1, pp. 50–
2391 93. ISSN: 0899-7667. DOI: [10.1162/NECO_a_00910](https://doi.org/10.1162/NECO_a_00910).
- 2392 Ouzounov, Dimitre G. et al. (2017). “In vivo three-photon imaging of activity of GCaMP6-
2393 labeled neurons deep in intact mouse brain”. eng. In: *Nature methods* 14.4. 28218900[pmid],
2394 pp. 388–390. ISSN: 1548-7105. DOI: [10.1038/nmeth.4183](https://doi.org/10.1038/nmeth.4183). URL: <https://pubmed.ncbi.nlm.nih.gov/28218900>.
- 2396 Patterson, Carolyn A. et al. (2014). “Similar adaptation effects in primary visual cortex and
2397 area MT of the macaque monkey under matched stimulus conditions”. In: *Journal of Neu-
2398 rophysiology* 111.6. PMID: 24371295, pp. 1203–1213. DOI: [10.1152/jn.00030.2013](https://doi.org/10.1152/jn.00030.2013). eprint: <https://doi.org/10.1152/jn.00030.2013>. URL: <https://doi.org/10.1152/jn.00030.2013>.
- 2401 Peron, Simon P. et al. (2015). “A Cellular Resolution Map of Barrel Cortex Activity during
2402 Tactile Behavior”. In: *Neuron* 86.3, pp. 783–799. ISSN: 0896-6273. DOI: [10.1016/j.neuron.2015.03.027](https://doi.org/10.1016/j.neuron.2015.03.027). URL: <https://doi.org/10.1016/j.neuron.2015.03.027>.
- 2405 Pnevmatikakis, E.A. et al. (Jan. 2016). “Simultaneous Denoising, Deconvolution, and Demix-
2406 ing of Calcium Imaging Data”. In: *Neuron* 89.2, pp. 285–299. DOI: [10.1016/j.neuron.2015.11.037](https://doi.org/10.1016/j.neuron.2015.11.037). URL: <https://doi.org/10.1016/j.neuron.2015.11.037>.
- 2409 Pnevmatikakis, Eftychios et al. (Nov. 2013). “Bayesian spike inference from calcium imaging
2410 data”. In: *Conference Record - Asilomar Conference on Signals, Systems and Computers*.
2411 DOI: [10.1109/ACSSC.2013.6810293](https://doi.org/10.1109/ACSSC.2013.6810293).
- 2412 Pnevmatikakis, Eftychios et al. (Sept. 2014). “A structured matrix factorization framework
2413 for large scale calcium imaging data analysis”. In:
- 2414 Schneidman, Elad et al. (2006). “Weak pairwise correlations imply strongly correlated net-
2415 work states in a neural population”. eng. In: *Nature* 440.7087. 16625187[pmid], pp. 1007–

- 2416 1012. ISSN: 1476-4687. DOI: [10.1038/nature04701](https://doi.org/10.1038/nature04701). URL: <https://pubmed.ncbi.nlm.nih.gov/16625187>.
- 2417
- 2418 Shannon, C. E. (1948). "A Mathematical Theory of Communication". In: *Bell System Technical Journal* 27.3, pp. 379–423. DOI: [10.1002/j.1538-7305.1948.tb01338.x](https://doi.org/10.1002/j.1538-7305.1948.tb01338.x).
2419 eprint: <https://onlinelibrary.wiley.com/doi/pdf/10.1002/j.1538-7305.1948.tb01338.x>. URL: <https://onlinelibrary.wiley.com/doi/abs/10.1002/j.1538-7305.1948.tb01338.x>.
- 2420
- 2421
- 2422
- 2423 Shimazaki, Hideaki et al. (2012). "State-space analysis of time-varying higher-order spike correlation for multiple neural spike train data". eng. In: *PLoS computational biology* 8.3. 22412358[pmid], e1002385–e1002385. ISSN: 1553-7358. DOI: [10.1371/journal.pcbi.1002385](https://doi.org/10.1371/journal.pcbi.1002385). URL: <https://pubmed.ncbi.nlm.nih.gov/22412358>.
- 2424
- 2425
- 2426
- 2427 Staude, Benjamin, Sonja Grün, and Stefan Rotter (2010). "Higher-Order Correlations and Cumulants". In: *Analysis of Parallel Spike Trains*. Ed. by Sonja Grün and Stefan Rotter. Boston, MA: Springer US, pp. 253–280. ISBN: 978-1-4419-5675-0. DOI: [10.1007/978-1-4419-5675-0_12](https://doi.org/10.1007/978-1-4419-5675-0_12). URL: https://doi.org/10.1007/978-1-4419-5675-0_12.
- 2428
- 2429
- 2430
- 2431
- 2432 Stein, Astrid von and Johannes Sarnthein (2000). "Different frequencies for different scales of cortical integration: from local gamma to long range alpha/theta synchronization". In: *International Journal of Psychophysiology* 38.3, pp. 301 –313. ISSN: 0167-8760. DOI: [https://doi.org/10.1016/S0167-8760\(00\)00172-0](https://doi.org/10.1016/S0167-8760(00)00172-0). URL: <http://www.sciencedirect.com/science/article/pii/S0167876000001720>.
- 2433
- 2434
- 2435
- 2436
- 2437 Steinmetz, Nick, Matteo Carandini, and Kenneth D. Harris (2019). "Single Phase3" and "Dual Phase3" Neuropixels Datasets. DOI: [10.6084/m9.figshare.7666892.v2](https://doi.org/10.6084/m9.figshare.7666892.v2). URL: https://figshare.com/articles/dataset/_Single_Phase3_Neuropixels_Dataset/7666892/2.
- 2438
- 2439
- 2440
- 2441 Steinmetz, Nick et al. (Mar. 2019). "Eight-probe Neuropixels recordings during spontaneous behaviors". In: DOI: [10.25378/janelia.7739750.v4](https://doi.org/10.25378/janelia.7739750.v4). URL: https://janelia.figshare.com/articles/Eight-probe_Neuropixels_recordings_during_spontaneous_behaviors/7739750.
- 2442
- 2443
- 2444
- 2445 Stringer, Carsen et al. (2019). "Spontaneous behaviors drive multidimensional, brainwide activity". In: *Science* 364.6437. ISSN: 0036-8075. DOI: [10.1126/science.aav7893](https://doi.org/10.1126/science.aav7893).
2446 eprint: <https://science.scienmag.org/content/364/6437/eaav7893.full.pdf>. URL: <https://science.scienmag.org/content/364/6437/eaav7893>.
- 2447
- 2448
- 2449

- 2450 Tada, Mayumi et al. (2014). “A highly sensitive fluorescent indicator dye for calcium imaging
2451 of neural activity in vitro and in vivo”. In: *European Journal of Neuroscience* 39.11,
2452 pp. 1720–1728. DOI: [10.1111/ejn.12476](https://doi.org/10.1111/ejn.12476). eprint: <https://onlinelibrary.wiley.com/doi/pdf/10.1111/ejn.12476>. URL: <https://onlinelibrary.wiley.com/doi/abs/10.1111/ejn.12476>.
- 2455 Tian, Lin et al. (2009). “Imaging neural activity in worms, flies and mice with improved
2456 GCaMP calcium indicators”. eng. In: *Nature methods* 6.12. 19898485[pmid], pp. 875–
2457 881. ISSN: 1548-7105. DOI: [10.1038/nmeth.1398](https://doi.org/10.1038/nmeth.1398). URL: <https://pubmed.ncbi.nlm.nih.gov/19898485>.
- 2459 Tkačik, Gašper et al. (2014). “Searching for collective behavior in a large network of sensory neurons”. eng. In: *PLoS computational biology* 10.1. 24391485[pmid], e1003408–
2460 e1003408. ISSN: 1553-7358. DOI: [10.1371/journal.pcbi.1003408](https://doi.org/10.1371/journal.pcbi.1003408). URL:
2462 <https://pubmed.ncbi.nlm.nih.gov/24391485>.
- 2463 Treves, Alessandro and Stefano Panzeri (1995). “The Upward Bias in Measures of Information Derived from Limited Data Samples”. In: *Neural Computation* 7.2, pp. 399–407.
2464 DOI: [10.1162/neco.1995.7.2.399](https://doi.org/10.1162/neco.1995.7.2.399). eprint: <https://doi.org/10.1162/neco.1995.7.2.399>. URL: <https://doi.org/10.1162/neco.1995.7.2.399>.
- 2468 Vinh, Nguyen Xuan, Julien Epps, and James Bailey (Dec. 2010). “Information Theoretic
2469 Measures for Clusterings Comparison: Variants, Properties, Normalization and Correc-
2470 tion for Chance”. In: *J. Mach. Learn. Res.* 11, 2837–2854. ISSN: 1532-4435.
- 2471 Vogelstein, Joshua T. et al. (Oct. 2010). “Fast nonnegative deconvolution for spike train infer-
2472 ence from population calcium imaging”. In: *Journal of neurophysiology* 104.6, 295–300.
2473 DOI: [10.1152/jn.01073.2009](https://doi.org/10.1152/jn.01073.2009). URL: <https://dx.doi.org/10.1152%2Fjn.01073.2009>.
- 2475 Wierzynski, ”Casimir M. et al. (2009). “”State-Dependent Spike-Timing Relationships be-
2476 tween Hippocampal and Prefrontal Circuits during Sleep””. In: ”*Neuron*” ”61.””4”, ”587
2477 –596”. ISSN: ”0896-6273”. DOI: <https://doi.org/10.1016/j.neuron.2009.01.011>. URL: <http://www.sciencedirect.com/science/article/pii/S0896627309000786>.
- 2480 Zariwala, Hatim A. et al. (2012). “A Cre-dependent GCaMP3 reporter mouse for neuronal
2481 imaging in vivo”. eng. In: *The Journal of neuroscience : the official journal of the Society
2482 for Neuroscience* 32.9. 22378886[pmid], pp. 3131–3141. ISSN: 1529-2401. DOI: [10.1529/jneurosci.0532-12.2012](https://doi.org/10.1529/jneurosci.0532-12.2012).

- 2483 1523 / JNEUROSCI . 44 69–11 . 2012 . URL: <https://pubmed.ncbi.nlm.nih.gov/22378886>.
- 2484 Zou, Hui and Trevor Hastie (2005). “Regularization and variable selection via the Elastic Net”. In: *Journal of the Royal Statistical Society, Series B* 67, pp. 301–320.